ABSTRACT

Large Eddy Simulation of Turbulent Flow Over Transverse Variations in Aerodynamic Roughness Length

David Willingham, M.S.M.E.

Committee Chairperson: William C. Anderson, Ph.D.

A great deal of literature has been published regarding the impact of complex roughness on turbulent flow. However, the topic of transverse variations in surface roughness, has received relatively little attention. In this thesis, large-eddy simulation is used to investigate the effects on turbulent, high Reynolds number flow, caused by periodic step-changes in aerodynamic roughness length, which persist in the streamwise direction. A parametric study is conducted with respect to the ratio of high to low roughness length and the transverse width of high roughness regions. Results show that lateral momentum flux across shear layers, generates secondary flows in the vicinity of transverse transitions in roughness. These secondary flows form boundary layer scale, counter-rotating vortices, which redistribute turbulence and momentum throughout the entire domain and create time-invariant regions of relatively low and high momentum, above low and high surface roughness, respectively.

Large Eddy Simulation of Turbulent Flow Over Transverse Variations in Aerodynamic Roughness Length

by

David Willingham, B.S.

A Thesis

Approved by the Department of Mechanical Engineering

____
William Jordan, Ph.D., Chairperson

Submitted to the Graduate Faculty of
Baylor University in Partial Fulfillment of the
Requirements for the Degree
of
Master of Science in Mechanical Engineering

Approved by the Thesis Committee

____
William C. Anderson, Ph.D., Chairperson

____
David A. Jack, Ph.D.

____
John M. Davis, Ph.D.

Accepted by the Graduate School
August 2014

____
J. Larry Lyon, Ph.D., Dean

Page bearing signatures is kept on file in the Graduate School.

TABLE OF CONTENTS

List of Figures v

List of Tables ix

Acknowledgments x

Dedication xi

Chapter 1 Introduction 1

1.1 Study Overview and Objectives 3

1.1.1 Application 4

Chapter 2 Simulatioin Details 7

2.1 Approaches to Turbulent Simulation 7

2.1.1 DNS 7

2.1.2 RANS 8

2.1.3 LES 8

2.2 Code Details 9

2.3 Domain Details 12

2.3.1 Boundary Conditions 13

2.3.2 Averaging 15

Chapter 3 Primary Simulation Results 17

3.1 Low and High Momentum Pathways 21

3.2 Coherent Structures 23

3.2.1 Vortex Cores 24

3.2.2 Induced Mean Flow Deviations 26

3.3 Stress Effects 32

3.3.1 Surface Stress 32

3.3.2 Transverse Surface Stress 35

3.3.3 Transverse Shear Stress 35
3.4 Variations of Local Boundary Layer Thickness 37
3.5 Turbulence Effects 38
3.6 Quadrant-Analysis 44
3.7 Turbulent Mixing Length 49

Chapter 4 Secondary Simulation Results 55
4.1 Enhanced Strip Width 58
4.2 Linearly Sloped Roughness 60
4.3 Sinusoidal Roughness 64
4.4 Discontinuous High Roughness Strips 68
4.5 Immersed Objects 73

Chapter 5 Conclusions and Recommendations 80
5.1 Conclusions 80
5.2 Futures Recommendations 83

Bibliography 86

LIST OF FIGURES

1.1 Illustration of flow past a perpendicularly aligned step-change in roughness . . . 2

1.2 Illustration of flow past a parallel aligned step-change in roughness . . 3

1.3 Illustration of the basic roughness configuration considered in this thesis 5

3.1 Vectors of Secondary flow components, superimposed over contours of streamwise velocity for cases A1-3. . . . 18

3.2 Vectors of secondary flow components, superimposed over contours of streamwise velocity for cases B1-3. . . . 18

3.3 Vectors of secondary flow components, superimposed over contours of streamwise velocity for cases C1-3. . . . 19

3.4 Vectors of secondary flow components, superimposed over contours of streamwise velocity for cases D1-3. . . . 19

3.5 Vectors of secondary flow components, superimposed over contours of streamwise velocity for cases E1-3. . . . 20

3.6 Vectors of secondary flow components, superimposed over contours of streamwise velocity for cases F1-3. . . . 20

3.7 Vectors of secondary flow components, superimposed over contours of swirling strength, λ_{ci}, from cases D1-3 . . . 26

3.8 Profiles of velocity components from cases A-F1 . . . 29

3.9 Profiles of velocity components from cases A-F2. . . . 29

3.10 Profiles of velocity components from cases A-F3 . . . 30

3.11 Profiles of transverse gradients, in streamwise velocity . . . 30

3.12 Absolute value of transverse distance between $Lx_2/(4\delta)$ and location of maximum transverse velocity gradient 32

3.13 Ratios of streamwise velocity obtained from LES and the log-law . . . 33

3.14 Mean profiles of streamwise and transverse surface lstress 34

3.15 Profiles of transverse shear stress, from cases 36

3.16 Local boundary layer thickness, superimposed over contours of streamwise velocity 37

3.17 Profiles of Reynolds normal stress components, from cases A-F1 . . . 41

3.18 Profiles of Reynolds normal stress components, from cases A-F2 . . . 42

3.19 Profiles of Reynolds normal stress components, from cases A-F3 . . . 42

3.20 Contours of turbulent kinetic energy 43

3.21 Contours showing differences in local and planar averaged turbulent fluctuations 43

3.22 Overview of alternate quadrant splitting scheme 45

3.23 Vertical probability profiles of quadrant events 46

3.24 Mean magnitude profiles of quadrant events, from cases A-F2 47

3.25 Ratios of the total contribution to Reynolds shear stress by Q_2 vs. Q_4 events 48

3.26 Transverse shear stress plotted vs. streamwise velocity gradient with least squared linear fits applied 51

3.27 Vertical profiles of turbulent eddy viscosity, $\nu_T/(\delta u_\tau)$ 52

3.28 Vertical profiles of transverse mixing length 53

3.29 Mixing length profile from case B3 with logarithmic fit applied to values below the shifting elevation of maximum transverse gradient. 53

4.1 Vectors of secondary flow components, superimposed over contours of streamwise velocity for cases d1-3 56

4.2 Streamwise averaged profiles of: wallstress, transverse velocity gradient and transverse shear stress at $x_3 \approx 0.01\delta$ for cases b2, B2, d2, D2, f2 and F2 57

4.3 Vectors of secondary flow components, superimposed over contours of streamwise velocity for cases D_w1, D_w2 and D_w3 60

4.4 Streamwise averaged profiles of: wallstress, transverse velocity gradient and transverse shear stress at $x_3 \approx 0.01\delta$ for cases $D_w1 - 3$ 61

4.5 Vectors of secondary flow components, superimposed over contours of streamwise velocity for cases B_w1, D_w1 and E_w11 62

4.6 Vectors of secondary flow components, superimposed over contours of streamwise velocity for cases B_L1, D_L1 and E_L1 64

4.7 Streamwise averaged profiles of: surface stress, transverse velocity gradient and transverse shear stress at $x_3 \approx 0.01\delta$ for cases $D_L1 - 3$ . . . 65

4.8 Vectors of secondary flow components, superimposed over contours of streamwise velocity for cases S1, S2 and S4 66

4.9 Streamwise averaged profiles of: surface stress, transverse velocity gradient and transverse shear stress at $x_3 \approx 0.01\delta$ for cases S2, S4 and S5 67

4.10 Illustration of basic surface roughness configuration used for cases in Table 4.4 69

4.11 Vectors of secondary flow components, superimposed over contours of streamwise velocity for cases G1-4 71

4.12 Vectors of secondary flow components, superimposed over contours of streamwise velocity for cases G5-8 72

4.13 Profiles of surface stress, transverse velocity gradient and transverse shear stress taken at $\{(x_2 = Lx_2/4 - L_s/2)/\delta, x_3/\delta \approx 0.01\}$ from cases G1, G4 and G7 73

4.14 Illustration of basic surface configuration used for cases in Table 4.6 . 75

4.15 Vectors of secondary flow components, superimposed over contours of streamwise velocity for cases $O1, O4$ and $O5$ 77

4.16 Streamwise averaged profiles of: transverse velocity gradient and transverse shear stress at $x_3 \approx 0.01\delta$ for cases $O2$,$O3$, $O4$ and $O5$ . . 77

4.17 Streamwise averaged profiles of: transverse velocity gradient and transverse shear stress at $x_3 \approx 0.01\delta$ for cases $O1$, $O4$ and $O6$ 78

4.18 Profiles of streamwise velocity, transverse velocity gradient and transverse shear stress taken at $\{(x_2 = Lx_2/4 - L_s/2)/\delta, x_3/\delta \approx 0.01\}$ from cases $O2$, $O3$, $O4$ and $O5$ 78

LIST OF TABLES

2.1 Physical Interpretations of Roughness Lengths for Homogeneous Surfaces 13

3.1 Summary of Primary Simulation Cases 17

4.1 Summary of Lower Resolution Cases 55

4.2 Summary of Cases with Widened Strip Width 59

4.3 Summary of Linearly Sloped Roughness Cases 63

4.4 Summary Sinusoidal Roughness Cases 66

4.5 Summary of Discontinuous Strip Cases 70

4.6 Summary of Immersed Object Cases 74

ACKNOWLEDGMENTS

I would like to express my deepest gratitude to my mentor Dr. William Anderson for the constant guidance, which he has provided me with throughout this entire process. Without the enormous amount of time and energy he has given me, over these last couple years, none of the work presented in this thesis would have been possible. I am grateful to Dr. Jack and Dr. Davis for taking time out of their busy schedules to review my thesis and be on my committee, and I am additionally grateful to Dr. Jack for providing me with the LaTeX template, used to make this thesis. Also, I would like to acknowledge Dr. Kenneth Christensen and Julio Barros for the valuable contributions they have made to this research.

Academic support for this research was provided by the Baylor University engineering department. Many thanks to all the faculty and staff in the Mechanical Engineering Department at Baylor, who have always been extremely pleasant and generous to me with their time and wisdom. Also, thanks to the Academic and Research Computing Services at Baylor, particularly Mike Hutcheson for his tireless efforts to keep Kodiak, and hence my research, running. I would also like to thank Scott Ulrich, who originally helped me to get familiar with the LES code. Lastly, I am sincerely grateful to my parents, sisters and grandparents, for all the unconditional love and support they have shown me over the years.

DEDICATION

To my father Glenn, whose work ethic and commitment to serving God and family, have always given me something to look up to.

CHAPTER ONE

Introduction

Heterogeneous surface roughness is a common feature throughout many natural and man-made surfaces. Roughness heterogeneities may take the form of anything from patches of corrosion on metal plating, to entire cities or forests. Making an assumption of uniform surface roughness is convenient for the sake mathematical simplicity, when analyzing many turbulent flow scenarios. However, care must be taken because realistically, few examples of truly homogeneous surface roughness exist. For this reason, a more complete understanding of the way in which complex surface roughness interacts with turbulent, flow, is a topic of serious interest to both the scientific and engineering communities.

There has been a great deal of both numerical and experimental research that has sought to identify flow effects, caused by rapid changes in surface roughness length. The case in which flow encounters a forward step-change from a surface with relatively low roughness length, $z_{0,L}$, to an adjacent surface with relatively high roughness length, $z_{0,H}$, (as is illustrated in Figure 1.1) has been given particular attention [1–5]. The considerable amount of attention paid to this specific roughness configuration is logical simply from an intuitive standpoint, as one might expect streamwise step-changes in roughness to produce the most dramatic effects on incoming flow. It has been shown that forward step-changes in roughness give rise to the formation of an internal boundary layer (IBL), δ_i. Beyond the roughness step-change, the IBL has been shown to grow in the streamwise, x_1, direction according to the Wood model [4]:

$$\delta_i(x_1, z_{0,H}) = C z_{0,H} \left(\frac{x_1}{z_{0,H}} \right)^n, \tag{1.1}$$

where it has been experimentally determined that C=0.28 and $n \approx 0.28$ [6]. Such a sudden rise in surface roughness also results in increased turbulence and stress directly downstream of the transition [2, 6–9]

Aerodynamic (or momentum) roughness length, z_0, represents the theoretical elevation at which logarithmic velocity profiles reach zero, when extrapolated below the height where the law-of-the-wall can be accurately applied. Roughness lengths are often defined with respect to other scalar quantities such as heat or humidity and these alternately defined roughness lengths differ in value form aerodynamic roughness length [10, 11]. Such scalar roughness lengths correspond with the wall-normal distance at which the scalar quantity theoretically reaches it's surface value, rather than zero. However, please note that all references to roughness and roughness length hereafter will exclusively refer to surface roughness associated with momentum.

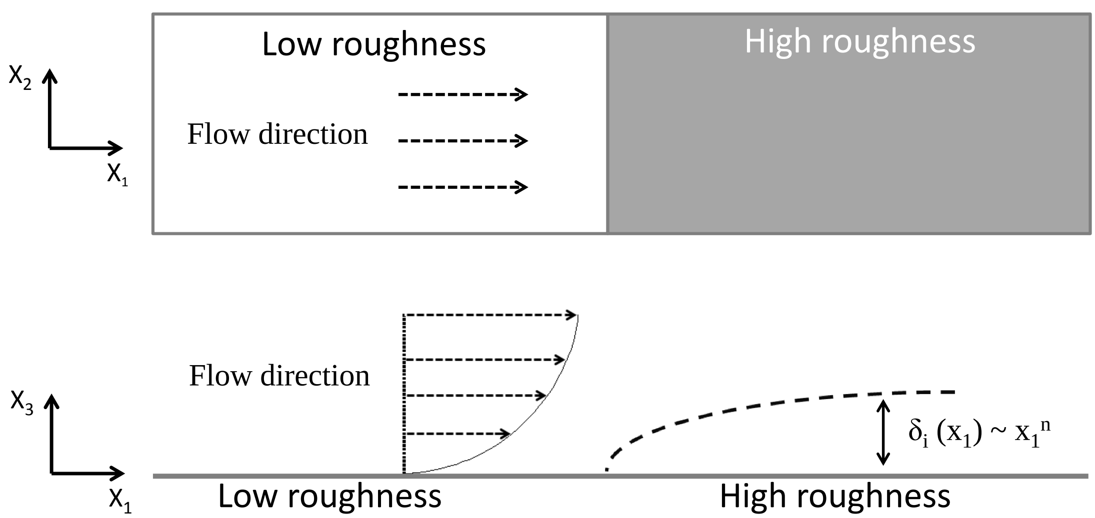

Figure 1.1: Illustration of flow past a perpendicularly aligned step-change in roughness. Top image shows overhead view, bottom image shows side view with internal boundary layer.

The Figure 1.1, IBL scenario is an adequate approximation of many realistic surfaces and certainly merits the attention it has received. However, it assumes a prevailing flow direction which is aligned at precisely a perpendicular angle with respect to the transition in surface roughness. Of course, in reality, many applications must deal with streamwise flow that may approach from all possible directions. Yet relatively little literature currently exists concerning flow with non-normal orientation to roughness step-changes and to the authors knowledge no such studies have been preformed numerically. Due to the lack of previous research on this topic, the specific scenario considered in this thesis, is streamwise flow, aligned parallel to step-changes in roughness, as illustrated in Figure 1.2.

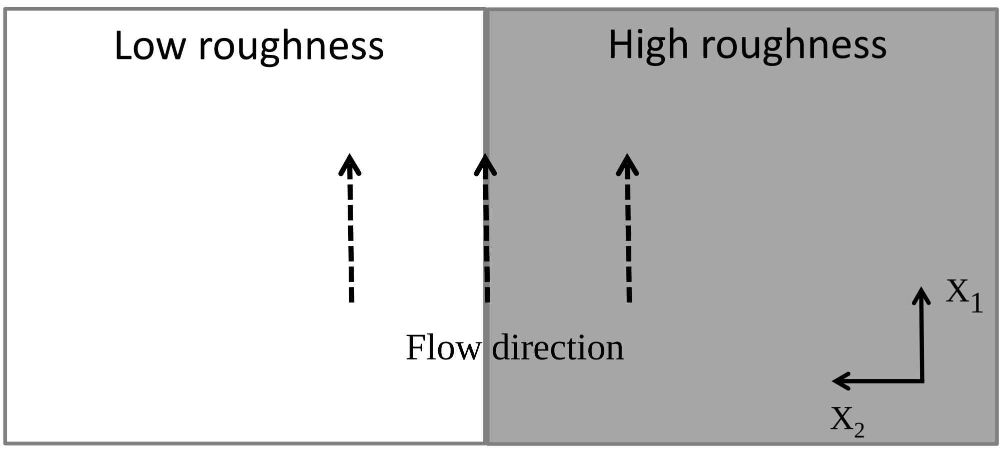

Figure 1.2: Illustration of flow past a parallel aligned step-change in roughness.

1.1 Study Overview and Objectives

In order to address the current lack of numerical studies regarding the general effects of transverse variations in surface roughness, one primary and several secondary suites of large eddy simulations (LES) have been run, which consist of fully turbulent, high Reynolds number flow. The code used here was developed at Johns

Hopkins University and relevant details pertaining to the code are provided in Chapter 2. Figure 1.3 provides a sketch of the roughness configuration used in the primary LES set. These primary LES consist of two, equally spaced, elevated roughness strips which are aligned parallel to the streamwise flow direction. Detailed results and analysis of these primary simulations are located in Chapter 3, while results and discussion of secondary cases may be found in Chapter 4. Secondary simulations are intended to provide further analysis of transverse roughness transitions, by exploring the effects caused by specific modifications to the lower LES boundary conditions, as sketched in Figure 1.3. The information gained from secondary simulations is intended to support and further build upon the conclusions derived from primary simulation results. The advantage of a numerical study such as this one, is the ability to consider a highly controlled environment with easily adjustable parameters. The primary parameters of interest here are: the ratio of high to low surface roughness lengths $\lambda = z_{0H}/z_{0L}$, and the width of the high roughness strips, L_s/δ, where δ represents the vertical extent of all simulation domains.

In short, the primary objectives of this study are to:

1. Provide a parametric study of the effects, caused by transverse variations in surface roughness, on turbulent, high Reynolds number flow.

2. Accurately predict statistical effects and coherent structures produced by transverse roughness variations and offer some insight into the underlying mechanisms responsible for them.

1.1.1 Application

As a result of periodic boundary conditions, surfaces shown in Figure 1.3 are equivalent to an infinite number of infinitely long high roughness strips. Therefore,

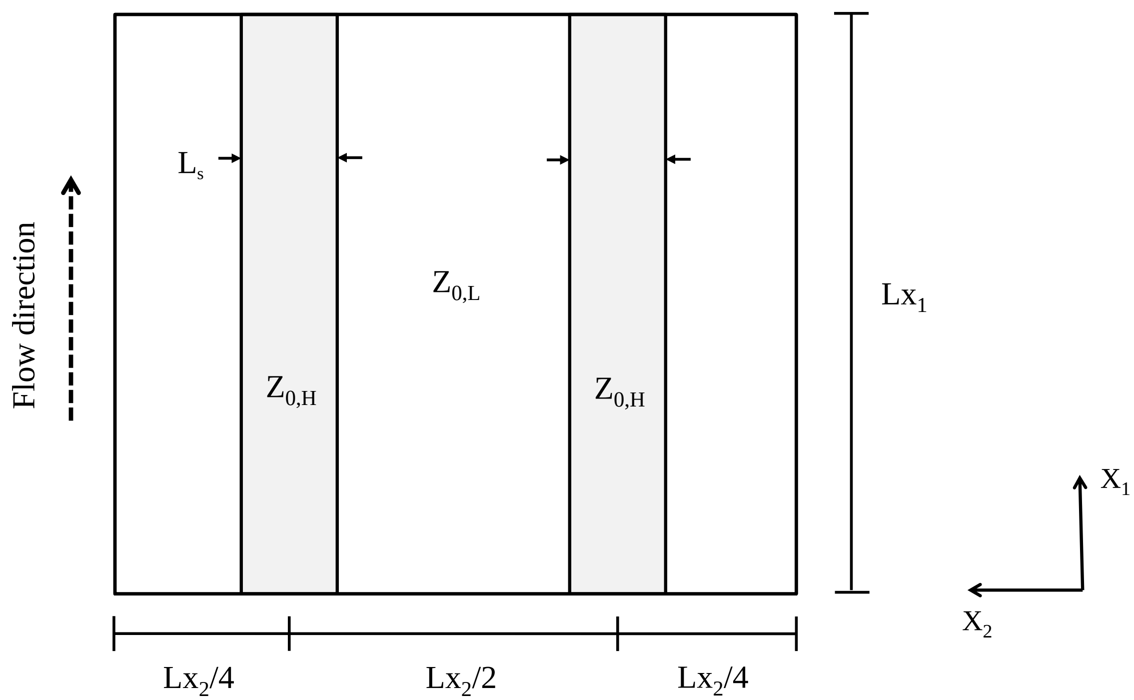

Figure 1.3: Illustration of the basic roughness configuration considered in this thesis.

it must be made clear that this roughness configuration is an idealization and is not intended to correspond precisely with any actual surfaces. Instead the goal here is to investigate the theoretical limits of flow over transverse roughness transitions that extend over large distances, with the understanding that shorter strips will likely produce milder effects. However, there are a wide range of potential applications which may be approximated by the scenario presented in Figure 1.3.

Many land-surfaces exposed to atmospheric flow, exhibit abrupt roughness changes due to variations in vegetation density, bodies of water (such as lakes and rivers) bordered by forests, urban environments and roadways. In fact all natural surfaces which may be approximated by Figure 1.1 may also, at times, be approximated by Figure 1.2, depending on the currently prevailing wind direction.

The vast majority of turbulent momentum, heat and mass transport from land-surfaces are determined by the dynamics of flow located in the lower section of the atmospheric boundary layer (ABL), because this is where the greatest amount of turbulent mixing occurs [12]. Thus this topic is of particular interest to all classes of atmospheric sciences, such as hydrology, meteorology and climatology. Figure 1.3 could also be representative of a wide range of mechanical and aerospace engineering applications such as naval architecture, wind farms (such as those considered by Baidya-Roy [13]) or turbine blade roughness. Although the results presented below deal only with momentum transfer, it is believed that they may have significant implications for both heat and mass transfer, due to enhancement of turbulent mixing and large-scale vortices at the surface.

CHAPTER TWO

Simulatioin Details

2.1 Approaches to Turbulent Simulation

Numerical simulations of turbulent flow, such as those in this thesis, are typically carried out using one of three approaches.

1. Direct Numerical Simulation (DNS).

2. Reynolds Averaging of the Navier Stokes equations (RANS).

3. Large Eddy Simulation (LES).

2.1.1 DNS

During DNS, momentum transport equations are directly integrated, both temporally and spatially, over all scales of turbulence. This makes DNS the most accurate method available, but also the most computationally expensive. As new technology allows computational power to progress, DNS is becoming an increasingly viable option for many applications and gaining more wide spread use. However, DNS is currently not reasonable for the present study which considers high Reynolds number atmospheric flow with Re $\backsim 10^8$ (where $\backsim$ denotes order of magnitude). It has been shown that the number of degrees of freedom required to apply DNS to a three-dimensional flow can be related to Reynolds number through: (number of degrees of freedom) $\approx Re^{9/4}$ [14]. Because the present work deals with high Reynolds numbers on the order of 10^8, $\backsim 10^{18}$ degrees of freedom would need to be accounted for in order to apply DNS. Unfortunately, this is far beyond what is currently feasible for this work.

2.1.2 RANS

The RANS method of simulating turbulence, relies on temporal averaging of flow properties (velocity, pressure, etc.) to eliminate instantaneous fluctuations caused by turbulence. Instead of resolving all scales of turbulence like DNS, RANS does not resolve turbulence at all. Instead, the effects of turbulence are entirely accounted for by a closure model, which relies upon pre-existing knowledge of flow conditions for calibration. Therefore, RANS is not well-suited to the current study, because the ability to capture instantaneous data is desired and because a lack of pre-existing data is, in fact, one of the primary reasons that this problem is of interest in the first place.

2.1.3 LES

Large eddy simulation was introduced by Joseph Smagorinsky in 1963 [15]. The fundamental idea behind LES is to resolve only large scales of turbulent eddies in the flow and use a model to account for small scales. This is acceptable because in turbulent flow, most energy associated with momentum is contained in the largest scales of turbulence, while the great majority of energy dissipation occurs at the smallest scales. LES first applies a filter to separate large and small scales of turbulence based on a specified grid size, Δ. Then scales larger than Δ are resolved (i.e. solved through integration of the momentum equations), while scales smaller than Δ are modeled through a subgrid-scale (SGS) closure model. The filtering process can be described by

$$\tilde{\mathbf{u}}(\mathbf{x}) = \int \mathbf{u}(\mathbf{x}')F_{\Delta}(\mathbf{x} - \mathbf{x}')d\mathbf{x}'. \tag{2.1}$$

Where F_{Δ} is a filter function for scale Δ. $\mathbf{u}(x)$ is the velocity vector, $\{\mathbf{u}(x) = u_1, u_2, u_3\}$, for flow at a location determined by spatial coordinates $\{\mathbf{x} = x_1, x_2, x_3\}$.

$\tilde{\mathbf{u}}(x)$ is the "resolved" velocity vector $\{\tilde{\mathbf{u}}(x) = \tilde{u}_1, \tilde{u}_2, \tilde{u}_3\}$, which is locally evaluated at $\{\mathbf{x}\}$. Instantaneous velocity values can then be expressed as

$$u_i = \tilde{u}_i + u_i^{SGS},\ i = 1, 2, 3 \tag{2.2}$$

Where u_i represents total velocity, $\tilde{u}_i$ represents the resolved component of velocity and u_i^{SGS} is the unresolved component of velocity which requires modeling. For this study LES is clearly the best suited approach as it requires significantly less computational expense than DNS and offers more accuracy and flexibility than the RANS approach.

2.2 Code Details

The code used for all simulations presented in this thesis is the Johns Hopkins University, Large Eddy Simulation (JHU-LES) code. This code has been used numerous times in previous literature [e.g., Albertson and Parlange 1999a [10], Bou-Zeid *et al* 2005 [16], Anderson 2012 [17] and Port*é*-Agel et al. 2000 [18]]. For a more detailed description of this code see Albertson 1999b [19]. This code was developed specifically for simulation of flow in the atmospheric boundary layer over large land surfaces. However, all results here are output in non-dimensional form to facilitate application at any desired scale.

The governing equations used for these simulations are the incompressible continuity equation and the three dimensional momentum transport equations. Note that terms due to Coriolis accelerations have been omitted and effects of viscosity are considered negligible due to high Reynolds number. Using the definition of velocity given in Equation 2.2 these equation are written as:

$$\frac{\partial \tilde{u}_i}{\partial x_i} = 0, \tag{2.3}$$

$$\frac{\partial \tilde{u}_i}{\partial t} + \tilde{u}_j \left(\frac{\partial \tilde{u}_i}{\partial x_j} - \frac{\partial \tilde{u}_j}{\partial x_i} \right) = -\frac{1}{\rho} \frac{\partial \tilde{p}^*}{\partial x_i} - \frac{\partial_j \tau_{ij}}{\partial x_j} - \delta_{i1} \frac{1}{\rho} \frac{\partial P}{\partial x_1}. \tag{2.4}$$

Here δ_{ij} is the Kronecker delta where ($\delta_{ij} = 1$ for $i = j$ and $\delta = 0$ for $i \neq j$), $\partial P/\partial x_1$ is a streamwise pressure gradient and ρ is fluid density. The SGS stress tensor, defined by

$$\tau ij = \widetilde{u_i u_j} - \tilde{u}_i \tilde{u}_j, \tag{2.5}$$

is decomposed into its trace, τ_{kk}, and deviatoric component, τ_{ij}^d such that

$$\tau_{ij}^d = \tau_{ij} - \frac{1}{3}\tau_{kk}\delta ij. \tag{2.6}$$

$\tilde{p}^*$ is a modified pressure term and can be written as

$$\tilde{p}^* = \tilde{p} + \frac{1}{3}\rho\tau_{kk} + \frac{1}{2}\rho\tilde{u}_j\tilde{u}_j \tag{2.7}$$

where $(\tilde{p}/\rho)$ is the Boussinesq kinematic pressure and $(\frac{1}{3}\tau_{kk})$ is the removed trace of τ_{ij} taken from the second term on the right of Equation 2.4. $\frac{1}{2}\tilde{u}_j\tilde{u}_j$ is included so that Equation 2.4 may be written in rotational form, which is needed for conservation of kinetic energy and mass [20]. With Equation 2.3 and the divergence of Equation 2.4, a pressure Poisson equation is obtained and solved dynamically for $\tilde{p}^*$. As a note on notation, the superscript $\tilde{}$ is used here to represent filtering at the grid scale while $\widehat{\tilde{}}$ represents filtering at twice the grid scale, 2Δ.

In order to obtain a closed form solution for the deviatoric part of the SGS stress, τ_{ij}^d, the classic Smagorinsky model is applied [15]

$$\tau_{ij}^{smag} = -2\nu_T\tilde{S}_{ij} \tag{2.8}$$

where the value $\tilde{S}_{ij}$ represents the resolved strain rate tensor which can be expressed as

$$\tilde{S}_{ij} = 0.5\left(\frac{\partial\tilde{u}_i}{\partial x_j} + \frac{\partial\tilde{u}_j}{\partial x_i}\right) \tag{2.9}$$

ν_T is the turbulent eddy-viscosity and is given by

$$\nu_T = (C_s\Delta)^2|\tilde{S}| \tag{2.10}$$

where $|\tilde{S}| = \sqrt{2\tilde{S}_{ij}\tilde{S}_{ij}}$ is the magnitude of the strain rate tensor. The Smagorinsky coefficient, C_s, is simply assigned a constant value of 0.16 for the present study, based on the work of Lilly [21]. A number of modified Smagorinsky models which use more sophisticated selection methods for C_s values have been developed. For example, the dynamic Smagorinsky model introduced by Germano *et al.* [22], which allows values of C_s to be dynamically updated during simulation. Bou-Zeid *et al.* 2005 [23] presented a scale-dependent, Lagrangian dynamic model, which adds on to the work of Germano *et al.* by accounting for the effects of scale-dependence and employing Lagrangian averaging to allow consideration of more complex geometries with heterogeneous flow field directions [23]. However, it is undesirable to use either planar or Lagrangian averaging for the current simulations, due to abrupt spanwise variations in surface roughness, which cause increased error for any spatial averaging performed in non-streamwise directions. Therefore, it is believed that using a constant Smagorinsky coefficient value is the only viable option for the surfaces under consideration in this thesis.

Forcing is applied using an imposed streamwise pressure gradient of $\partial P/\partial x_1 = u_\tau^2/\delta$, where u_τ is shear velocity and δ is the domain height. Derivatives in the horizontal directions are solved using pseudo-spectral methods (see Orzarg 1971 [24, 25]) and vertical derivatives are solved using a centered second order finite-differencing scheme (see Monin *et al.* 1978 [26]). In order to step through time, a fully explicit second-order Adams-Bashforth scheme is used which can be written as:

$$\frac{\tilde{u}_i^{t+\Delta t} - \tilde{u}_i^t}{\Delta t} = \frac{3}{2}RHS_i^t - \frac{1}{2}RHS_i^{t-\Delta t}, \tag{2.11}$$

Where RHS represents the right hand side of Equation 2.4, solved for $\partial\tilde{u}_i/\partial t$ in discrete form. Convection terms of Equation 2.4 are de-aliased using the 3/2 padding rule which is necessary to avoid contamination of the smallest resolved scales of flow, due to the use of fast Fourier transforms.

2.3 Domain Details

Throughout all following chapters the notation i=1,2,3 corresponds with streamwise, transverse and vertical directions, respectively. Accordingly x_1, x_2 and x_3 represent streamwise, transverse and vertical coordinates, respectively, and Lx_1, Lx_2 and Lx_3 are used to denote streamwise, transverse and vertical domain extents, respectively. Likewise grid-spacing and node number are described by $\{\Delta_1, \Delta_2,\ \Delta_3\}$, and $\{Nx_1, Nx_2,\ Nx_3\}$, respectively. A staggered grid was employed for $\tilde{u}_1$ and $\tilde{u}_2$ data points, so that their lowest values are calculated at $\Delta_3/2$, while the lowest non-zero values of $\tilde{u}_3$ are placed at Δ_3. All lengths associated with the domain shown in figure 1.3 are non-dimensionalized by the domain height δ which physically represents 1000 meters. This significant height is desired in order to capture the entire internal boundary layer. All velocity values are non-dimensionalized by a single friction velocity $u_\tau = 0.45\, m/s$.

The horizontal domain lengths, Lx_1 and Lx_2 were assigned equal values of $2\pi/\delta$. Values of high roughness length, z_{0H}, are given a value of $1.0/\delta$ and held constant throughout all cases regardless of λ or Ls/δ, so that changing the value of λ is equivalent to changing values of low roughness length, z_{0L}. This particular $z_{0,H}$ value was chosen in order to create substantial, but not physically unrealistic effects on the flow. In earlier stages of this research, comparison was made between cases, with different values of $z_{0,H}$. These cases were vastly different than those considered in this thesis and thus, are not presented here. But it was observed that changing values of $z_{0,H}$ has relatively little effect compared to changing values of λ and L_s/δ. Roughness length ratios over three orders of magnitude were considered ranging from 2 to

900. Table 2.1 lists physical interpretations of surface roughness lengths, although as discussed previously, the results presented here may be applied to a wide range of length scales due to their non-dimensional form. Three strip widths of $\approx 0.2\delta$, $\approx 0.6\delta$ and $\approx 1.0\delta$ were used for the primary cases. The exact location of the high roughness strips can be described as: $z_0 = z_{0,H}$, if $(1/4Lx_2 - 1/2Ls) \leq x_2 \leq (1/4Lx_2 + 1/2Ls)$ or $(3/4Lx_2 - 1/2Ls) \leq x_2 \leq (3/4Lx_2 + 1/2Ls)$ and $z_0 = z_{0,L}$ at all other locations.

Table 2.1: Physical Interpretations of Roughness Lengths for Homogeneous Surfaces (Taken From Wieringa 1993 [27])

Surface type	z_0 (cm)
Sea, loose sand	0.02
Concrete, flat desert, tidal flat	0.02-0.05
Flat snow field	0.01-0.07
Rough ice field	0.1-1.2
Fallow ground	1-0.4
Short grass and moss	0.8-3.0
	z_0 (m)
Long grass, and heather	0.02-0.06
Low mature agricultural crops	0.04-0.09
High mature agricultural crops (grain)	0.12-0.18
Continuous bush land	0.35-0.45
Mature pine forest	0.8-1.6
Tropical forest	1.7-2.3
Dense low buildings (suburb)	0.4-0.7
Regular-built large town	0.7-1.5

2.3.1 Boundary Conditions

Boundary conditions in the horizontal directions are periodic for both velocity and pressure, which is necessitated by the use of pseudo-spectral methods. At the domain's top boundary, zero stress and normal velocity are applied so that $\tilde{u}_3|_{x_3=\delta} = \partial\tilde{u}_3/\partial x_3|_{x_3=\delta} = 0$. Pressure at the top and bottom boundaries are assigned as $\partial\tilde{p}^*/\partial x_3|_{x_3=0} = 0$ and $\tilde{p}^*/\partial x_3|_{x_3=\delta} = 0$. At the surface, zero normal velocity is imposed, and aerodynamic drag is applied to the flow using the equilibrium logarithmic law [28]. Assuming a neutrally stratified turbulent boundary layer with zero buoyant forces, the components of drag acting on the streamwise and transverse components of velocity at the wall, τ_{13}^w and τ_{12}^w, are given as:

$$\frac{\tau_{13}^w}{\rho} = -\left[\frac{\kappa U}{\ln(x_3/z_0(x_1,x_2))}\right]^2 \frac{\hat{\tilde{u}}_1}{U}, \tag{2.12}$$

$$\frac{\tau_{23}^w}{\rho} = -\left[\frac{\kappa U}{\ln(x_3/z_0(x_1,x_2))}\right]^2 \frac{\hat{\tilde{u}}_2}{U}, \tag{2.13}$$

Where κ is the Von K$\acute{a}$rm$\acute{a}$n constant, U is the magnitude of the horizontal velocity components, $U = (\hat{\tilde{u}}_1^2 + \hat{\tilde{u}}_2^2))^{1/2}$, and $z_0(x_1, x_2)$ is the local surface roughness length. The superscript ^{w} indicates that statistics are taken at the lowest computational level. Filtering of velocity at twice the grid scale is used in Equations 2.3-2.4 because it has been shown to help reduce undesirable fluctuations [2]. In order to ensure that the flow is fully turbulent, random, low amplitude values are added to the initial velocity field. Because of this, simulations returns unique result each time they are run and some amount of asymmetry is introduced into the flow statistics.

It should be kept in mind that the effects caused by each high roughness strip are not decoupled from the effects of the two neighboring strips on either side. This is the result of induced secondary flows, which are discussed further in Chapters 3 and 4. It was originally desired to consider only a single transverse roughness transition per domain. But isolating the effects of an individual roughness transition, while maintaining acceptable mesh resolution, was found to be impractical and this ultimately led to the adoption of the current scenario shown by Figure 1.3. While this change may result in somewhat less general results, it is believed to be more realistic for many practical applications, since very large regions of completely homogeneous roughness are uncommon in most engineering applications and natural land-surfaces. The domain size and specific configuration depicted in Figure 1.3, has been selected (primarily through trial and error) as a means of clearly illustrating the effects of these periodic, parallel aligned surface roughness transitions. The use of two strips here is admittedly redundant due to the periodic boundary conditions, but the addition of a second strip was found to be useful for visualization of various flow characteristics.

2.3.2 Averaging

The notation used here to denote averaging is $\langle ... \rangle_{x,y,z}$ where x, y and z are arbitrary constants which define the sequence of averaging operations used, in order from inner to outer subscripts. All flow statistics presented in this thesis, were acquired at steady state conditions. During simulation velocity and stress values were averaged in time for a sufficient duration to ensure temporal statistical homogeneity. The code then continues to run beyond this point until enough data has been collected for accurate temporal averaging. As a result of periodic boundary conditions and uniform surface roughness in the x_1 dimension, spatial averaging may be done along the streamwise direction. However, no other form of spatial averaging is valid for these simulations, due to the transverse heterogeneities in surface roughness. Because of the staggered grid used by the code, local values of $\tilde{u}_3$ are defined as averages between x_3 nodes to ensure that all velocity statistics are taken at identical locations. Also, gradients of streamwise velocity in the transverse direction are computed using central differencing to allow for comparison with other statistics, located at computational nodes.

As a final but important note on averaging, Equation 2.14 defines total values of Reynolds stress (i.e. the sum of SGS and resolved Reynolds stress components) as

$$\langle T_{ij} \rangle_t = \langle \tau_{ij} \rangle_t + \langle \tilde{u}_i' \tilde{u}_j' \rangle_t, \tag{2.14}$$

where $\langle \tau_{ij} \rangle_t$ is the SGS component of Reynolds stress and $\langle \tilde{u}_i' \tilde{u}_i' \rangle_t$ is the resolved component. In Equation 2.14 the prime notation refers to local deviation from the streamwise mean so that $\tilde{u}_i' = \tilde{u}_i - \langle \tilde{u}_i \rangle_1$.

CHAPTER THREE

Primary Simulation Results

The primary suite of LES, with a total of eighteen simulations is presented and discussed in this Chapter. Table 3.1 gives a complete summary of these cases and the relevant parameters associated with them. Figures 3.1-3.6 present contours of streamwise velocity averaged in time and the streamwise direction. Vectors constructed from the secondary velocity components $\langle \tilde{u}_2 \rangle_{t,1}/u_\tau$ and $\langle \tilde{u}_3 \rangle_{t,1}/u_\tau$ have been superimposed to indicate mean secondary flow directions and white, dashed lines are used to to provide reference for the x_2 locations of the roughness transitions at the surface. Note that this convention of dashed lines over locations of spanwise roughness transition, is continued throughout the results presented in this Chapter as well as Chapter 4. These images provide a good sense of the general flow characteristics caused by the periodic step-changes in surface roughness, shown in Figure 1.3. In order to demonstrate the amount of variability in LES results for the given parameters listed in Table 3.1, every simulation in Table 3.1 has been included in Figures 3.1-3.6.

Table 3.1: Summary of Primary Simulation Cases

Case	λ	$\approx Ls/\delta$
A1, A2, A3	2	0.2, 0.6, 1.0
B1, B2, B3	10	0.2, 0.6, 1.0
C1, C2, C3	25	0.2, 0.6, 1.0
D1, D2, D3	100	0.2, 0.6, 1.0
E1, E2, E3	500	0.2, 0.6, 1.0
F1, F2, F3	900	0.2, 0.6, 1.0

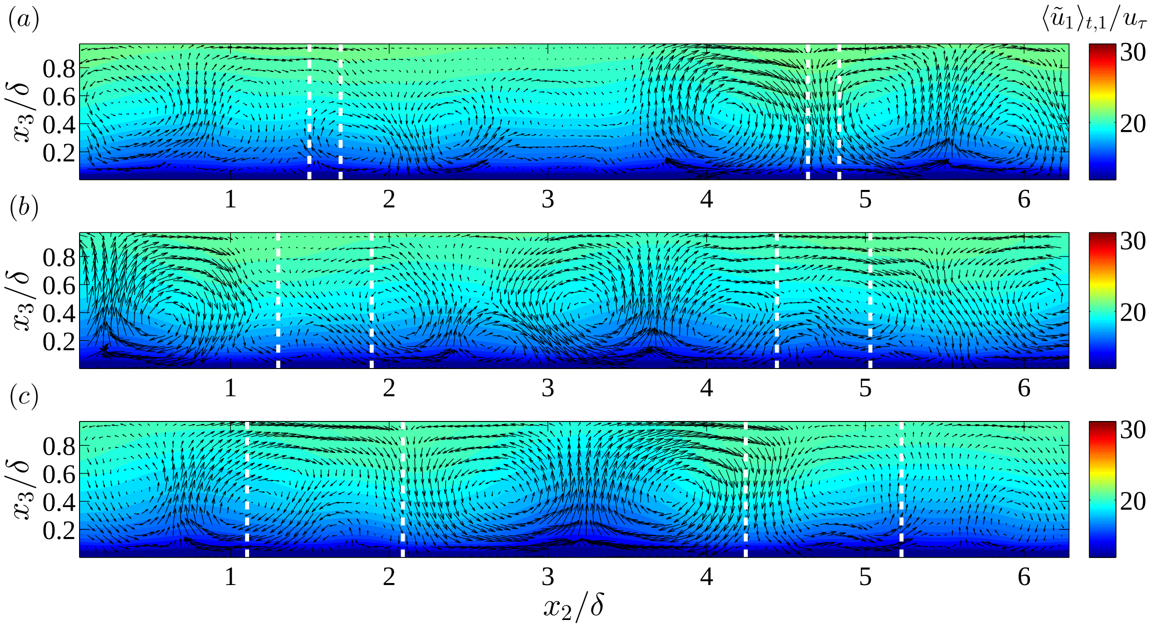

Figure 3.1: Black vectors of secondary flow components, $\{\langle \tilde{u}_2 \rangle_{t,1}/u_\tau, \langle \tilde{u}_3 \rangle_{t,1}/u_\tau\}$, superimposed over contours of streamwise velocity for cases A1-3. White dotted lines indicate x_2/δ locations of transverse variations in surface roughness.

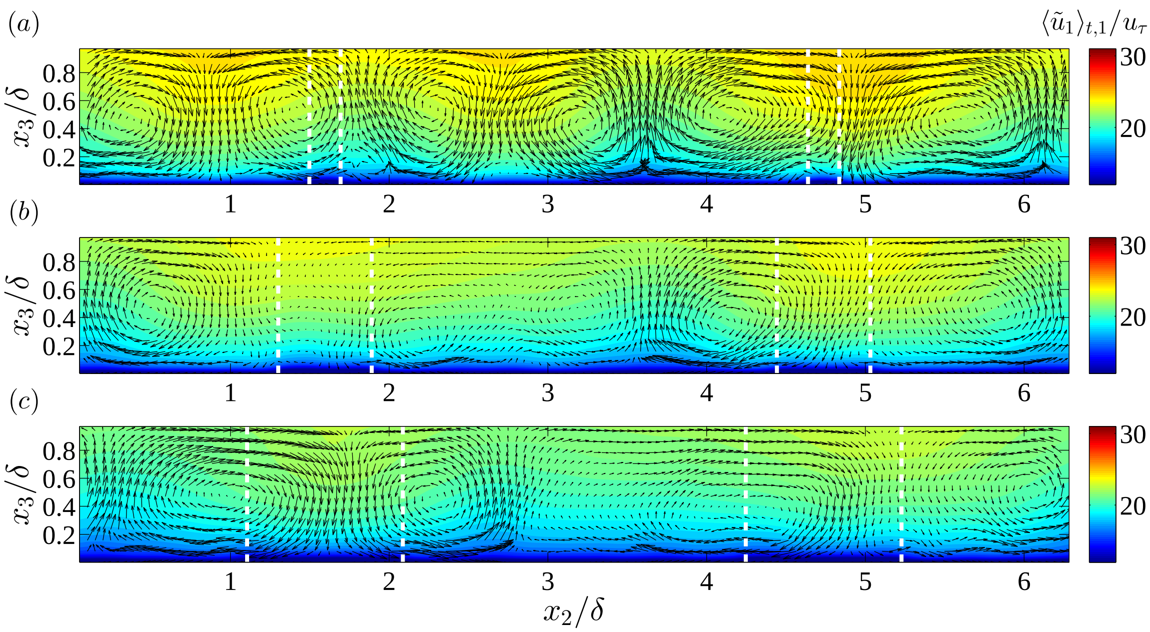

Figure 3.2: Black vectors of secondary flow components, $\{\langle \tilde{u}_2 \rangle_{t,1}/u_\tau, \langle \tilde{u}_3 \rangle_{t,1}/u_\tau\}$, superimposed over contours of streamwise velocity for cases B1-3.

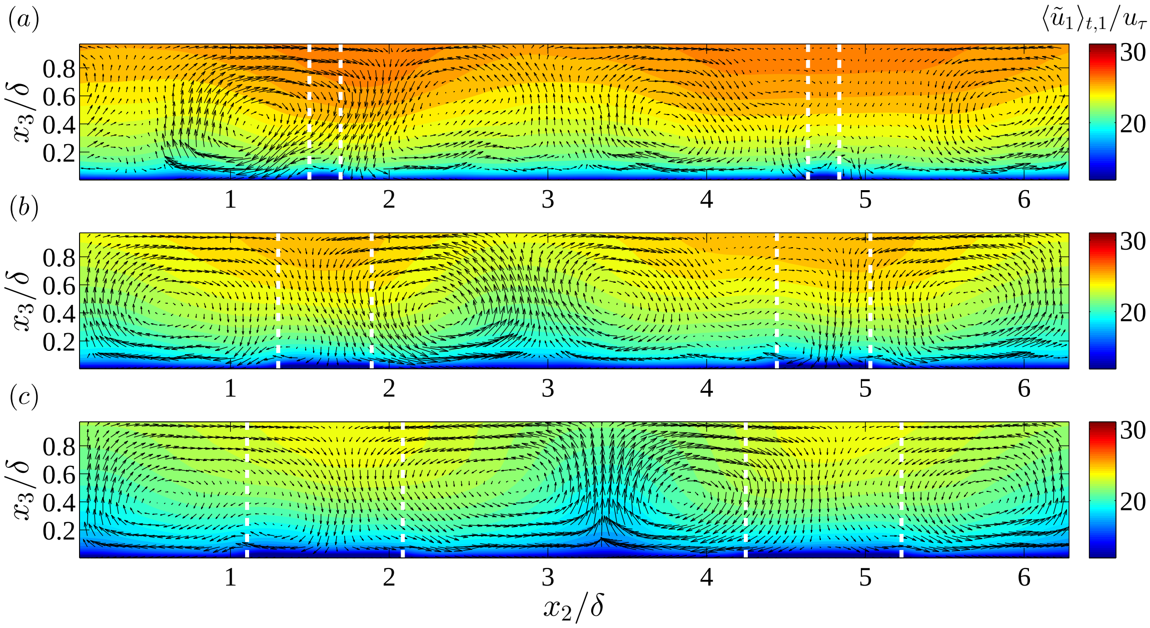

Figure 3.3: Black vectors of secondary flow components, $\{\langle \tilde{u}_2 \rangle_{t,1}/u_\tau, \langle \tilde{u}_3 \rangle_{t,1}/u_\tau\}$, superimposed over contours of streamwise velocity for cases C1-3.

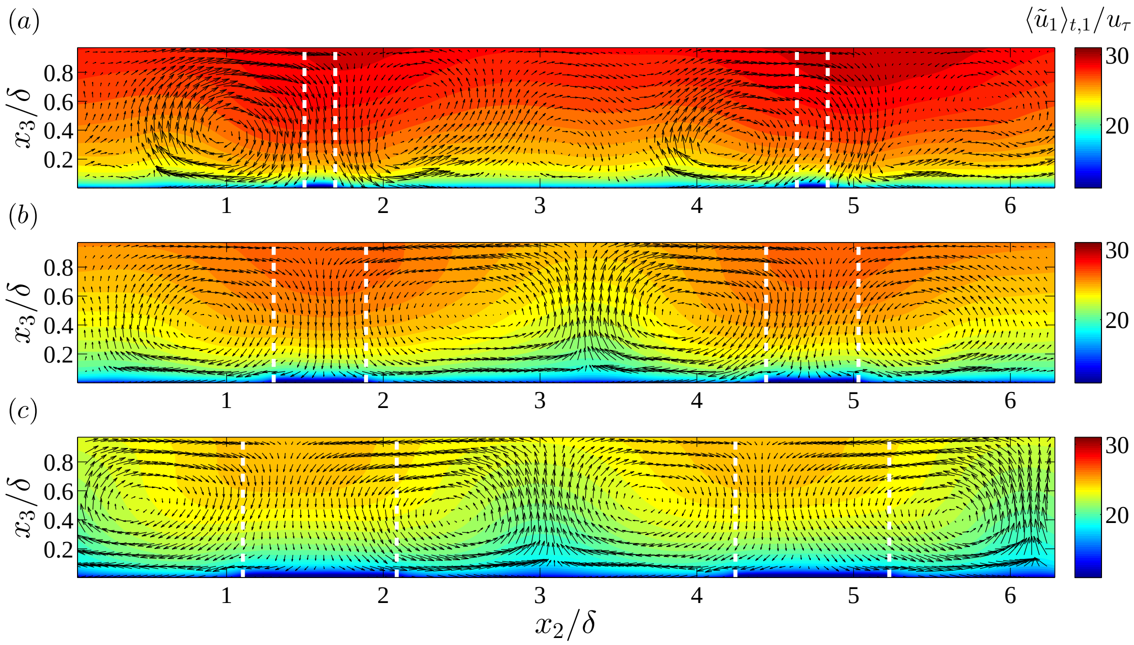

Figure 3.4: Black vectors of secondary flow components, $\{\langle \tilde{u}_2 \rangle_{t,1}/u_\tau, \langle \tilde{u}_3 \rangle_{t,1}/u_\tau\}$, superimposed over contours of streamwise velocity for cases D1-3.

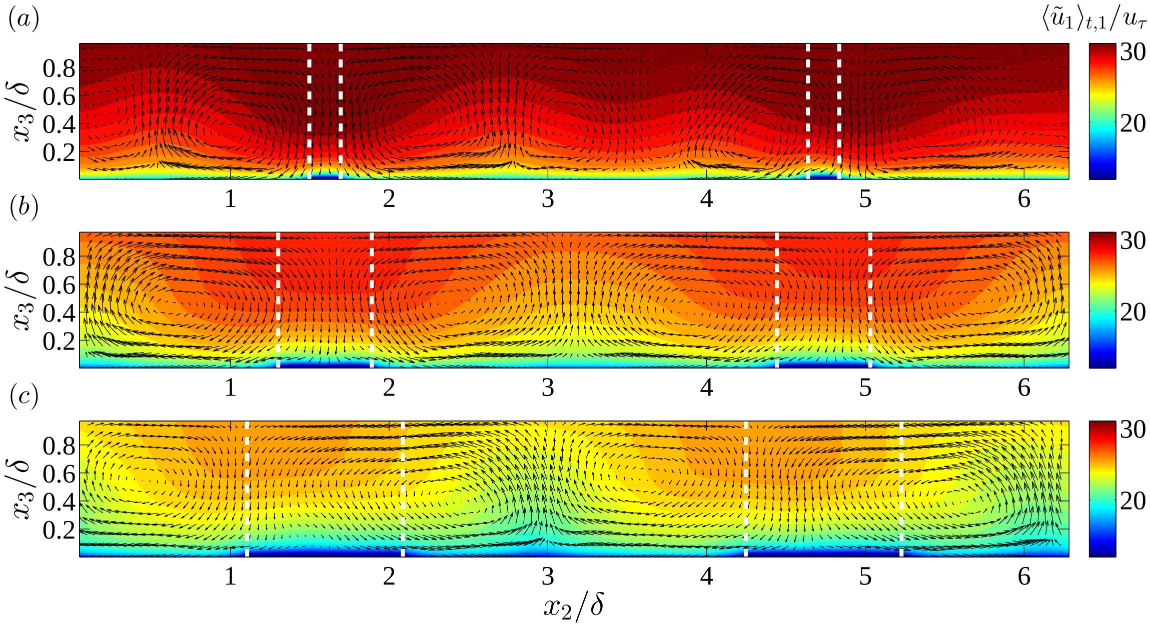

Figure 3.5: Black vectors of secondary flow components, $\{\langle\tilde{u}_2\rangle_{t,1}/u_\tau, \langle\tilde{u}_3\rangle_{t,1}/u_\tau\}$, superimposed over contours of streamwise velocity for cases E1-3.

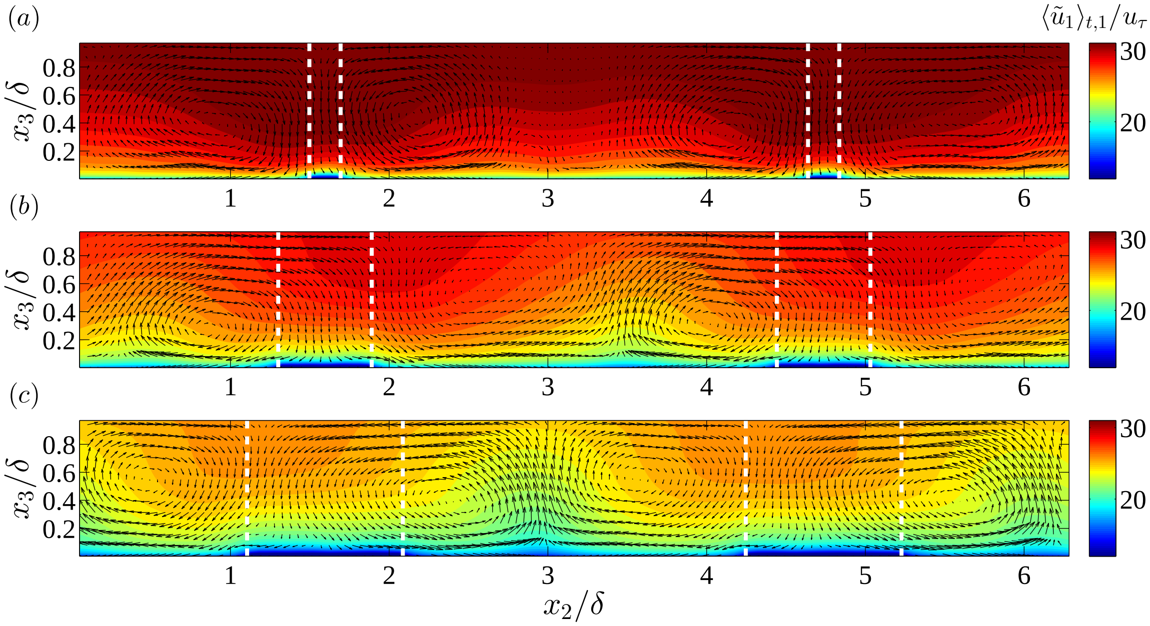

Figure 3.6: Black vectors of secondary flow components, $\{\langle\tilde{u}_2\rangle_{t,1}/u_\tau, \langle\tilde{u}_3\rangle_{t,1}/u_\tau\}$, superimposed over contours of streamwise velocity for cases F1-3.

Figures 3.1-3.6 illustrate two particularly striking characteristics of the LES flowfields:

1. The periodic formation of high and low momentum pathways, which consistently form above the high roughness length, z_{0H}, and low roughness length, z_{0L}, surface regions, respectively.

2. Counter rotating, boundary layer scale vortices, which develop on both sides of the high roughness strips.

These two characteristics can often be seen, even for roughness strips with low values of λ such as those shown in Figure 3.1-3.2. The terminology high momentum pathway (HMP) and low momentum pathway (LMP), was introduced by Mejia-Alvarez *et al.*, [29] to describe experimental results observed in flow over heterogeneous turbine blade roughness and is quite appropriate for results shown in Figures 3.1-3.6.

These two prominent flow features will be discussed individually in greater detail, but it should be initially pointed out that there is a strong correlation between them. Close inspection of Figures 3.1-3.6 show that without exception, boundary layer scale vortices rotate into low momentum pathways and away from high momentum pathways along the surface. Identification of the underlying mechanisms responsible for these two flow characteristics has been and continues to be one of the primary points of emphasis for this research.

3.1 Low and High Momentum Pathways

The formation of instantaneous, low velocity streaks in turbulent flow, has been observed frequently in previous literature [30–33]. What makes the results shown in Figures 3.1-3.6 unique from the bulk of previous studies, is that the observed high and low velocity streaks do not meander or change with time. Instead, the development of “pathways” is observed, and these pathways are approximately stationary with respect to both space and time.

It must be noted that these findings are not by any means unprecedented for flow over complex surface roughness. In particular there have been several recent experimental studies performed by Nugroho *et al.* [34] and Barros and Christensen [29, 35, 36], which also note spanwise deviations in the mean velocity of turbulent flows and are qualitatively similar to the results shown here. The specific roughness configurations used in these works is however, quite distinct from that shown in Figure 1.3. Nugroho et al. [34] for example, investigated flow over a converging-diverging riblet patterns which created periodic, preferential pathways in the flow, thus causing equivalent effects to those of the current LES through different means.

Christensen *et al.* [29,35,36] looked at flow over surfaces with complex roughness, modeled after actual roughness from a damaged turbine blade. They observed the noted, high and low momentum pathways and showed that LMPs correspond with spanwise locations of low roughness (in a mean streamwise sense), similar to LES results. This is intriguing because the current LES deals with an idealized surface consisting of clearly defined roughness transitions and a large range of roughness ratios. The results found by Christensen et al. are particularly encouraging, because they not only indicate that the current LES results are physically realistic, but also that even for less organized surfaces with small roughness ratios, similar results may be observed.

Some amount of asymmetry is not uncommon in the LES statistics, particularly for cases with low values of λ. For instance, Figure 3.1 (a) and (b), and Figure 3.2 (a) clearly demonstrate asymmetric behavior and exhibit HMPs which are not located over the z_{0H} surface regions. It has been observed that re-running cases under the same initial conditions will often result in noticeably different locations of the low momentum pathways and associated counter rotating vortices. In fact, asymmetry is sometimes observed, slanting in the opposite direction, from that of the previous simulation. However, this should not be entirely surprising due to the turbulence present in the LES flow fields. Because of the low-amplitude random number distributions associated with the initial LES velocity fields, each individual case tends to incline at least slightly in either the positive or negative x_2 direction. This causes preferential pathways to develop, which often persist for large amounts of time after the simulation begins. It has also been shown from instantaneous data, that the HMP-LMP pattern can translate somewhat in a random manner with time. But, from past experience with running the LES code, it is know that restarting a specific case and running it for additional time steps, yields much less disparity in results than resetting the initial velocity field distribution. Thus the asymmetry in time averaged statistics is mostly attributed to the initial velocity field distribution and not to meandering of the pathways over time.

It should also be noted that asymmetry in general is less likely and less dramatic as the values of both λ and L_s/δ increase. This also is not surprising because (as will be discussed in subsequent sections) larger values of λ result in stronger transverse mixing at the surface and thus have a greater effect on the flow. While larger values of L_s/δ result in smaller regions of z_{0L} and thus afford less room for the vortices, which flank the high roughness strips, to drift along the transverse, dimension.

3.2 Coherent Structures

Boundary layer scale, counter-rotating vortices invariably rotate away from z_{0H} roughness strips and into the base of low momentum pathways at the surface. These results are consistent with previous experimental works, which also note counter-rotating vortex pairs flowing into the base of low momentum regions [33–41]. Although, hairpin structures also consist of counter-rotating vortices which rotate into an induced, low-speed flow region [42], a distinction must be made between the counter-rotating vortices in the present study and those often associated with hairpin structures [43–45]. Hairpin structures are short lived and can be detected only through instantaneous data, whereas almost all results presented in the current study, undergo extensive temporal and spatial averaging which makes detection of hairpin structures impossible. This is certainly not to say that hairpin structures do not occur instantaneously in the LES flowfields, but rather that the boundary layer scale counter-rotating vortices shown in Figures 3.1-3.6 are too well structured and stationary to be associated with hairpins.

3.2.1 Vortex Cores

To further illustrate the counter-rotating vortex pairs present in Table 3.1 cases, Figure 3.7 shows contours of "swirling strength", with vectors of secondary flow superimposed for reference. Swirling strength, λ_{ci}, is a visualization technique introduced by Adrian *et al.* [46] in order to identify vortex cores from two-dimensional flow data. Here λ_{ci} is evaluated locally as the imaginary component of the complex eigenvalue obtained from the following matrix:

$$\boldsymbol{D}_{23} = \begin{bmatrix} \dfrac{\partial \langle \tilde{u}_2 \rangle_{t,1}}{\partial x_2} & \dfrac{\partial \langle \tilde{u}_2 \rangle_{t,1}}{\partial x_3} \\ \dfrac{\partial \langle \tilde{u}_3 \rangle_{t,1}}{\partial x_2} & \dfrac{\partial \langle \tilde{u}_3 \rangle_{t,1}}{\partial x_3} \end{bmatrix}. \tag{3.1}$$

To denote rotational direction of the flow, swirling strength values shown in Figure 3.7, λ_{ci} have been signed with the polarity of streamwise vorticity. Thus blue and red λ_{ci} values, correspond with clockwise and counter-clockwise rotation, respectively. As expected λ_{ci} matches well with the counter-rotating vortices shown by secondary flow vectors. To avoid redundancy only cases D1-3 have been shown in Figure 3.7, but similar results are observed with respect to λ_{ci} throughout cases listed in Table 3.1. Images of swirling strength reveal small vortex cores in the immediate vicinity of the roughness transitions, which rotate in the opposite direction of the large scale, secondary vortices. These small vortex cores are thought to be caused by the turbulent mixing processes taking place at roughness transitions.

Note that Figure 3.7 (b) and (c) shows vortices which come into direct contact with each other, approximately half way between the high roughness strips. However when $L_s/\delta \approx 0.2$ in panel (a), the vortices forming on either side of the high roughness strips, are too far apart to come directly into contact with each other. This has no effect on vertical momentum over $z_{0,H}$ roughness, which is driven by mixing at roughness transitions. But as a consequence of decoupled vortices such as those in Figure 3.7 (a), transverse flow is relatively small for cases with $L_s/\delta \approx 0.2$, compared to those with $L_s/\delta \approx 0.6$ and 1.0. The reason for this is that whether vortices meet over the center of $z_{0,L}$ or not, angular momentum of the vortices appears to be unaffected. However, the total, horizontal distance traveled by mean secondary flow around the vortices, becomes longer when the vortices extend to the center of the low roughness regions. Thus greater horizontal momentum is required for coupled, than for decoupled voretices.

One quantity that is commonly of interest when describing the effects of local surface heterogeneities is the blending height, h_b [47], defined as the elevation at which effects of local surface heterogeneities are blended out by turbulent mixing [2]. Determination of a blending height is sometimes desired for ABL flows, because it is useful for predicting the elevation at which Monin-Obukhov similarity theory (MOS) [28] may be accurately applied. However, because the vortices observed here are on

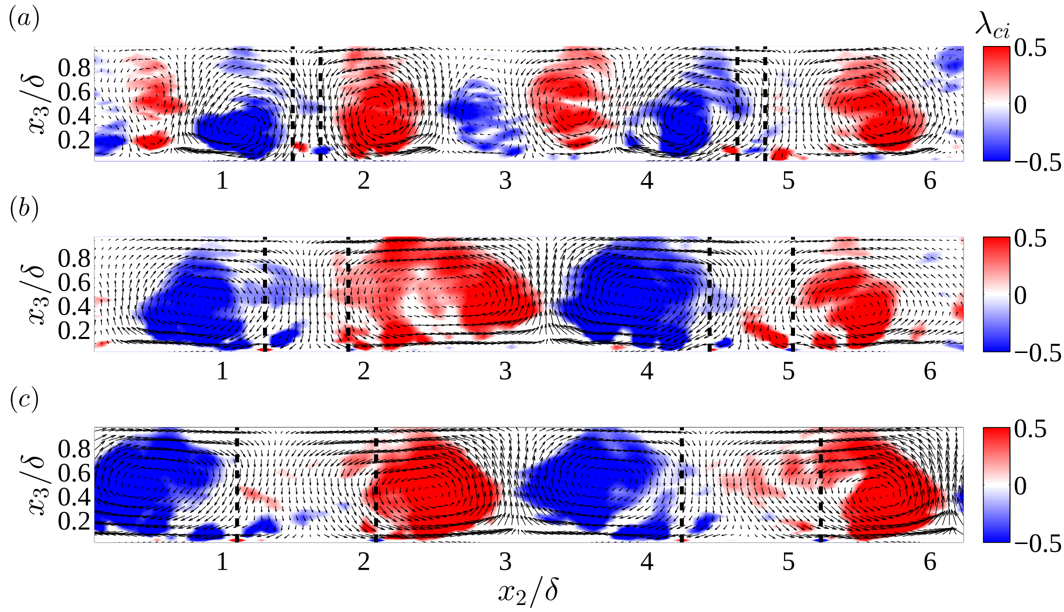

Figure 3.7: Black vectors of secondary flow components, $\{\langle\tilde{u}_2\rangle_{t,1}/u_\tau, \langle\tilde{u}_3\rangle_{t,1}/u_\tau\}$, superimposed over contours of swirling strength, λ_{ci}, from cases D1-3.

the order of the boundary layer, it is clear that effects of the spanwise varying surface roughness, affect the flow to some extent throughout the entire domain. Therefore it is concluded that any estimation of a blending height is not valid for the current domain height. There have been a number of studies, that have considered flow over perpendicularly aligned step-changes in roughness (as in Figure 1.3) and found h_b values, that are equivalently much lower than the domain height used in the present simulations [2, 3, 16, 48–50]. This seems to imply that the effects of parallel aligned roughness may actually be detected, at elevations even farther from the surface than those of perpendicular alignment.

3.2.2 Induced Mean Flow Deviations

Figures 3.8-3.10 provide linear profiles of all three velocity components, at elevations of $\approx 0.004\delta$ (left panels: a, d, and g), $\approx 0.035\delta$ (center panels: b, e, and h) and $\approx 0.075\delta$ (right panels: c, f, and i). These profiles demonstrate the effects of

λ and L_s/δ, close to the surface. Notice that for all values of λ and L_s/δ the profiles at the lowest height (panels a, d and g) are monotonic. But as data is taken farther from the surface, the values become increasingly less monotonic due to the weaker influence of surface stress.

From Figures 3.8-3.10 (a)-(c), it can be seen that spanwise locations with roughness length, z_{0H}, cause dramatic decreases in streamwise velocity near the surface. These sharp drops in velocity attenuate higher in the domain and are indistinguishable at only $\approx 7.5\%$ of the domain height. It is observed that maximum values of $\tilde{u}_1$ increase monotonically with increasing λ, but decrease as values of L_s/δ are raised. The reason for this is that a constant surface area is used throughout all simulations. The drag imposed on the flow is directly dependent on the value of L_s/δ and thus as L_s/δ increases, the maximum values of $\tilde{u}_1$ located above z_{0L} roughness regions are lowered by the rise in total drag. This brings to light a key feature of these flows, which is that as L_s/δ is increased the impact of λ is diminished due to smaller transverse velocity gradients.

Profiles of flow in the transverse, $\tilde{u}_2$ direction (shown in panels d-f of Figure 3.8-3.10), exhibit large positive and negative values, on the large and small x_2 coordinate sides of z_{0H} strips, respectively. This corresponds with the presence of counter-rotating vortices discussed previously, which rotate away from the high roughness surface regions. Profiles of $\tilde{u}_2$ have some characteristics in common with those of $\tilde{u}_1$, such as monotonic profiles near the surface which increase with λ, and also attenuating gradients at higher elevations. Interestingly though, dips in $|\tilde{u}_2|$ profiles are observed above roughness transition locations in Figures 3.9 and 3.10. This may be attributed to turbulent mixing taking place at the transitions, which has been shown by Figure 3.7 to cause relatively small vortices that rotate in the opposite direction of the boundary layer scale, counter-rotating flow structures. Nevertheless, it is clear that the mean transverse flow, results in horizontal momentum flux away from high roughness regions, for all cases. As expected, $\tilde{u}_2$ values are smaller with $L_s/\delta \approx 0.2$ in Figures 3.8 (d-f) than with $L_s/\delta \approx 0.6$ and 1.0 in Figure 3.9 and 3.10, respectively. Again this is due to the decoupling of the boundary layer scale, vortices, over $z_{0,L}$ roughness, on either side of the high roughness strips and it shows that this decoupling takes place consistently for cases A-F1.

Profiles of vertical velocity at the surface, seen in Figures 3.8-3.10 (g), show monotonically increasing absolute values with respect to increasing λ and decreasing L_s/δ. This is consistent with the rises observed in profiles of $\tilde{u}_1$ and shows that all velocity components are directly influenced by both λ and L_s/δ. One notable difference seen in the $\tilde{u}_3$ profiles however, is that the extreme values of $\tilde{u}_3$ increase significantly at locations farther away from the surface (shown in panels h and i of Figures 3.8-3.10). This again is consistent with the boundary layer scale counter-rotating vortex pattern discussed previously. It is clear, upon inspection, that the positive and negative swells of $\langle \tilde{u}_3 \rangle_{t,1}/u_\tau$ profiles in Figures 3.8-3.10 (h) and (i), conform to the notion of vortices which rotate downward towards $z_{0,H}$ roughness and upwards over z_{0L} roughness.

Another feature of the $\tilde{u}_3$ profiles to take note of, is that there are noticeable decreases in $\tilde{u}_3$ located over low roughness, just beyond transition lines in Figures 3.8-3.10 (g). This is to be expected based on the counter-rotating vortices flowing downwards over transition locations. Yet just inside the transition lines, over high roughness, there are actually small increases in $\langle \tilde{u}_3 \rangle_{t,1}/u_\tau$ profiles. This again is likely due to turbulent mixing at the roughness transitions which opposes the motion of the

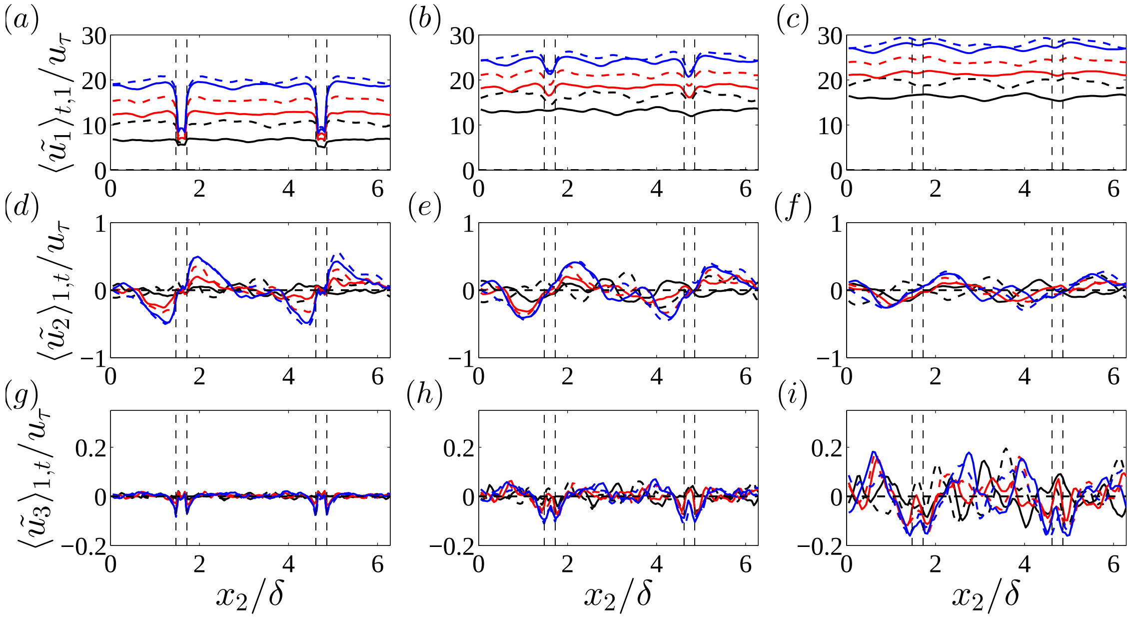

Figure 3.8: Profiles of velocity components from cases A1 (solid black), B1 (dashed black), C1 (solid red), D1 (dashed red), E1 (solid blue) and F1 (dashed blue) taken at heights of $x_3/\delta \approx 0.001$ (panels a, d and g), $x_3/\delta \approx 0.02$ (panels b, e and h) and $x_3/\delta \approx 0.04$ (panels c, f and i). This color assignment scheme for λ is continued throughout Chapter 3. Thin, dashed black lines placed at 0.0 on vertical axes and at roughness transitions, for reference.

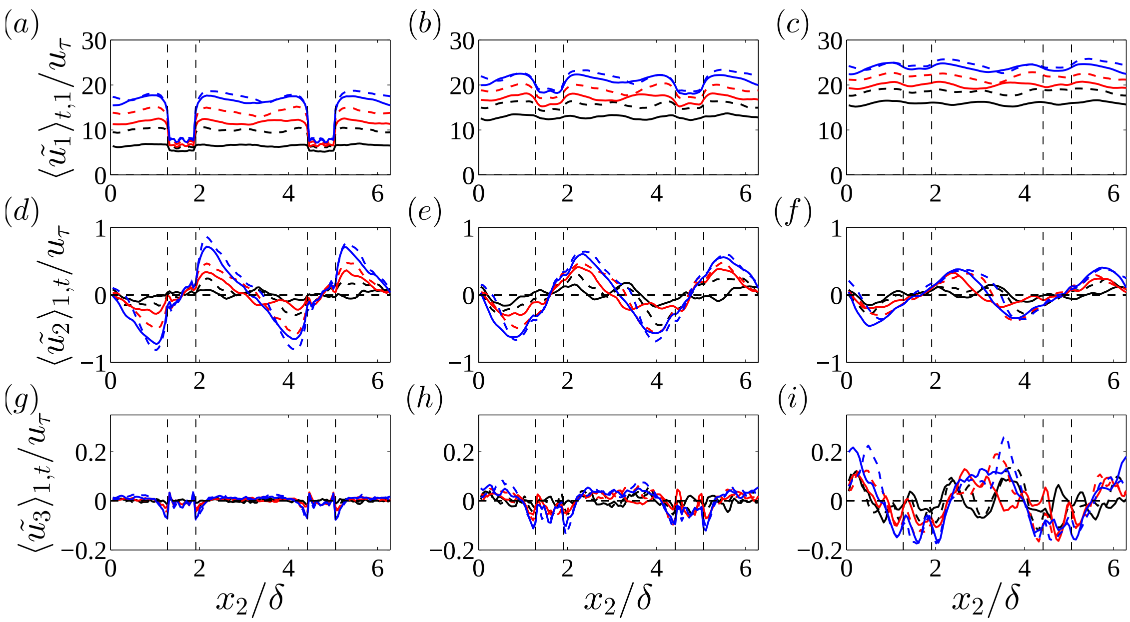

Figure 3.9: Profiles of velocity components from cases A-F2 taken at heights of $x_3/\delta \approx 0.001$ (panels a, d and g), $x_3/\delta \approx 0.02$ (panels b, e and h) and $x_3/\delta \approx 0.04$ (panels c, f and i).

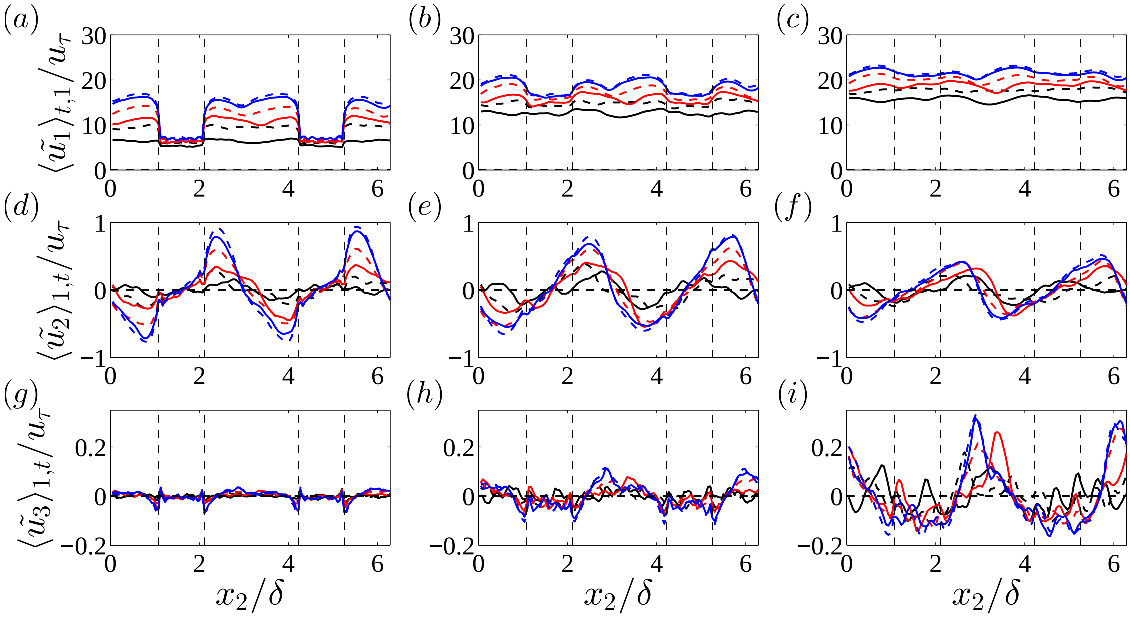

Figure 3.10: Profiles of velocity components from cases A-F3 taken at heights of $x_3/\delta \approx 0.001$ (panels a, d and g), $x_3/\delta \approx 0.02$ (panels b, e and h) and $x_3/\delta \approx 0.04$ (panels c, f and i).

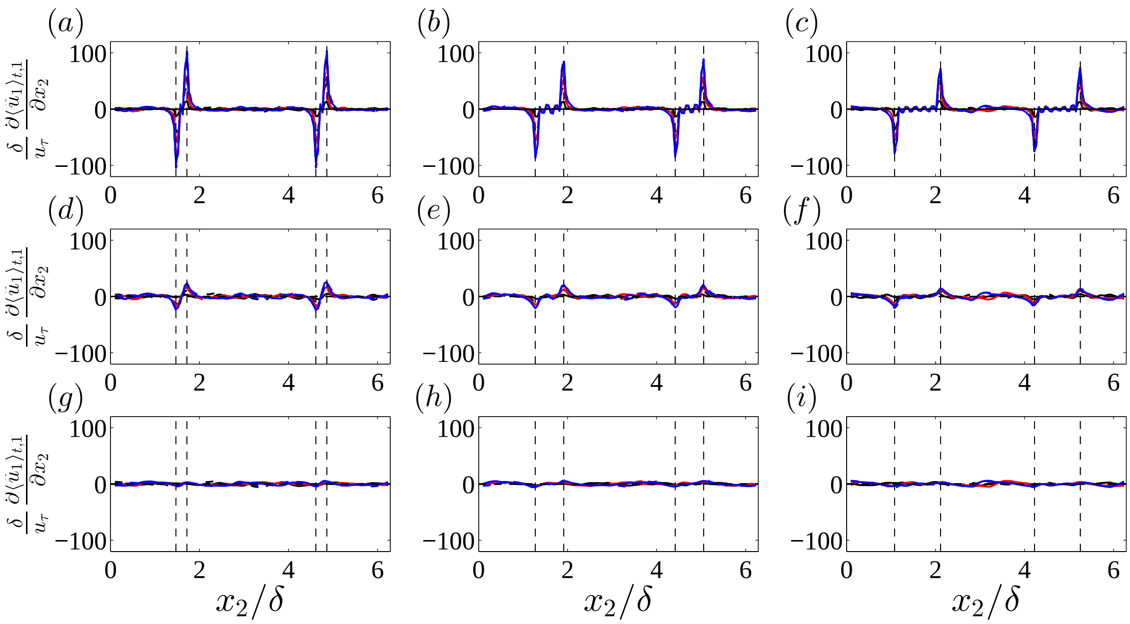

Figure 3.11: Profiles of transverse gradients, in streamwise velocity, from cases A-F1 (panels a, d and g), A-F2 (panels (b,e and h) and A-F3 (panels c, f and i) taken at heights of $x_3/\delta \approx 0.001$ (panels a-c), $x_3/\delta \approx 0.02$ (panels d-f) and $x_3/\delta \approx 0.04$ (panels g-i).

boundary layer scale counter-rotating vortices and causes the observed upwards flows to be seen, just within the high roughness regions. Figure 3.11 shows profiles of transverse gradients in streamwise velocity, $\frac{\delta}{u_\tau}\partial\langle\tilde{u}_1\rangle_{t,1}/\partial x_2$, averaged in time and the streamwise direction. These profiles demonstrate the relative impact of both λ and L_s/δ on velocity gradients at the same elevations as profiles in Figures 3.8-3.10. Profiles of $\frac{\delta}{u_\tau}\partial\langle\tilde{u}_1\rangle_{t,1}/\partial x_2$ show dramatic positive and negative peaks at the high and low x_2 sides of z_{0H} strips, respectively. Note that this corresponds with the sizable drops and rises found in Figures 3.8-3.10 (a)-(c). As with profiles of $\tilde{u}_1$ and $\tilde{u}_3$, the effects on $\frac{\delta}{u_\tau}\partial\langle\tilde{u}_1\rangle_{t,1}/\partial x_2$ become monotonically more dramatic as λ increases and less dramatic as L_s/δ increases. It is further noted that as $\frac{\delta}{u_\tau}\partial\langle\tilde{u}_1\rangle_{t,1}/\partial x_2$ moves farther from the surface in Figure 3.11 (d)-(f), the extreme values located at the transitions become much less prominent and by only $\approx 7.5\%$ of the domain height in Figure 3.11 (g)-(i)), $\frac{\delta}{u_\tau}\partial\langle\tilde{u}_1\rangle_{t,1}/\partial x_2$ profiles are nearly uniform. Upon close inspection, it is seen that at a certain point the maximum absolute values of $\frac{\delta}{u_\tau}\partial\langle\tilde{u}_1\rangle_{t,1}/\partial x_2$ tend to shift away from above the roughness transitions to locations near the center of the z_{0L} regions. Figure 3.11 (i), which shows visibly detectable dips and rises in profiles near the domain center, moving in the positive x_2 direction. These variations in $|\frac{\delta}{u_\tau}\partial\langle\tilde{u}_1\rangle_{t,1}/\partial x_2|$ at higher elevations (where $|...|$ indicates absolute value), correspond with the presence of low momentum pathways. To further illustrate this phenomenon, Figure 3.12 plots absolute x_2/δ distance of $\max(|\partial\langle\tilde{u}_1\rangle_{t,1}/\partial x_2|)$ from the nearest roughness transition, for case C2. This figure indicates that mixing between high and low momentum flows, across roughness transitions, is not significant for this case, above $\approx$ 10-15% of the domain height.

Another consequence of the counter-rotating vortices is vertical momentum flux which effectively "pulls" high momentum down towards the high roughness and

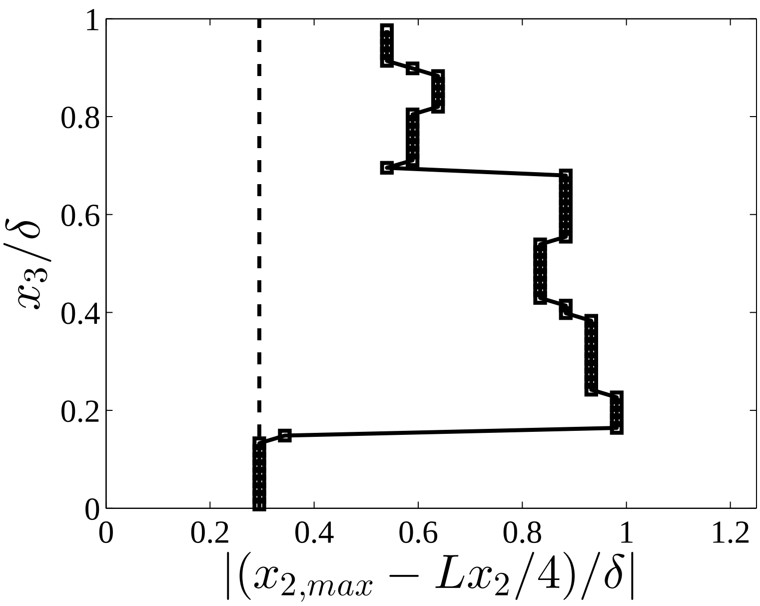

Figure 3.12: Absolute value of transverse distance between $Lx_2/(4\delta)$ and location of $\max(|\partial\langle\tilde{u}_1\rangle_{t,1}/\partial x_2|)$ on $0 \leq x_2/\delta \leq \pi$ from case C2. Dashed line represents location of roughness transitions.

"pumps" low momentum up away from the low roughness. The result of this is the formation of the noted HMP-LMP pattern and also local variations of the boundary layer, as will be shown further on in this chapter. In Figure 3.13 actual streamwise velocity values are compared as a function of height, with theoretical values found using the logarithmic law of the wall:

$$u_{Log} = \frac{u_\tau}{\kappa} \ln\left[\frac{x_3}{z_0}\right]. \tag{3.2}$$

3.3 Stress Effects

3.3.1 Surface Stress

It must be emphasized that spanwise variations in surface roughness length are the only requirement for creating all flow effects described in this chapter. Therefore all mean secondary flows and transverse variations in streamwise momentum, found in

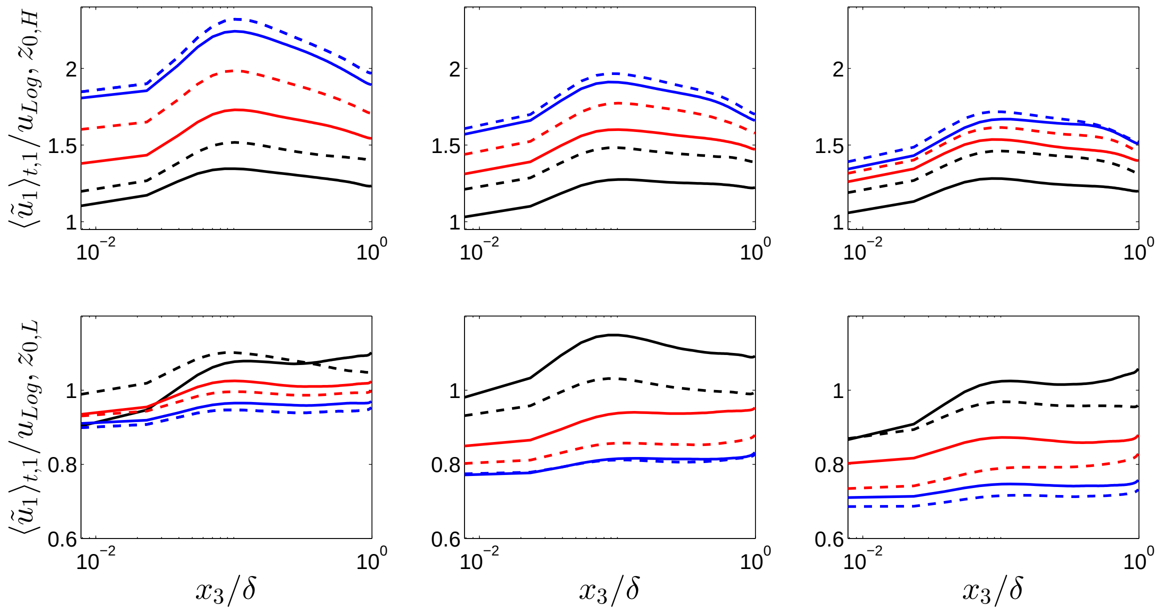

Figure 3.13: Ratios of streamwise LES velocity, $\langle \tilde{u}_1 \rangle_{t,1}/u_\tau$ and log-law velocity, u_{Log}. Top images taken over $z_{0,L}$ roughness at $x_2/\delta = \pi/2$ and bottom images taken over $z_{0,H}$ roughness at $x_2/\delta = \pi/4$. Figures (a) and (d) show cases A-F1, figures (b) and (e) show A-F2 and figure (c) and (f) show A-F3

Table 3.1 cases, are ultimately the result of discontinuities in surface stress. Note that the term "surface stress" is used to refer to vertical stress on streamwise momentum at the lowest computational level of the LES. To gain further insight into the origin of the flow effects, which have been described up to this point, Figures 3.14 show profiles of surface stress for each case listed in Table 3.1. Dotted lines have been added to the vertical axis of Figures 3.14, in order to compare the observed surface stress values with analytical predictions for flow over uniform roughness.

These profiles show sudden rises in magnitude at locations corresponding with high surface roughness, particularly near the roughness transitions. Absolute values of surface stress monotonically increase with λ and decrease with L_s/δ, just as was observed in Figure 3.8-3.10 (a)-(c) profiles, of streamwise velocity near the surface. This is not surprising because stress is assigned at the domain surface using Equations

2.12-2.13 and thus has a direct dependence on velocity. Through lateral momentum flux above the roughness transitions, streamwise flow is sped up near the edges of the $z_{0,H}$ strips and therefore, the largest absolute values of $\langle \tau_{13}^{w} \rangle_{t,1}/u_{\tau}^{2}$ are located in the vicinity of the roughness transitions.

Although $\langle \tau_{13}^{w} \rangle_{t,1}/u_{\tau}^{2}$ follows the same trends with respect to λ and L_s/δ as $\tilde{u}_1$, $\frac{\delta}{u_\tau}\partial \langle \tilde{u}_1 \rangle_{t,1}/\partial x_2$ etc. it should be pointed out that the locations with greatest dependence on λ in Figure 3.14, are located over z_{0H} roughness. However, recall that roughness length is constant for every case in Table 3.1. Therefore the dependence on λ over the z_{0H} strips must be entirely attributed to deviations in streamwise velocity from their logarithmic profiles (described in Figure 3.13), which is caused by lateral momentum flux, initiated by transverse mixing at the roughness transitions.

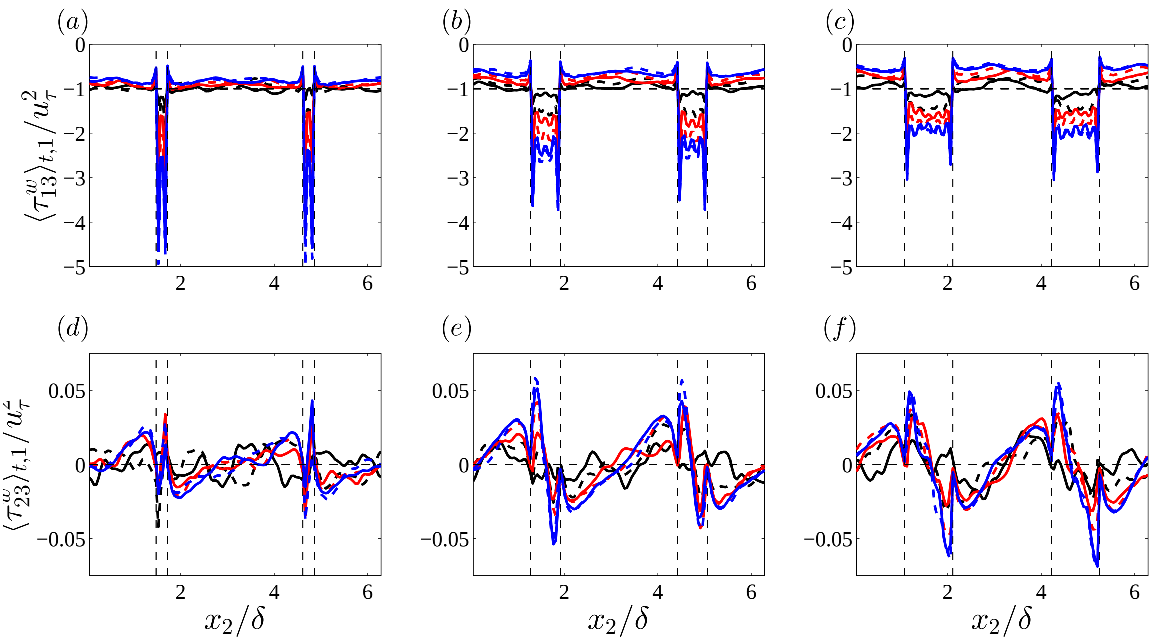

Figure 3.14: Mean profiles of surface stress components: streamwise (figure a-c) and transverse (figure d-f). From cases: A-F1 (figures a and d), A-F2 (figures b and e) and A-F3 (figures c and f).

3.3.2 Transverse Surface Stress

Figure 3.14 (d)-(f) contains profiles of transverse surface stress, $\langle \tau_{23}^{w} \rangle_{t,1}/u_\tau^2$. $\langle \tau_{23}^{w} \rangle_{t,1}/u_\tau^2$ is dependent on $\tilde{u}_2$ according to Equation 2.13 and thus follows similar trends to those found in Figures 3.8-3.10 (d). As in profiles of $\langle \tilde{u}_2 \rangle_{t,1}/u_\tau$, drops in $|\langle \tau_{23}^{w} \rangle_{t,1}/u_\tau^2|$ are seen at transition locations and generally smaller $|\langle \tau_{23}^{w} \rangle_{t,1}/u_\tau^2|$ is seen for $L_s/\delta \approx 0.2$, in panel (d). Profiles in Figure 3.14 (d), are highly inconsistent with those in panels (e) and (f), at locations over the $z_{0,H}$ roughness regions. A possible explanation for this is that $L_s/\delta \approx 0.2$ is not sufficiently wide for the largest scales of mixing taking place at roughness transitions, to be decoupled across $z_{0,H}$ roughness strips. This is consistent with Figure 3.7 (a), which shows widened, overlapping vortex cores associated with mixing. Thus mixing may affect mean secondary flow near the surface, across the entire $z_{0,H}$ strips, rather than only the roughness transitions, for cases with $L_s/\delta \approx 0.2$.

3.3.3 Transverse Shear Stress

In the proximity of the roughness transitions, discontinuities in surface stress impose large spanwise gradients on streamwise velocity as shown by profiles in Figure 3.15. This creates turbulent shearing layers between the adjacent flow regions over high and low roughness. Such shearing between parallel flows has been considered extensively in previous literature [51, 52]. Vermaas *et al.* [53] conducted open channel flow experiments using acoustic Doppler velocimetry, to investigate the lateral exchange of streamwise momentum caused by a parallel roughness transition. These roughness transitions are similar to those considered in the present study, although only a single transition was used rather than a transversely periodic pattern. They also, noted significant increases in horizontal shear stress in the vicinity of their roughness transitions, consistent with those encountered here.

Figure 3.15 considers profiles of $\langle T_{12}\rangle_{t,1}/u_\tau^2$ (where $\langle T_{12}\rangle_t$ values are obtained through Equation 2.14) for all cases in Table 3.1 and reveals a large amount of transverse shearing, generated in close proximity to each roughness transition. The transverse shearing here corresponds with locally increased production of turbulence at the roughness transitions, similar to the findings of Vermaas 2011 [53], Hoagland 1960 [54] and Hinze 1967 [55]. This horizontal shearing is also the driving force behind all turbulent mixing taking place at roughness transitions.

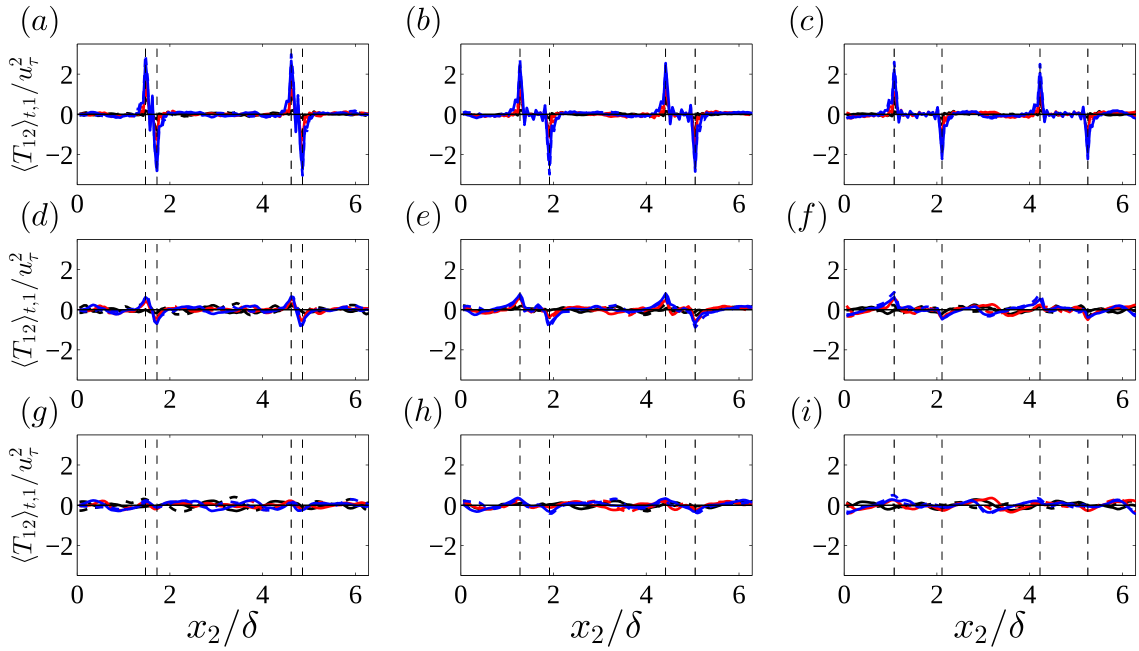

Figure 3.15: Profiles of transverse shear stress, from cases A-F1 (panels a, d and g), A-F2 (panels (b,e and h) and A-F3 (panels c, f and i) taken at heights of $x_3/\delta \approx 0.001$ (panels a-c), $x_3/\delta \approx 0.02$ (panels d-f) and $x_3/\delta \approx 0.04$ (panels g-i).

$\langle T_{12}\rangle_{t,1}/u_\tau^2$ profiles show positive and negative peak locations, which are opposite of those found in the $\frac{\delta}{u_\tau}\partial\langle\tilde{u}_1\rangle_{t,1}/\partial x_2$ profiles of Figure 3.11. This indicates that transverse shear stress is directly caused by transverse gradients of streamwise velocity, which are in turn caused by spanwise heterogeneities in surface stress, $\langle\tau_{13}^w\rangle_{t,1}/u_\tau^2$. As seen frequently in preceding statistics, such as $\langle\tilde{u}_1\rangle_{t,1}/u_\tau$, $\frac{\delta}{u_\tau}\partial\langle\tilde{u}_1\rangle_{t,1}/\partial x_2$ and $\langle\tau_{13}^w\rangle_{t,1}/u_\tau^2$, the maximum and minimum peaks of $\langle T_{12}\rangle_{t,1}/u_\tau^2$ are observed to increase

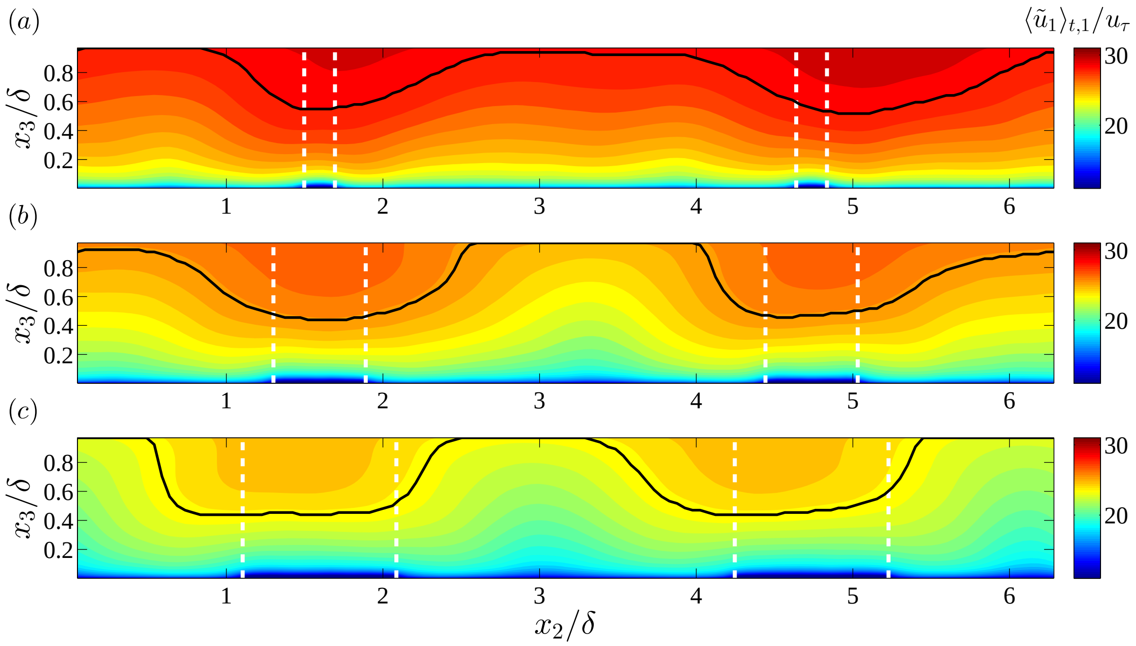

Figure 3.16: Solid black line denoting height of local boundary layer thickness, superimposed over contours of streamwise velocity, for cases D1 (figure a), D2 (figure b) and D3 (figure c).

and decrease with λ and L_s/δ, respectively, and to swiftly attenuate with increasing distance from the surface. This further supports the idea that $\langle T_{12} \rangle_{t,1}$ is driven by $\partial \langle \tilde{u}_1 \rangle_{t,1}/\partial x_2$ and that $\langle T_{12} \rangle_{t,1}/u_\tau^2$ profiles are ultimately caused by the same underlying mechanisms as those of $\langle \tilde{u}_1 \rangle_{t,1}/u_\tau$, $\frac{\delta}{u_\tau}\partial \langle \tilde{u}_1 \rangle_{t,1}/\partial x_2$ etc., namely, step-changes in surface roughness length.

3.4 Variations of Local Boundary Layer Thickness

One aspect of the flows fields shown by Figures 3.8-3.10 which may be somewhat counterintuitive at first glance, is the location of HMPs and LMPs, over z_{0H} and z_{0L} roughness regions, respectively. It has been shown in Figure 3.8-3.10 that velocity profiles at the surface, experience sharp drops over z_{0H} roughness due to increased drag, and one might intuitively expect this trend to continue throughout the entire domain. However, due to secondary flow, caused by mixing above the roughness transitions, it turns out that this is not the case. The boundary layer scale, counter-rotating vortices transport momentum vertically throughout the domain, which results in spanwise variation of local boundary layer thickness. This effect was noted previously by Nugroho *et al.* [34] in their study of flow over converging-diverging riblets.

Figure 3.16 shows several cases depicting streamwise averaged contours of boundary layer height. Local boundary layer height is defined here as the lowest x_3/δ location at which $\langle \tilde{u}_1 \rangle_{t,1}/u_\tau = 0.98U_\infty$, where U_∞ represents free stream velocity and is defined as the mean streamwise velocity at the top of the domain. Local boundary layer heights are denoted by continuous black lines, superimposed over contours of $\langle \tilde{u}_1 \rangle_{t,1}/u_\tau$. Figure 3.16 shows that the large scale secondary flows, generally result in local decreases of the boundary layer thickness above z_{0H} roughness and local increases of the boundary layer thickness above z_{0L} roughness. This explains the observed pattern of high and low momentum pathways, located over high and low surface roughness, respectively. Flow over z_{0H} roughness is actually outside the boundary layer and has reached free stream velocity, while flow over z_{0L} roughness has essentially been pulled deeper inside the boundary layer, thus resulting in the observed flow features. Note that despite local thinning of boundary layers, δ_i/z_{0H} ratios are still comfortably above ≈ 80 at all points, this is important because for $\delta_i/z_{0H} \lessapprox 80$ the simulations could be considered flow over obstacles rather than surface roughness [12].

3.5 Turbulence Effects

Figures 3.17-3.19 shows profiles of Reynolds normal stress, $\langle T_{ii} \rangle_{t,1}/u_\tau^2$, where Reynolds stress components are obtained through Equation 2.14. Reynolds normal stresses are shown at the same three elevations as profiles of Figures 3.8-3.10, with ascending values moving from the left to right side of each figure. All profiles taken at the lowest elevation (Figure 3.17-3.19 a, d and g), exhibit sharp rises in normal stress around the roughness transitions. This confirms that the formation of shearing layers and transverse mixing in this area, corresponds with enhanced turbulence production over $z_{0,H}$ roughness. As could be expected based on Equation 2.14, rises in $\langle T_{11}\rangle_{t,1}/u_\tau^2$ and $\langle T_{22}\rangle_{t,1}/u_\tau^2$ shown in Figure 3.17-3.19 (a), (d) and (g) correspond with rises in the absolute value of Figure 3.15 (a), (d) and (g). The maximum absolute values in normal stress, increase with larger λ and decrease with larger L_s/δ, except for $\langle T_{22}\rangle_{t,1}/u_\tau^2$ in Figure 3.17 (d)-(f), due to the lower transverse momentum shown in Figure 3.8 (d)-(f). This demonstrates a correlation between absolute values of shear stress profiles and the generation of turbulence in the lower section of the domain. Normal stresses are notably smaller over the high roughness regions in panels (a), (d) and (g) of Figures 3.17-3.19. This is due to the sharp decreases in momentum at these locations, shown in Figures 3.8-3.10 (a). But note that proportionally equal growth takes place in normal stresses at this elevation, on both sides of the roughness transitions.

As elevation increases, profiles of normal stresses become increasingly smooth and no longer show abrupt growth at roughness transition locations. This corresponds with the weakening of shear layers with distance from the surface, as shown in Figure 3.15. In Figures 3.17-3.19 panels (b), (c), (e), (f), (h) and (i), normal stress profiles are shown to increase and decrease over high and low roughness, respectively, as the value of λ is raised. It is not surprising that larger normal stresses would be seen for larger λ, above $z_{0,H}$ roughness, due to stronger shearing and mixing which enhance turbulence. It is also not surprising to see lower normal stress values over $z_{0,L}$ roughness, with higher λ, due to stronger secondary flows that pull turbulence away from the low roughness surfaces. However, in Figures 3.17-3.19 panels (a), (d) and (g), monotonically larger values of normal stress are seen across the entire domain. This indicates that the influence of secondary flow is negligible compared to that of aerodynamic drag, near the surface and is consistent with Figures 3.8-3.10 (g), which show low values of vertical flow in the vicinity of $z_{0,L}$ roughness.

Based on Figures 3.17-3.19, it is clear that transverse mixing at the roughness transitions causes locally enhanced turbulence production in the vicinity of high roughness strips. The locations of maximum $\langle T_{11} \rangle_{t,1}/u_\tau^2$ are located directly over roughness transitions, while maximum values of $\langle T_{22} \rangle_{t,1}/u_\tau^2$ and $\langle T_{33} \rangle_{t,1}/u_\tau^2$ take place at some distance above the $z_{0,H}$ roughness, as shown in Figure 3.17-3.19 (f), and (i). Streamwise averaged contours of TKE in Figure 3.20, show significantly larger values above $z_{0,H}$ roughness than above $z_{0,L}$ roughness. TKE values becomes increasingly large over $z_{0,H}$ roughness as λ is increased, even though $z_{0,H}$ values are identical throughout all simulations, this must be entirely attributed to increased turbulence, caused by increased mixing around roughness transitions. It has been speculated that enhanced production of TKE in the vicinity of the high roughness regions, is the direct cause of the boundary layer scale, counter-rotating vortices. Consistent with the findings of Hinze 1967 [55], secondary flow is thought to be necessary as a means of transporting high turbulence flow away from $z_{0,H}$ roughness regions and pulling low turbulence flow towards $z_{0,H}$ roughness. At the present this is only theoretical, but it is expected that in in future works, analysis of TKE budgets may provide crucial insight into the driving forces, responsible for the observed flow field characteristics.

Due to the large scale, secondary flows which rotate downwards towards areas of high roughness and upwards from areas of low roughness, momentum and turbulence are redistributed throughout the entire domain. As shown by Figure 3.13, flow over high roughness is pulled downwards towards the surface while flow over low roughness is pumped vertically away from the surface. High turbulence shows similar effects to low momentum as a result of secondary flow. This is illustrated in Figure 3.21 which shows root-mean-squared deviations in local velocity, from spanwise averaged values, where root-mean-squared deviations are calculated as

$$\tilde{u}'_{RMS,1} = \sqrt{\overline{[\langle\tilde{u}_1\rangle_t - \tilde{u}_1]^2}}. \tag{3.3}$$

Temporal averaging is used in Equation 3.3 in order to enable direct comparison to experimental results such as those of Nugroho *et al.* [34]. Note that for uniform surface roughness, Figure 3.21 would be expected to have uniform values of zero. Near the surface, values in Figure 3.21 are positive and negative over high and low roughness, respectively, which is consistent with Figures 3.17-3.20. However farther

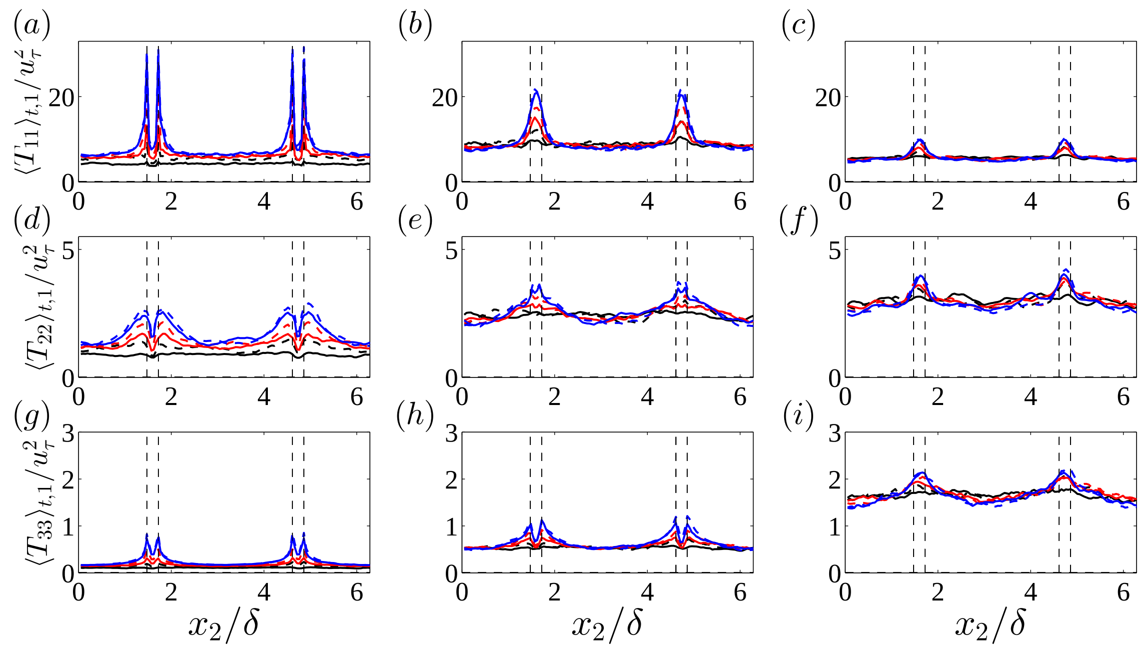

Figure 3.17: Profiles of Reynolds normal stress components, from cases A-F1 taken at heights of $x_3/\delta \approx 0.001$ (panels a-c), $x_3/\delta \approx 0.02$ (panels d-f) and $x_3/\delta \approx 0.04$ (panels g-i).

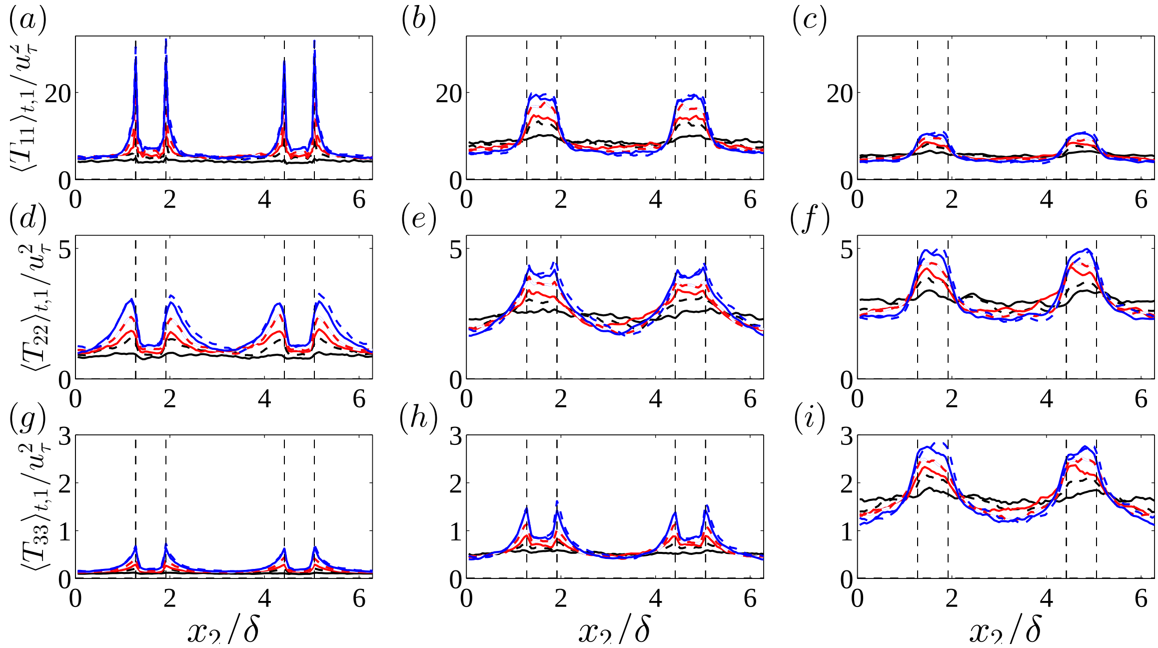

Figure 3.18: Profiles of Reynolds normal stress components, from cases A-F2 taken at heights of $x_3/\delta \approx 0.001$ (panels a-c), $x_3/\delta \approx 0.02$ (panels d-f) and $x_3/\delta \approx 0.04$ (panels g-i).

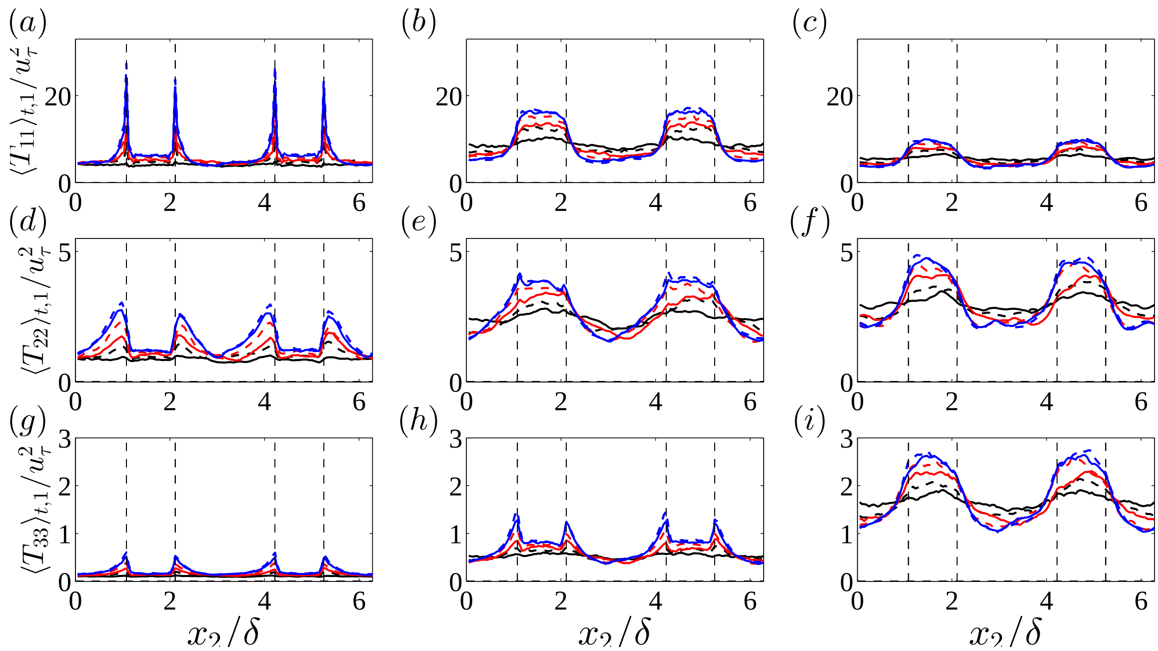

Figure 3.19: Profiles of Reynolds normal stress components, from cases A-F3 taken at heights of $x_3/\delta \approx 0.001$ (panels a-c), $x_3/\delta \approx 0.02$ (panels d-f) and $x_3/\delta \approx 0.04$ (panels g-i).

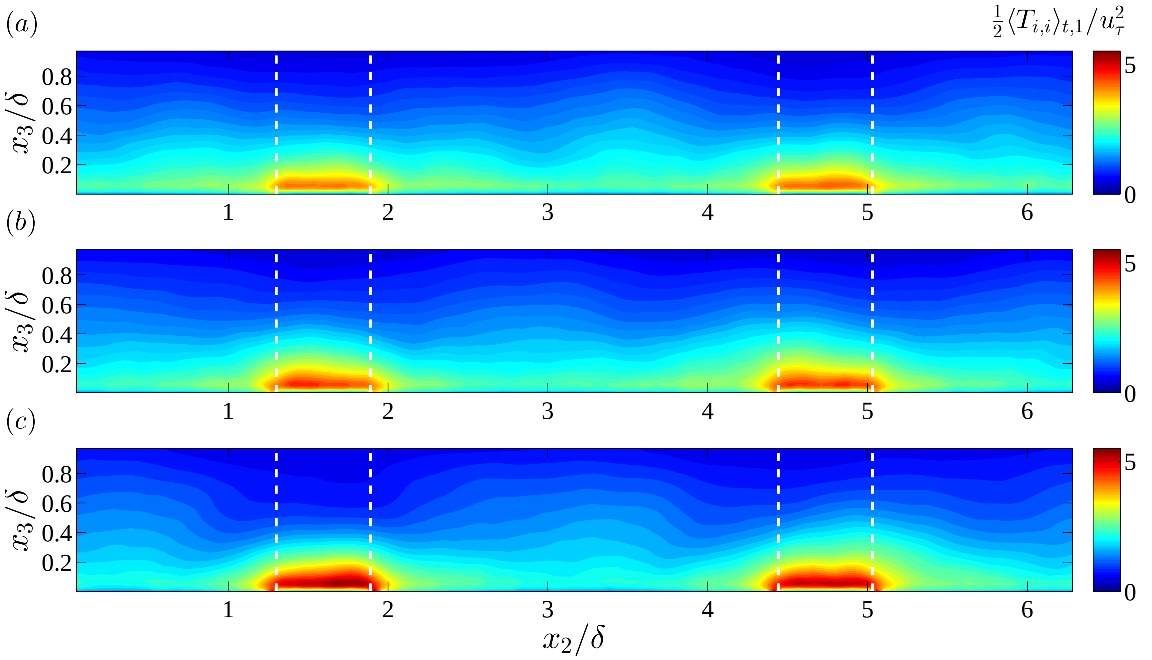

Figure 3.20: Contours of turbulent kinetic energy from cases B2 (figure a), C2 (figure b) and D2 (figure c)

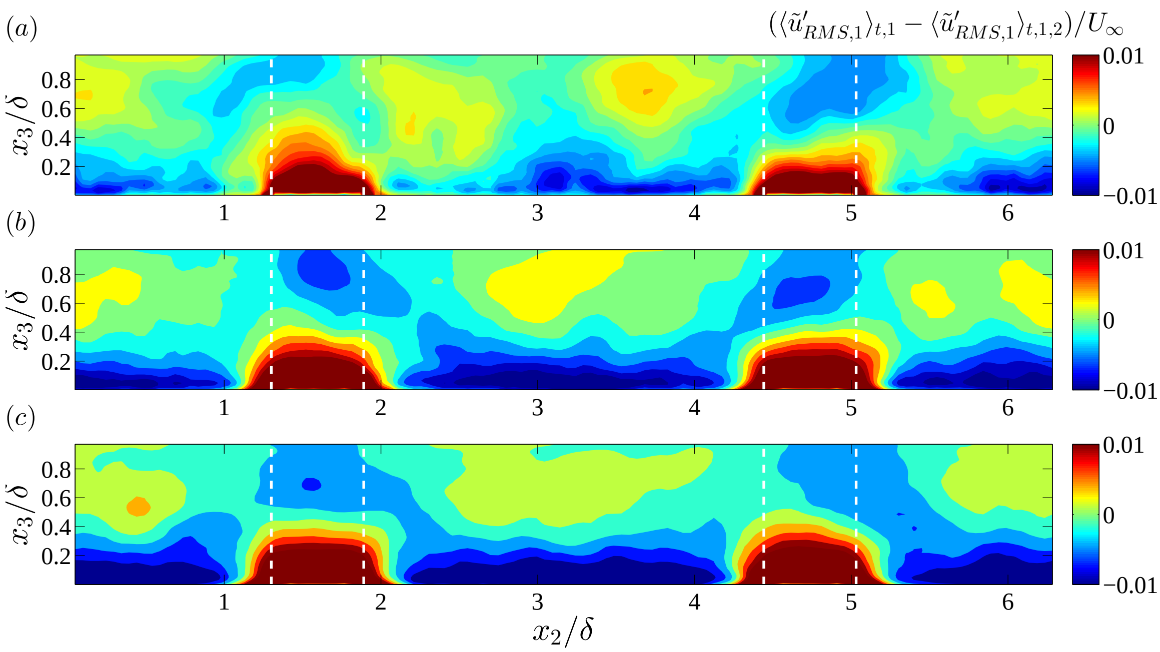

Figure 3.21: Contours showing differences in local and planar averaged turbulent fluctuations from cases B2 (figure a), D2 (figure b) and E2 (figure c).

from the surface, turbulence transport through secondary flows, causes values in Figure [34] to become locally positive and negative above the low and high roughness surface regions, respectively. This reveals that in general, high and low momentum pathways correspond with local reduction of turbulence, while low momentum pathways correspond with local elevation of turbulence. This is entirely consistent with the findings of Nugroho *et al.*

3.6 Quadrant-Analysis

Quadrant-analysis is often used to determine the composition of Reynolds stress, by comparing the relative contributions from the four possible quadrants of the $\{\tilde{u}'_i$-$\tilde{u}'_j\}$ plane : $(\tilde{u}'_i < 0,\ \tilde{u}'_j < 0), (\tilde{u}'_i > 0,\ \tilde{u}'_j < 0), (\tilde{u}'_i < 0,\ \tilde{u}'_j > 0)$ and $(\tilde{u}'_i > 0,\ \tilde{u}'_j > 0)$. Near rough surfaces, wall stress dominates and therefore quadrant analysis is typically done with respect to stress acting on streamwise velocity in the vertical direction (i.e. the $\langle \tilde{u}'_1 \tilde{u}'_3 \rangle_t$ component of Reynolds stress) [56–60]. Turbulent events in the second and fourth quadrants ($\tilde{u}'_1 < 1,\ \tilde{u}'_3 > 1$ and $\tilde{u}'_1 > 1,\ \tilde{u}'_3 < 1$), are classified as "ejections" and "sweeps", respectively. While events in the first and third quadrants ($\tilde{u}'_1 > 1,\ \tilde{u}'_3 > 1$ and $\tilde{u}'_1 < 1,\ \tilde{u}'_3 < 1$), are classified as "outward interactions" and "inward interactions", respectively.

However, in the present study the quantity of greatest interest is the transverse component of Reynolds stress, $\langle \tilde{u}'_1 \tilde{u}'_2 \rangle_t$. Hence, an alternate quadrant splitting scheme, which replaces fluctuations in wall-normal velocity with fluctuations in transverse velocity, is used in an attempt to gain deeper insight into the effects of turbulence and shearing layers in the present flow. Figure 3.22 provides an illustration of this variation on the standard quadrant splitting scheme.

All velocity values are taken at locations directly above the transverse roughness transitions at $x_2/\delta \approx (Lx_2/4 + Ls/2)/\delta$ and $x_2/\delta \approx (3Lx_2/4 + Ls/2)/\delta$ so that

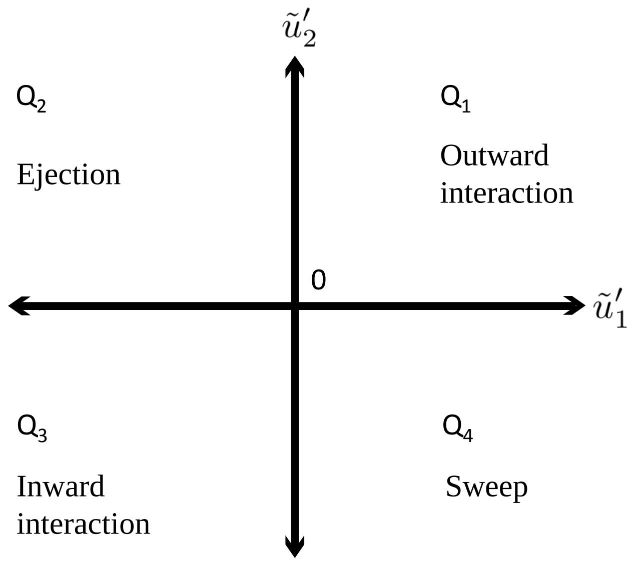

Figure 3.22: Overview of alternate quadrant splitting scheme used

positive values of $\tilde{u}_2'$ correspond with instantaneous rises in transverse momentum, directed away from the high roughness strips. Here sweeps and ejections are relative to the shearing layer formed at the transition as opposed to the surface as for conventional quadrant analysis. Note however, that because $\langle \tilde{u}_2 \rangle_{t,1}/u_\tau$ has positive values at this location, negative $\tilde{u}_2'$ does not necessarily correspond with flow towards the shearing layers.

Figure 3.15 shows that the total transverse shear stress at $x_2/\delta \approx (Lx_2/4 + Ls/2)/\delta$ and $x_2/\delta \approx (3Lx_2/4 + Ls/2)/\delta$ has negative values. Therefore it is to be expected that Q_2 and Q_4 events would dominate over Q_1 and Q_3 events. This is precisely what is observed in Figures 3.23, which shows probability profiles for transverse stress occurring in each of the four quadrants, for cases A-F2. Though only cases A-F1 are shown in Figure 3.23, note that similar trends are also observed in the remaining cases as well. Ejections and sweeps are more numerous at low elevations, as expected. However, at locations higher in the domain, this trend disappears and in some cases, inward and outward flow interactions actually become more frequent

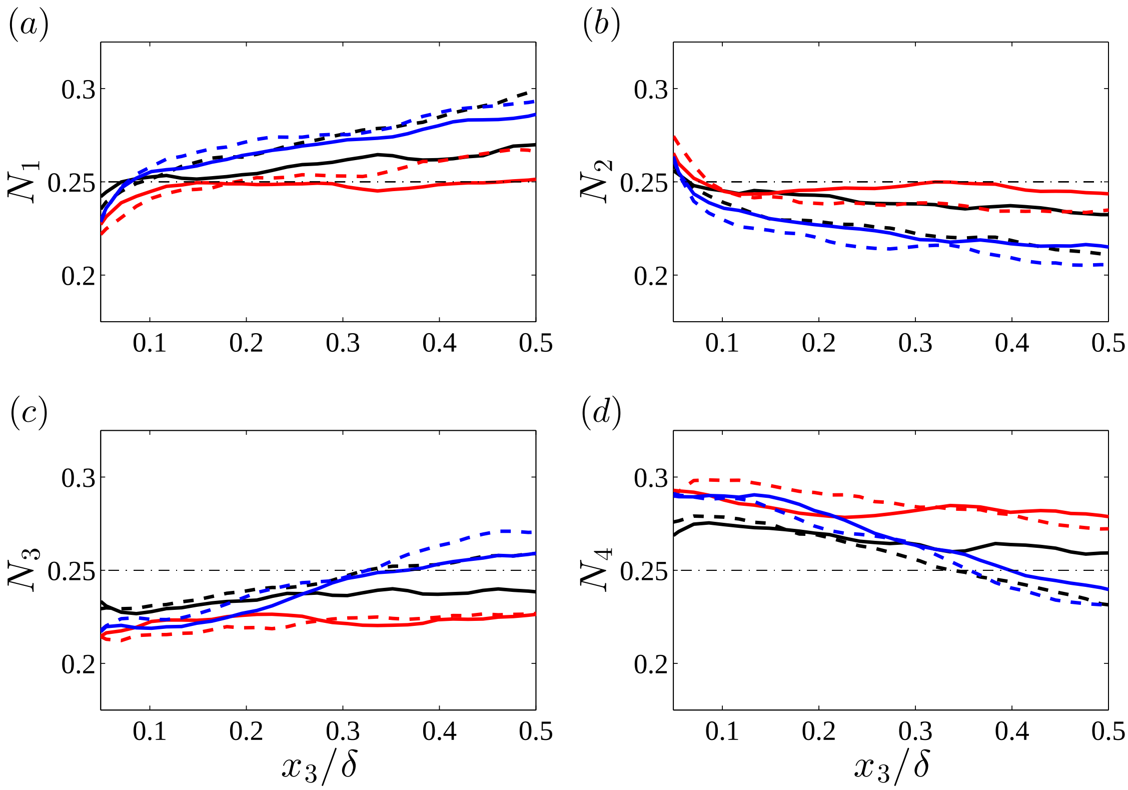

Figure 3.23: Vertical probability profiles of $\langle \tilde{u}_1' \tilde{u}_2' \rangle_{t,1}/u_\tau^2$ quadrant events for cases A-F1. Thin dashed/dotted black line is placed at $N_i = 0.25$ for reference.

due to the reduced influence of lower boundary conditions. Q_4 events are in general more numerous than those of Q_2 and little consistency is observed in profiles with respect to the effects of either Ls/δ or λ. This indicates that the intensity of mixing at roughness transitions does not have a significant influence on the total number of quadrant events.

Mean magnitude profiles of $\langle \tilde{u}_1' \tilde{u}_2' \rangle_{t,1}/u_\tau^2$ quadrant events, are plotted in Figure 3.24 at a constant L_s/δ value of ≈ 0.6. Unlike probability profiles in Figure 3.23, Q_2 profiles in Figure 3.24 clearly surpass Q_4 within the lower $\approx 10\%$ of the domain. Monotonically increasing values are observed for increasing λ and decreasing Ls/δ, which simply implies that all four quadrants of shear stress are affected by higher transverse momentum gradients, as would be anticipated. Near the surface, average

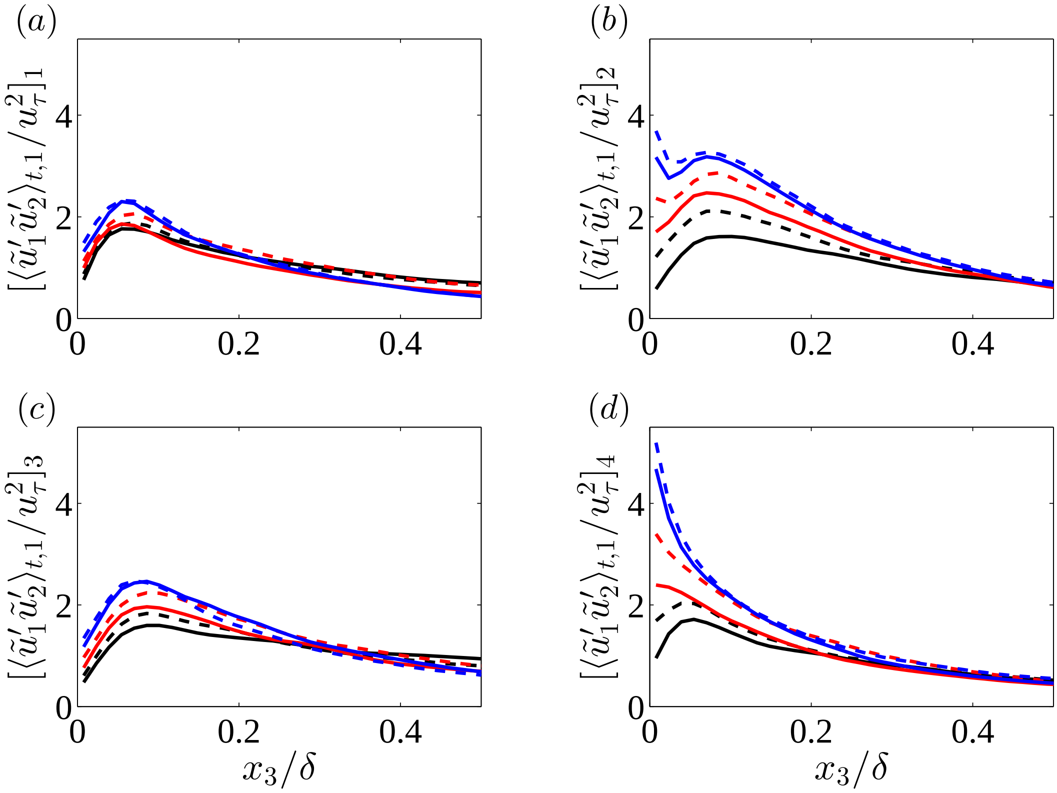

Figure 3.24: Mean magnitude profiles of $\langle\tilde{u}_1'\tilde{u}_2'\rangle_{t,1}/u_\tau^2$ quadrant events, from cases A-F2.

magnitudes of sweeps > ejections > outward interactions ≈ inward interactions. The differences in magnitudes between Q_2-Q_4 and Q_1-Q_3 events, though not as extreme as those typically observed in conventional quadrant analysis [56,57,59,60], are consistent and become more dramatic for cases which feature large velocity gradients. This confirms that these results are the direct consequence of transverse variations in surface roughness.

In order to determine the relative impact of sweeps compared with ejections, the total contributions of Q_2/Q_4 events are computed at all elevations, for all cases, in Figure 3.25. These images show that below $\approx 0.1\delta$, sweeps make more significant contributions to transverse Reynolds stress than ejections, but above $\approx 0.1\delta$ the opposite of this is found to be true. Because contributions of sweeps and ejections,

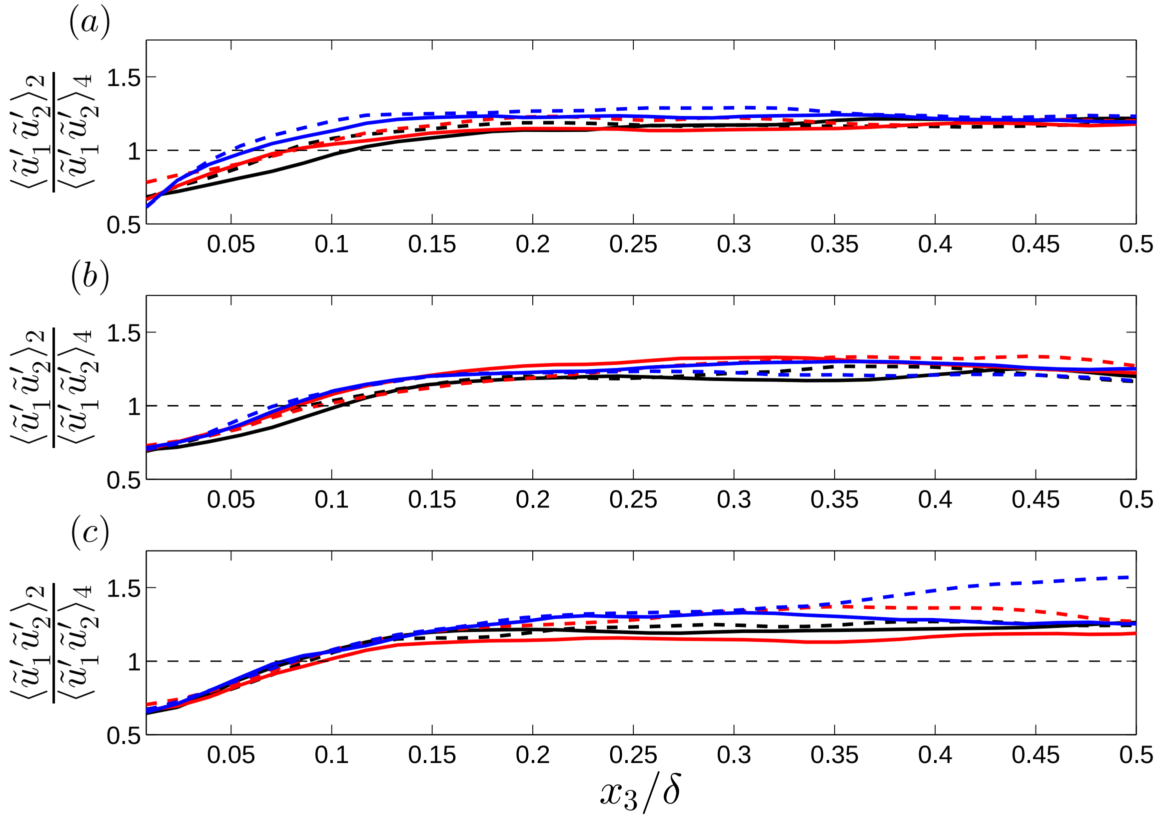

Figure 3.25: Ratios of the total contribution to Reynolds shear stress by Q_2 vs. Q_4 events, from cases A-F1 (figure a), A-F2 (figure b) and A-F3 (figure c).

shown in Figure 3.25, are not significantly monotonic with respect to either λ or Ls/δ, it may be inferred that the contributions from Q_2 and Q_4 events, scale proportionally as shear layers become stronger. Thus the fundamental nature of the mixing process does not appear to be dependent on either λ or L_s/δ.

These results are strikingly similar to quadrant analysis performed in previous studies of flow over rough surfaces with the standard $\{\tilde{u}_1', \tilde{u}_3'\}$ quadrant splitting scheme [56, 57, 59, 60]. It has been observed in studies such as these, that in flow past rough surfaces, sweeps contribute more heavily to Reynolds stress than ejections close to the wall, while farther from the wall, sweeps contribute less than ejections. This implies that surface stress in general, tends to sweep high momentum inwards and eject low momentum outwards from the surface. The results shown in Figures 3.23- 3.25 indicate that an analogous process takes place at shear layers formed over roughness transitions in the $\{x_1/\delta,\ x_2/\delta\}$ plane. In this case, transverse shear stress serves to sweep high momentum towards shear layers at roughness transitions and eject low momentum outwards, away from the roughness transitions.

3.7 Turbulent Mixing Length

In order to further describe the mixing taking place near the roughness transitions, transverse turbulent mixing lengths have been calculated. Physically, these mixing lengths represent the smallest scale of eddies, associated with the turbulent mixing process. Mixing length here is calculated using a method similar to that of Bai *et al.* [61] In their study, Bai *et al.* used particle image velocimetry to consider the turbulent flow structure and mixing length associated with wakes, downstream of a synthetic, fractal-like tree. They made use of the Boussinesq model [62], which provides a basis for many turbulence models, to evaluate mixing length scales, relevant to momentum transport. For incompressible flow, the Boussinesq model can be expressed as:

$$\frac{T_{ij}}{\rho} = -\nu_T\left(\frac{\partial \tilde{u}_i}{\partial x_j} + \frac{\partial \tilde{u}_j}{\partial x_i}\right) + \frac{2}{3}\delta_{ij}k, \tag{3.4}$$

where T_{ij} is the tensor for turbulent Reynolds stress, ν_T is turbulent eddy-viscosity, δ_{ij} is the Kronecker delta and $k = \frac{1}{2}\overline{u'_m u'_m}$ is turbulent kinetic energy. Considering exclusively transport in the horizontal, x_2, direction and recalling that all statistics in the present study have uniform streamwise means, Equation 3.4 can be reduced to

$$\frac{\langle T_{12}\rangle_{t,1}}{\rho} = -\nu_T\frac{\partial\langle\tilde{u}_1\rangle_{t,1}}{\partial x_2}. \tag{3.5}$$

Equation 3.5 may be solved for ν_T to yield:

$$\nu_T(x_3) = -\frac{\langle T_{12}\rangle_{t,1}}{\rho}\bigg/\frac{\partial\langle\tilde{u}_1\rangle_{t,1}}{\partial x_2}. \tag{3.6}$$

Which implies the value of ν_T can be obtained through a simple linear relationship between $\langle T_{12}\rangle_{t,1}$ and $\partial\langle\tilde{u}_1\rangle_{t,1}/\partial x_2$, both of which are known quantities and have been discussed in previous sections of this chapter. Therefore, from Equation 3.6, ν_T may be obtained in non-dimensional form as a function of x_3/δ, by plotting data points of $\langle T_{12}\rangle_{t,1}/u_\tau^2$ vs. $\frac{\delta}{u_\tau}\partial\langle\tilde{u}_1\rangle_{t,1}/\partial x_2$ and applying a linear least squared fit, to find the negative value of the slope. Examples of such data fitting are shown in Figure 3.26 at x_3/δ locations of ≈ 0.001, ≈ 0.035 and ≈ 0.075. These figures show steeper (more negative) slopes at larger x_3 positions, which indicates a rise in ν_T with distance from the surface.

Profiles of ν_T are plotted in Figure 3.27 for each case in Table 3.1. In this figure, ν_T is clearly shown to grow larger with increasing x_3/δ, near the bottom of the domain, in accordance with Figure 3.26. Figure 3.27 also shows values which increase monotonically with λ at the surface, but become much less consistent by $\approx 15\%$ of the domain height and seem to actually demonstrate reverse trends (i.e. decreasing ν_T with increasing λ values) above this. This is consistent with the results of $\langle T_{12}\rangle_{t,1}/u_\tau^2$ and $\frac{\delta}{u_\tau}\partial\langle\tilde{u}_1\rangle_{t,1}/\partial x_2$ shown in Figures 3.15 and 3.11, which do not maintain monotonic trends at any locations other than those in the immediate vicinity of the surface. Fortunately, the only values of real interest here, are those at low x_3/δ positions, because the transverse mixing length is only associated with the intense transverse mixing process ongoing at roughness transitions.

The Equation used to calculate mixing lengths here, makes use of Prandtls mixing length model, which states that

$$\nu_T = l u_c \tag{3.7}$$

where u_c is a characteristic velocity and l is a length associated with scales of mixing. The characteristic velocity is typically expressed as the product of l and the absolute

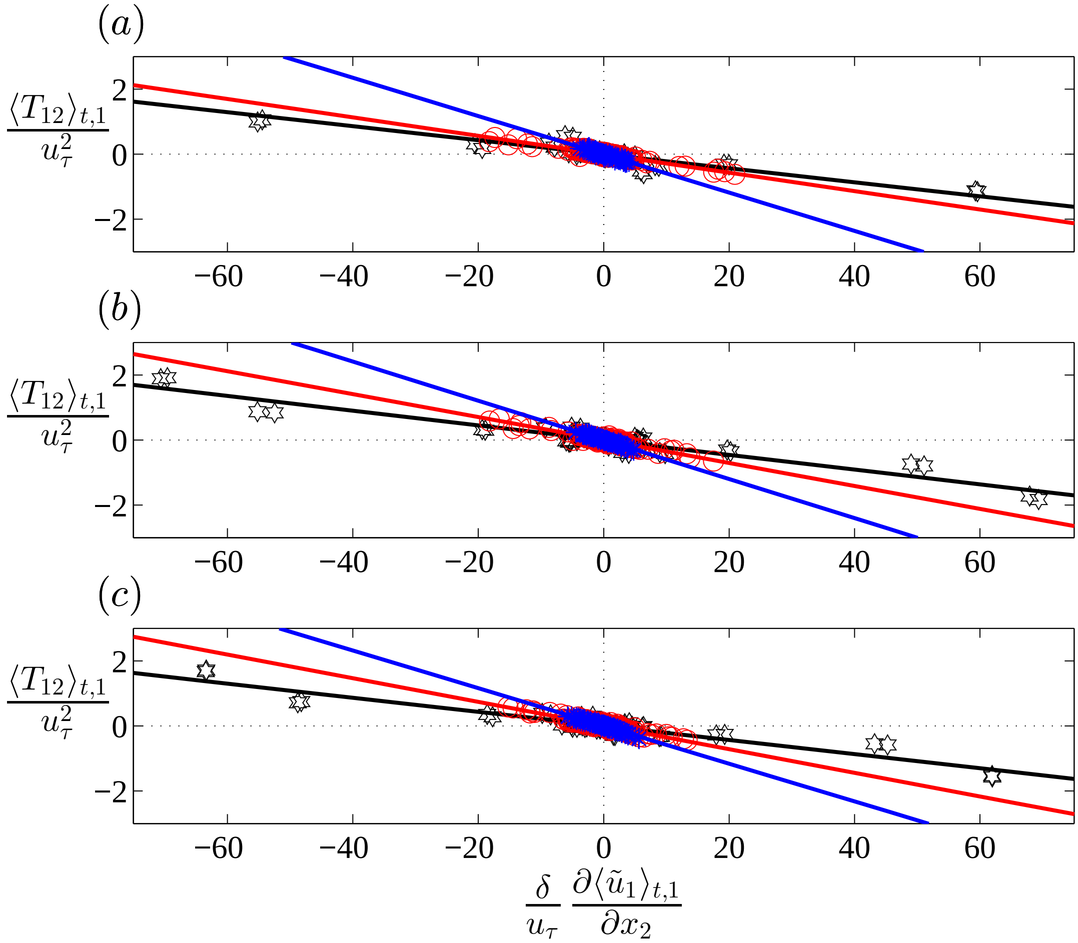

Figure 3.26: Transverse shear stress plotted vs. streamwise velocity gradient with least squared linear fits applied. Data points and lines taken at $x_3/\delta \approx 0.001$ (black), $x_3/\delta \approx 0.02$ (red) and $x_3/\delta \approx 0.04$ (blue) from cases D1 (figure a), D2 (figure b) and D3 (figure c).

value of a velocity gradient, which would be $\langle\partial\tilde{u}_1\rangle_{t,1}/\partial x_2$ in this instance. Thus Equation 3.7 becomes

$$\nu_T = l^2\frac{\partial\langle\tilde{u}_1\rangle_{t,1}}{\partial x_2}. \tag{3.8}$$

Recall form Figure 3.11 that $\partial\langle\tilde{u}_1\rangle_{t,1}/\partial x_2$ profiles all reach maximum absolute values at x_2 locations directly over the roughness transitions. Because of this, mixing length values can now be obtained by rearranging Equation 3.8 and taking the maximum

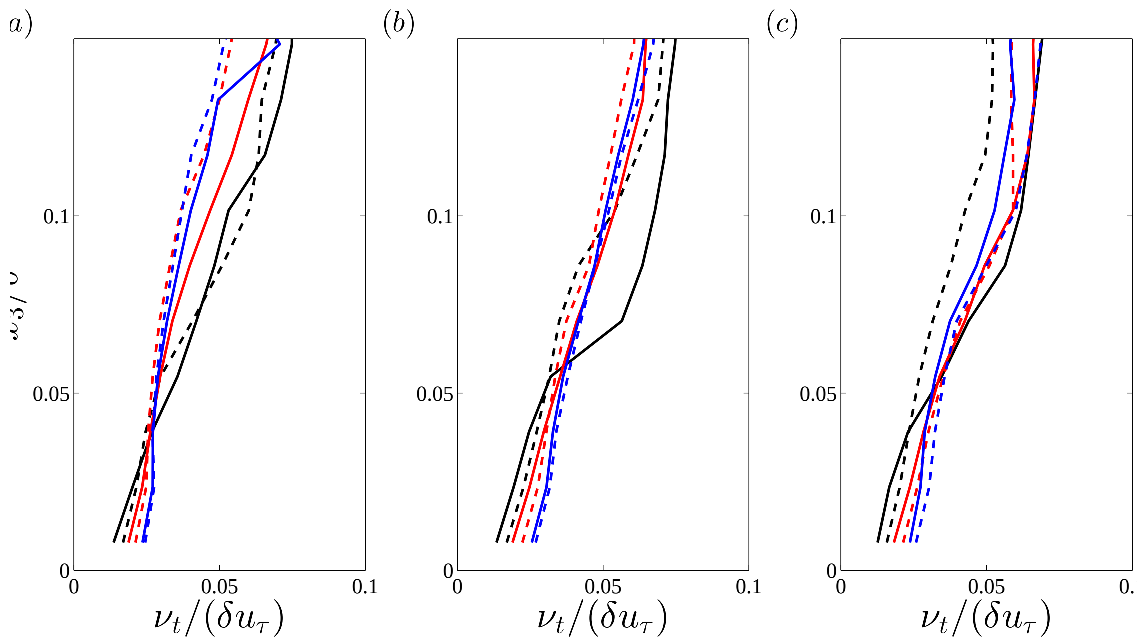

Figure 3.27: Vertical profiles of turbulent eddy viscosity, $\nu_T/(\delta u_\tau)$. For cases A-F1 (figure a), A-F2 (figure b) and A-F3 (figure c).

spanwise value of $|\partial\langle\tilde{u}_1\rangle_{t,1}/\partial x_2|$ as shown in Equation 3.9:

$$l = \sqrt{\frac{\nu_T}{\max(|\partial\langle\tilde{u}_1\rangle_{1,t}/\partial x_2|)}}. \tag{3.9}$$

From Equation 3.9, the transverse turbulent mixing length is found at every x_3/δ location and profiles of l/δ are provided in Figure 3.28. The analytical mixing length associated with the boundary layer, $l = \kappa x_3$, is also provided for reference.

Near the surface, mixing length values are approximately logarithmic and decrease monotonically with increasing λ and decreasing L_s/δ. But, these trends become less consistent above approximately 0.15δ. Recall from Figure 3.11 that maximum values of $|\partial\langle\tilde{u}_1\rangle_{t,1}/\partial x_2|$ are found over the roughness transitions near the surface, but often shift towards the center of the domain at some height, due to the formation of low momentum pathways above z_{0L} roughness. Therefore, l/δ values ultimately have no significance above approximately $x_3/\delta = 0.15$ anyway, because for most simulations, $\max(|\partial\langle\tilde{u}_1\rangle_{t,1}/\partial x_2|)$ shifts away from the roughness transitions around this

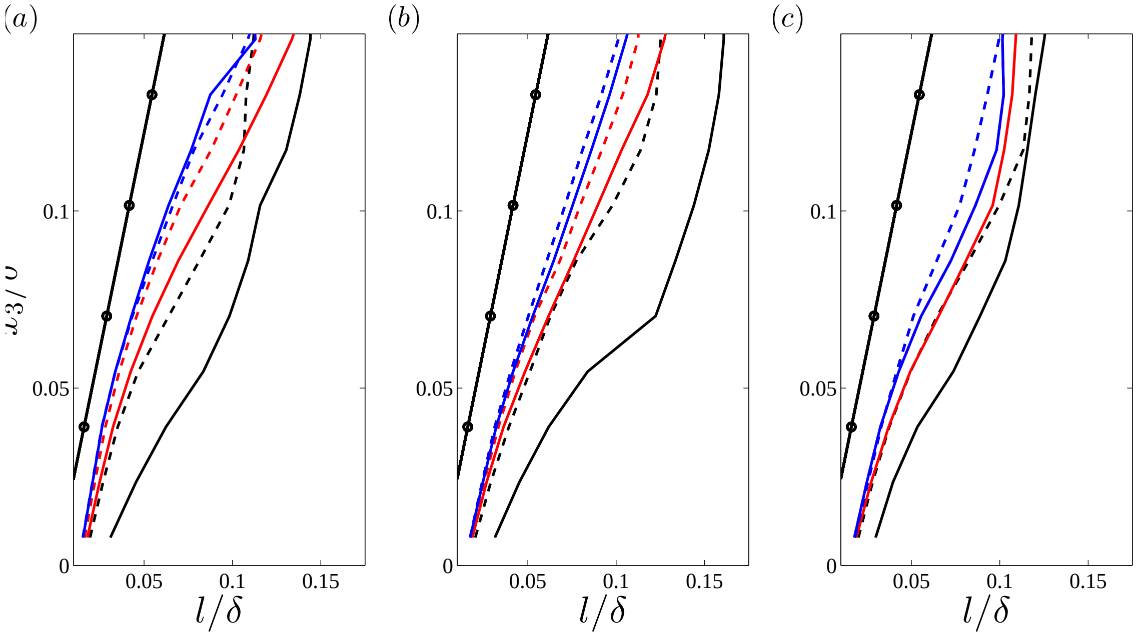

Figure 3.28: Vertical profiles of transverse mixing length from cases A-F1 (figure a), A-F2 (figure b) and A-F3 (figure c). Thick black line with circles indicates analytical boundary layer mixing length.

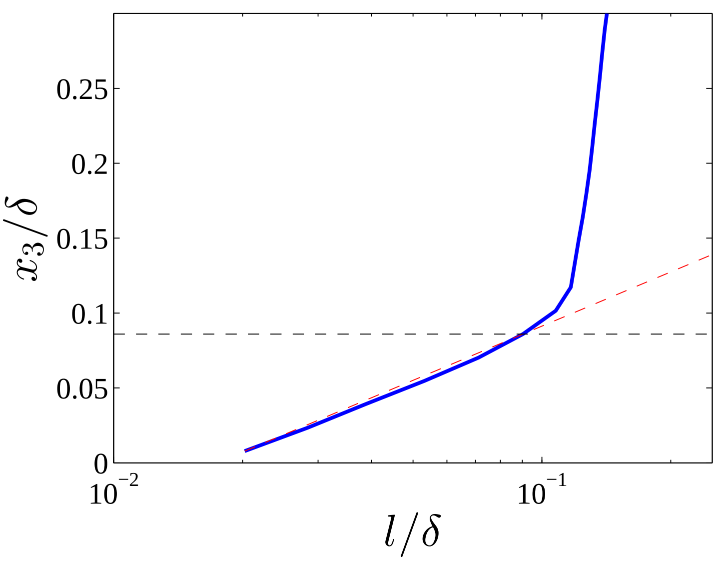

Figure 3.29: Mixing length profile from case B3 (solid blue line) with logarithmic fit (dashed red line) applied to values below the shifting elevation of maximum transverse gradient (dashed black line).

altitude, mixing remains substantially weaker than that of typical boundary layer mixing in the vertical direction. just as the case shown in Figure 3.12 does. Figure 3.29 provides an example of how mixing length profiles deviate from their nearly logarithmic form for all elevations above some shifting height of $\max(|\partial\langle\tilde{u}_1\rangle_{t,1}/\partial x_2|)$. This proves that only mixing length values taken near the surface are valid. But as with profiles of ν_T, this is acceptable since turbulent eddies associated with the most intense transverse momentum exchange are located close to the surface. The trends shown in Figure 3.28 reveal that smaller mixing lengths are associated with more vigorous mixings, since l values monotonically decrease and increase with growing λ and L_s/δ, respectively. Figure 3.28 also shows smaller length scales for eddies in the $\{x_1, x_3\}$ plane, which are associated with the turbulent boundary layer, than those associated with transverse mixing in the $\{x_1, x_2\}$ plane. It follows then, that in all cases considered, transverse mixing remains substantially weaker than that of typical boundary layer mixing in the vertical direction.

CHAPTER FOUR

Secondary Simulation Results

In Chapter 3, a highly specific, idealized, roughness configuration is shown to produce a particular set of flow features. However, this should not be interpreted to mean that only this precise configuration is capable of producing such results. Several alterations to this configuration have also been considered, which seem to produce similar effects to those discussed in Chapter 3. Several examples of this are discussed in this chapter and comparisons are made with respect to cases in Table 3.1. The purpose of this chapter is not to restate the statistics shown for the cases in Table 3.1, but rather to investigate how they are effected by certain, modifications to the surfaces considered in Chapter 3.

Table 4.1: Summary of Lower Resolution Cases

Case	λ	$\approx L_s/\delta$
a1, a2, a3	2	0.2, 0.6, 1.0
b1, b2, b3	10	0.2, 0.6, 1.0
c1, c2, c3	25	0.2, 0.6, 1.0
d1, d2, d3	100	0.2, 0.6, 1.0
e1, e2, e3	500	0.2, 0.6, 1.0
f1, f2, f3	900	0.2, 0.6, 1.0

The LES described in this chapter were run with the same code described in Chapter 2. However, a coarser mesh of $Nx_1 = Nx_2 = Nx_3 = 64$ was necessary in order to allow for frequent adjustments to be made in the domains and parameters without unacceptable computational expense. In order to confirm consistency between results acquired from this relatively low resolution and those in the preceding

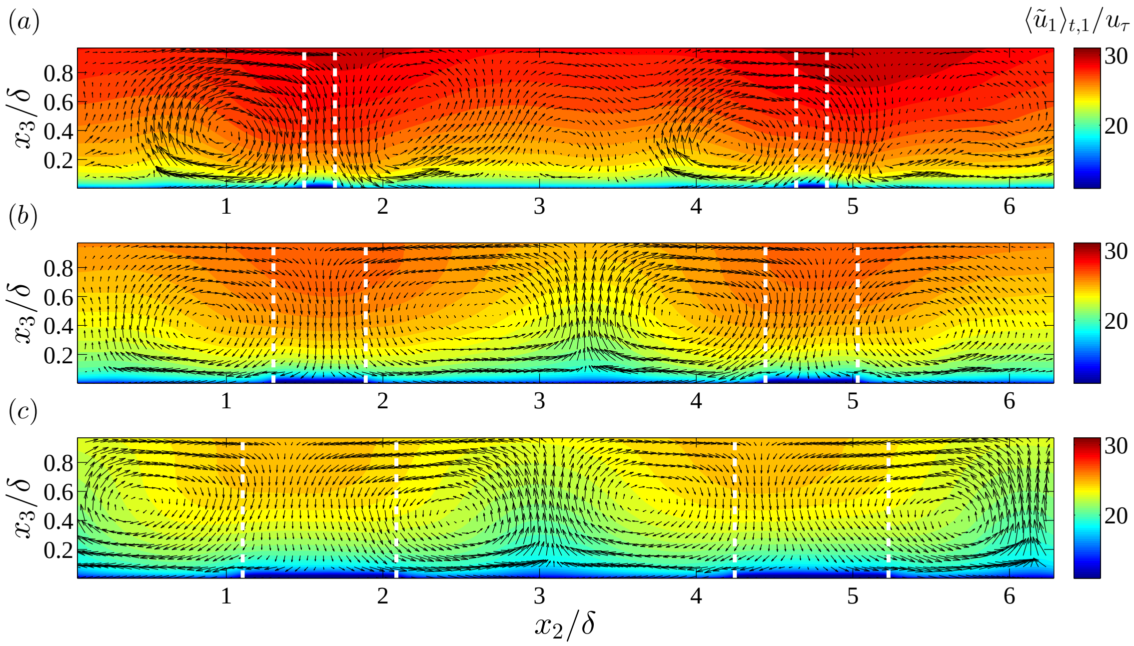

Figure 4.1: Black vectors of secondary flow components, $\{\langle\tilde{u}_2\rangle_{t,1}/u_\tau, \langle\tilde{u}_3\rangle_{t,1}/u_\tau\}$, superimposed over contours of streamwise velocity for cases d1-3. White dotted lines indicate x_2/δ locations of transverse variations in surface roughness.

chapter, all cases in Table 3.1 have been replicated at the coarser resolution. Figure 4.1 shows velocity contours with superimposed secondary flow vectors similar to those shown previously in Figures 3.1-3.6. The cases used in Figure 4.1 are analogous to cases D1-3 and demonstrate the same counter-rotating vortex and LMP-HMP patterns seen in the high resolution cases. This clearly demonstrates that low resolution results are, at least, qualitatively equivalent those at higher resolutions.

Figure 4.2 compares profiles of surface stress, transverse velocity gradient and transverse Reynolds stress taken at locations near the surface, for both the high and low resolution cases. This figure is quite useful for demonstrating similarity between high and low resolution cases because, as has been shown, heterogeneities in these particular statistics are responsible for driving all flow features described in Chapter 3. From these profiles, it can be seen that statistics taken with the coarse resolution are quantitatively similar, though of course, not identical, to high resolution statistics.

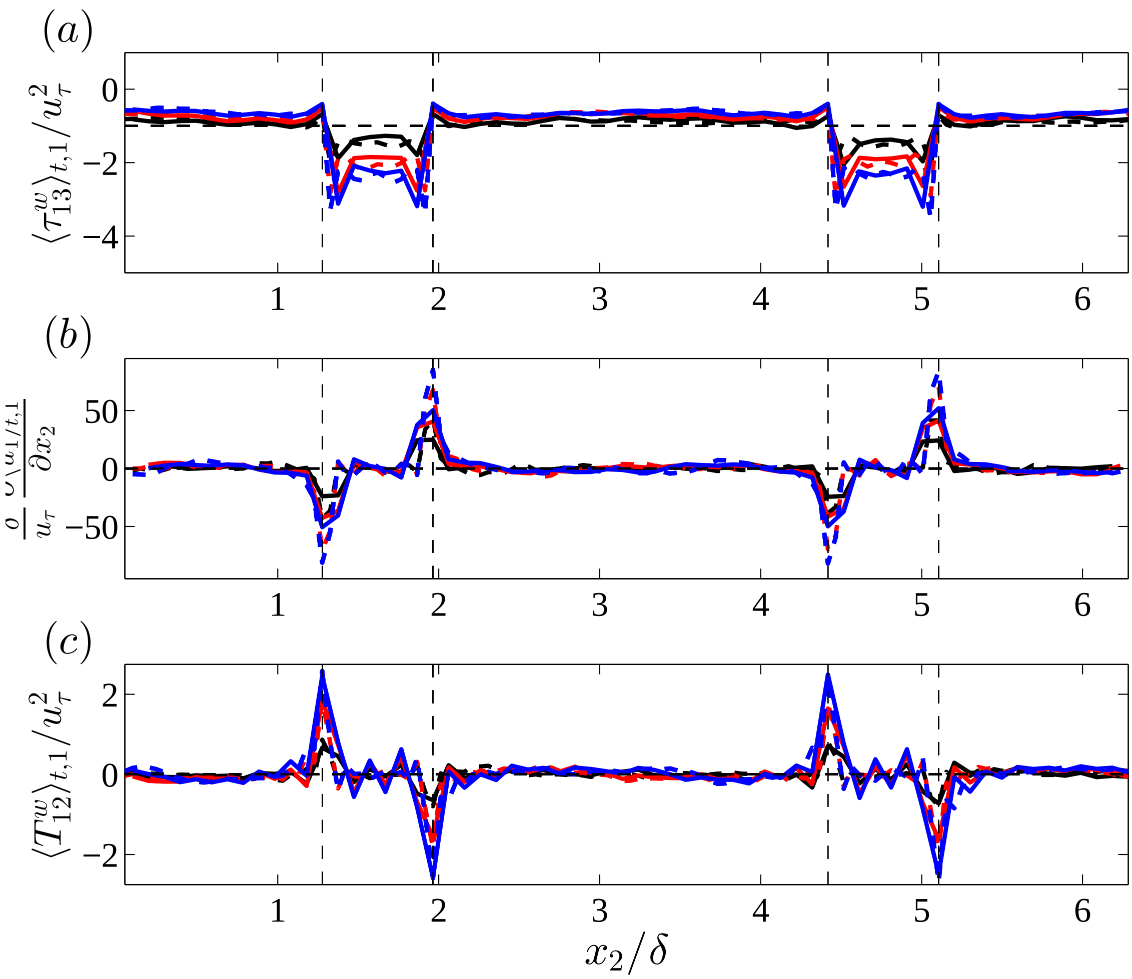

Figure 4.2: Streamwise averaged profiles of: wallstress (figure a), transverse velocity gradient (figure b) and transverse shear stress at $x_3 \approx 0.01\delta$ (figure c) for cases b2 (black line), B2 (dashed black line), d2 (red line), D2 (dashed red line), f2 (blue line) and F2 (dashed blue line).

As anticipated, extreme values of $\langle\tau_{13}^w\rangle_{t,1}/u_\tau^2$, $\frac{\delta}{u_\tau}\partial\langle\tilde{u}_1\rangle_{t,1}/\partial x_2$ and $\langle T_{12}^w\rangle_{t,1}/u_\tau^2$ occur near the transitions and monotonically increase and decrease in magnitude with growing values of λ and L_s/δ, respectively. There is close quantitative agreement observed between high and low resolution profiles of $\langle\tau_{13}^w\rangle_{t,1}/u_\tau^2$ and $\langle T_{12}^w\rangle_{t,1}/u_\tau^2$. However, in general maximum values of $\frac{\delta}{u_\tau}\partial\langle\tilde{u}_1\rangle_{t,1}/\partial x_2$ profiles taken from Table 4.1 cases, are lower than corresponding cases from Table 3.1. This is the simply the result of central differencing, used to calculate profiles of $\frac{\delta}{u_\tau}\partial\langle\tilde{u}_1\rangle_{t,1}/\partial x_2$ that causes them to be particularly affected by changes in mesh resolution. This is certainly not to say that the same driving mechanisms observed previously, are no longer captured at courser resolution, but rather that profiles of transverse gradients appear smoother than those from cases with finer meshes. This is only because averaging must be performed over larger transverse surface areas for low resolution cases, in order to obtain data at consistent locations with respect to all other statistics considered in this thesis.

Because nodes with discontinuous values of z_0 are separated by spanwise grid-spacing, Δ_2, increasing cell size causes nodes, adjacent to the roughness transitions, to become farther removed from the transition locations where shearing and mixing effects are generated. Fortunately, it is anticipated that the shearing and resulting secondary flows, caused by transverse roughness transitions would, if anything, be understated rather than exaggerated as a result of lower resolution. Therefore based on results shown in Figures 4.1 and 4.2, no reason is found to assume that the presence of mixing and secondary flows, shown in cases at lower resolution, are physically unrealistic.

4.1 Enhanced Strip Width

Up to this point there has been no consideration given to surfaces where the total surface area of $z_{0,H}$ is equal to greater than the total surface area of $z_{0,L}$, that is to say, cases for which $L_s/\delta \geq \pi/2$. At such large values of L_s/δ, surface locations with high roughness would more accurately be described as separate regions, as opposed to merely strips. Table 4.2 shows cases with L_s/δ values of: $\pi/2$, ≈ 2.2 and ≈ 2.8 at the same λ values as in Table 3.1. Note that, because cases in Table 4.2 have high L_s/δ values, the effects of λ are weaker than those of L_s/δ for Table 4.2 cases.

Cases run with $L_s/\delta = \pi/2$, such as case D_w1, shown in Figure 4.3 (a), still show consistent formation of high and low momentum pathways, as well as symmetric,

Table 4.2: Summary of Cases with Widened Strip Width

Case	λ	$\approx L_s/\delta$
A_w1, A_w2, A_w3	2	$\pi/2, \approx 2.2, \approx 2.8$
B_w1, B_w2, B_w3	10	$\pi/2, \approx 2.2, \approx 2.8$
C_w1, C_w2, C_w3	25	$\pi/2, \approx 2.2, \approx 2.8$
D_w1, D_w2, D_w3	100	$\pi/2, \approx 2.2, \approx 2.8$
E_w1, E_w2, E_w3	500	$\pi/2, \approx 2.2, \approx 2.8$
F_w1, F_w2, F_w3	900	$\pi/2, \approx 2.2, \approx 2.8$

well-structured counter-rotating vortices. However, for cases where L_s/δ is increased to $\approx$ 2.2 as in Figure 4.3 (b), both the LMP-HMP patterns and secondary flow structures tend to becomes somewhat less organized. Cases with $L_s/\delta \approx 2.8$, such as Figure 4.3 (c), typically have significant asymmetry associated with both mean and secondary flows. These results demonstrate that increasing L_s/δ above $\approx \pi/2$, causes increasingly inconsistent primary and secondary flow structures. Also for cases with large L_s/δ values such as ≈ 2.8, the total surface drag is increased to the point where transverse gradients are not large enough to produce consistent flow features with those seen in Chapter 3. Figure 4.4, shows how $\langle \tau_{13}^w \rangle_{t,1}/u_\tau^2$, $\frac{\delta}{u_\tau}\partial\langle\tilde{u}_1\rangle_{t,1}/\partial x_2$, and T_{12}^w/u_τ^2 decrease monotonically as L_s/δ increases. These cases indicate that while the addition of parallel, high roughness strips to surfaces composed of relatively low roughness is capable of causing significant effects on the flow field, adding strips of relatively low roughness to surfaces with relatively high roughness has substantially less impact on the flow.

It is theorized that cases with equal surface areas of $z_{0,L}$ and $z_{0,H}$ may in fact, be optimal for reducing asymmetry in the boundary layer scale, counter-rotating vortices. For such cases, $z_{0,L}$ regions are wide enough to create flow gradients, capable of

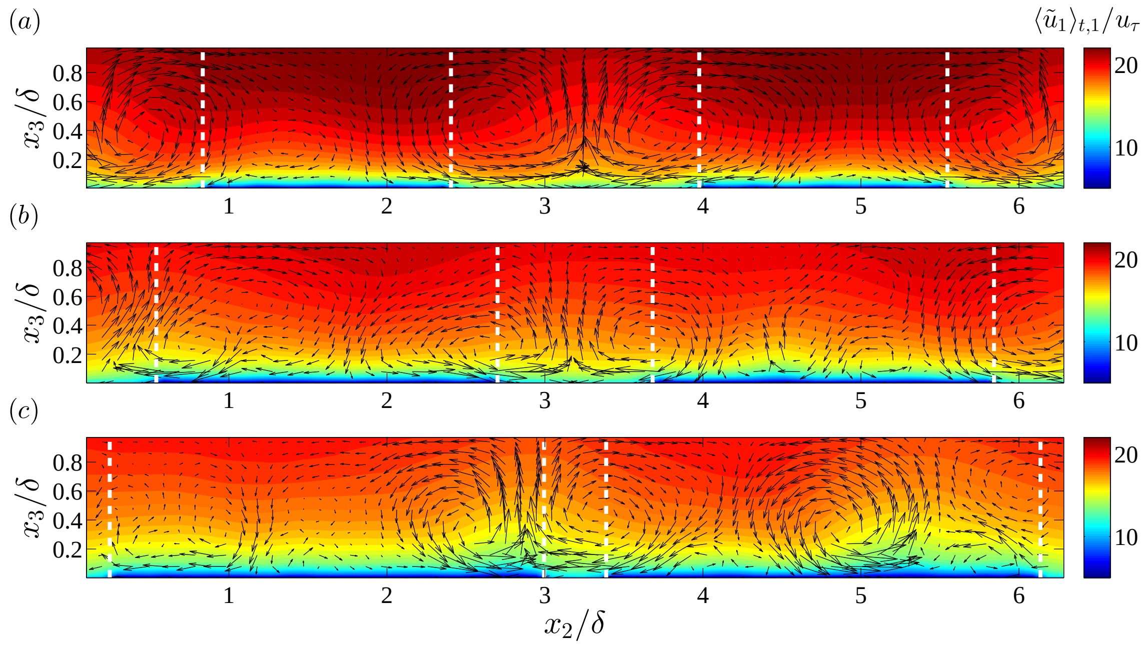

Figure 4.3: Black vectors of secondary flow components, $\{\langle \tilde{u}_2 \rangle_{t,1}/u_\tau, \langle \tilde{u}_3 \rangle_{t,1}/u_\tau\}$, superimposed over contours of streamwise velocity for cases D_w1, D_w2 and D_w3.

driving secondary flows, yet narrow enough to constrain the LMPs and prevent significant drifting of counter-rotating vortices. Figure 4.5 shows cases B_w1, D_w1 and E_w1, which again show only slight amounts of asymmetry. Precise prediction of counter-rotating vortex locations could be quite useful in, for example, applications which desire enhancement of heat transfer at a specific location. However, obtaining quantitative confirmation this hypothesis would require a tremendous number of additional simulations, due to the inherent randomness associated with the high Reynolds number, turbulent flows under consideration and has not currently been undertaken.

4.2 Linearly Sloped Roughness

In order to explore the general effects of transverse roughness transitions, all simulations to this point have been assigned constant, uniform roughness lengths for high and low roughness regions. However, this approximation is not physically realistic for most examples of actual roughness because, as mentioned near the beginning

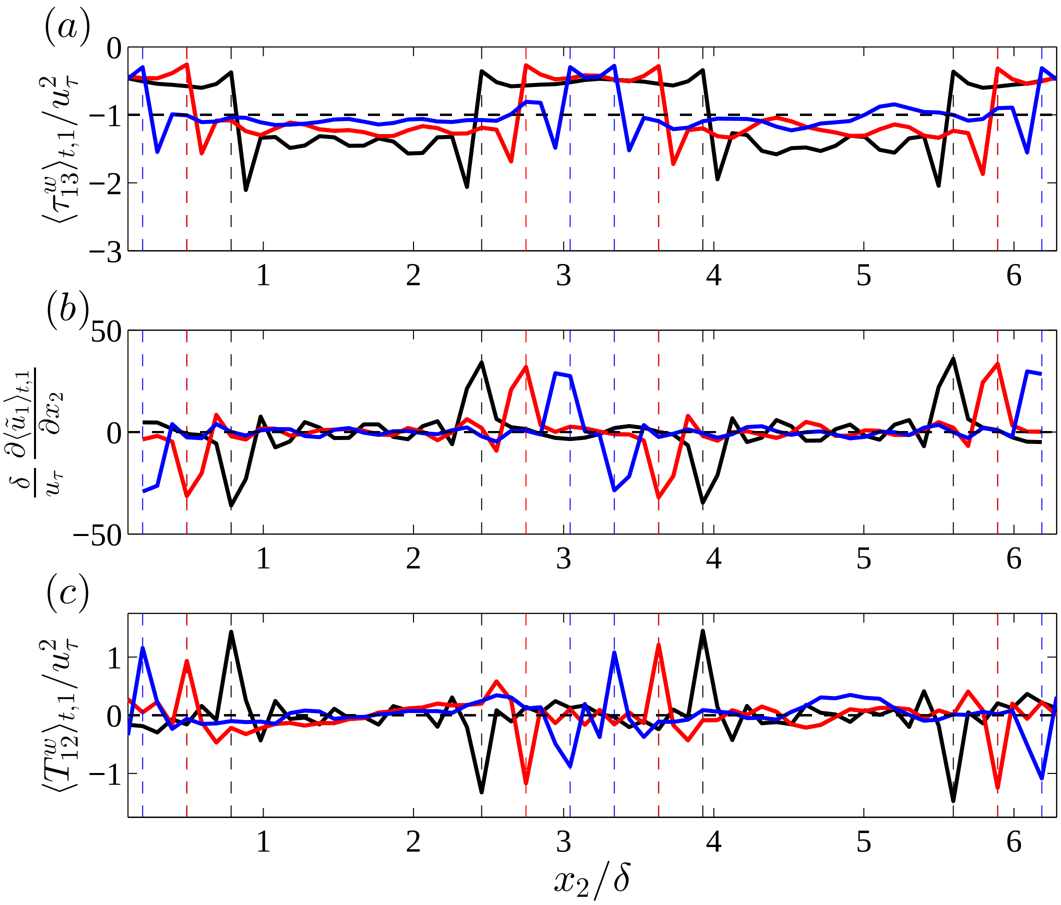

Figure 4.4: Streamwise averaged profiles of: wallstress (figure a), transverse velocity gradient (figure b) and transverse shear stress at $x_3 \approx 0.01\delta$ (figure c) for cases D_w1-3.

of this thesis, truly homogeneous roughness is rarely encountered in most engineering and scientific applications. Therefore, it is worthwhile to consider the somewhat more physically realistic scenario, of cases with non-uniform, spanwise values of $z_{0,H}$ roughness. In particular, it is of interest to determine whether the characteristics of Table 3.1 flows may be produced by smoother increases in surface roughness, instead of large step-changes. To this end, surfaces with linearly sloped $z_{0,H}$ values are considered and summarized in Table 4.3.

For all cases listed in Table 4.3, $z_{0,H}$ values are set to $1.0/\delta$ at $Lx_2/4$ and $3Lx_2/4$, and decreased linearly from these points to the edges of "elevated roughness"

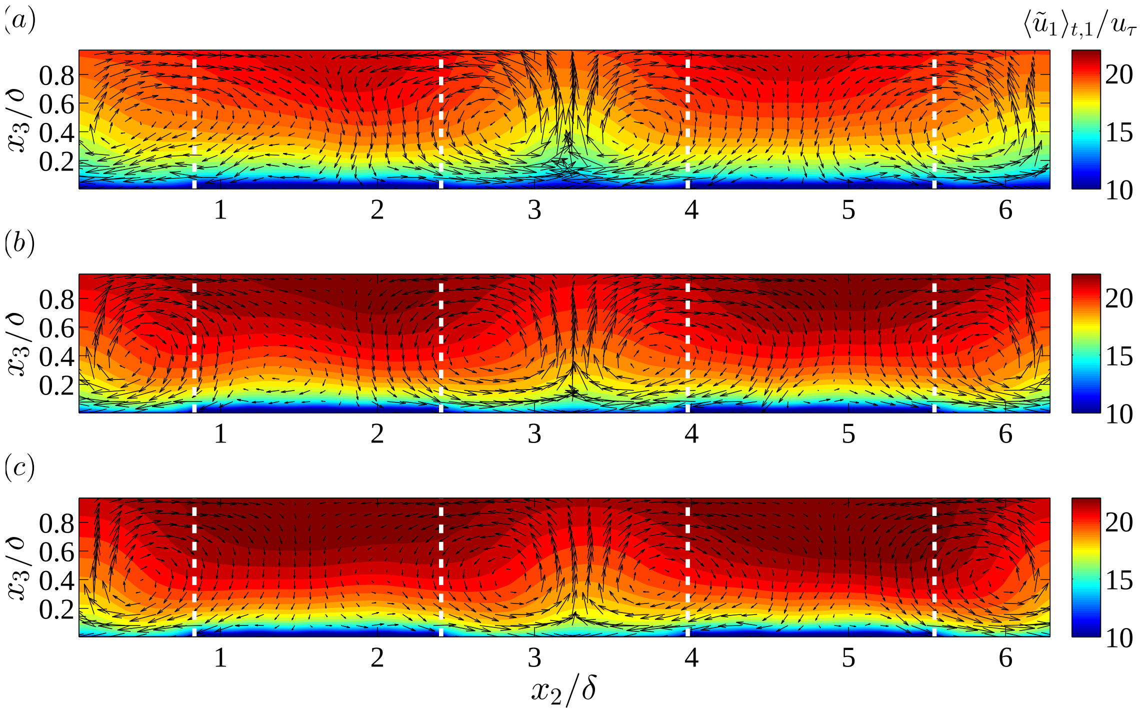

Figure 4.5: Black vectors of secondary flow components, $\{\langle \tilde{u}_2 \rangle_{t,1}/u_\tau, \langle \tilde{u}_3 \rangle_{t,1}/u_\tau\}$, superimposed over contours of streamwise velocity for cases B_w1, D_w1 and E_w1.

regions. The remaining surface area is assigned uniform roughness lengths of $z_0 = z_{0,L}$ as before. In Table 4.3, L_s refers to the transverse width of the elevated roughness regions and λ refers to the ratio of maximum to minimum roughness length values, $\lambda = z_{0,\max}/z_{0,\min}$. Figure 4.6 images demonstrate the same general features as cases listed in Table 4.1, with respect to secondary flow and LMP-HMP locations. Note that Figure 4.6 (c) shows more consistent formation of counter-rotating vortices and HMPs than does Figure 4.3 (c), despite having larger regions of increased roughness. This is partially due to lower total drag imposed on the flow by the linearly sloped roughness and partially due to the fact that mixing is created across the entire elevated roughness regions, as opposed to only at isolated roughness transitions.

Figure 4.7 compares the effects of L_s/δ on cases with λ values of 100. This figure shows that the most negative values of $\langle \tau^w_{13} \rangle_{t,1}/u_\tau^2$ are located in the centers

Table 4.3: Summary of Linearly Sloped Roughness Cases

Case	λ	$\approx L_s/\delta$
A_L1, A_L2, A_L3	2	1.0, 2.0, 3.0
B_L1, B_L2, B_L3	10	1.0, 2.0, 3.0
C_L1, C_L2, C_L3	25	1.0, 2.0, 3.0
D_L1, D_L2, D_L3	100	1.0, 2.0, 3.0
E_L1, E_L2, E_L3	500	1.0, 2.0, 3.0
F_L1, F_L2, F_L3	900	1.0, 2.0, 3.0

of the elevated roughness regions, where roughness length is highest. However, the largest gradients in $\langle \tau_{13}^w \rangle_{t,1}/u_\tau^2$ are still observed immediately beyond the edge of the elevated roughness regions, just as they were for uniform $z_{0,H}$ cases. Note that in Figure 4.7, changes in surface roughness at the edges of the sloped roughness strips are no greater than those at any other x_2 location along the elevated roughness regions. Therefore, the reason for these large changes in $\langle \tau_{13}^w \rangle_{t,1}/u_\tau^2$, is that near the surface, spanwise locations with greatest streamwise momentum are still located over $z_{0,L}$ roughness. Therefore locations with greatest transverse gradient in $\langle \tau_{13}^w \rangle_{t,1}/u_\tau^2$ are located at the edges of these $z_{0,L}$ regions due, to the influence of $\tilde{u}_1$ on τ_{13}^w described by Equation 2.12.

Based on the form of these $\langle \tau_{13}^w \rangle_{t,1}/u_\tau^2$ profiles, the trends observed in profiles of $\frac{\delta}{u_\tau}\partial\langle \tilde{u}_1 \rangle_{t,1}/\partial x_2$ and $\langle T_{12}^w \rangle_{t,1}/u_\tau^2$ are not surprising. Because $\tilde{u}_1$ and τ_{13}^w are interdependent, $\partial\langle \tilde{u}_1 \rangle_{t,1}/\partial x_2$ reaches its most extreme values at the same x_2 locations where $\langle \tau_{13}^w \rangle_{t,1}/u_\tau^2$ profiles experience the sharpest changes. The maximum absolute values in $\langle T_{12}^w \rangle_{t,1}/u_\tau^2$ are also located at the edges of the sloped roughness, but in these cases, a greater amount of horizontal shearing and mixing exists throughout the entire elevated roughness regions. Greater values of L_s/δ result in smoother profiles of $\langle \tau_{13}^w \rangle_{t,1}/u_\tau^2$ and as a result, smoother profiles of $\frac{\delta}{u_\tau}\partial\langle \tilde{u}_1 \rangle_{t,1}/\partial x_2$ and $\langle T_{12}^w \rangle_{t,1}/u_\tau^2$ also.

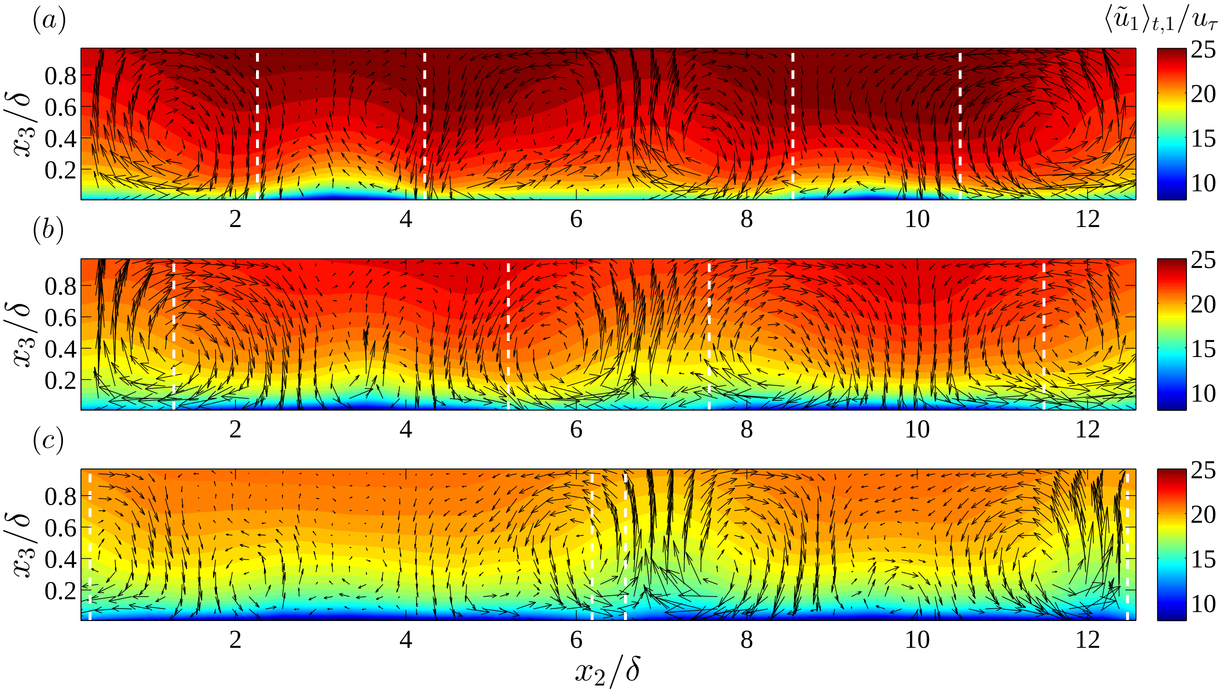

Figure 4.6: Black vectors of secondary flow components, $\{\langle \tilde{u}_2 \rangle_{t,1}/u_\tau, \langle \tilde{u}_3 \rangle_{t,1}/u_\tau\}$, superimposed over contours of streamwise velocity for cases B_L1, D_L1 and E_L1.

Thus, unlike Table 4.3 cases, shearing and mixing are not exclusively created at the roughness transitions, but throughout the $z_{0,H}$ roughness regions. This leads to more consistent secondary flow than for analogous cases with uniform roughness.

4.3 Sinusoidal Roughness

It has been shown that the flow characteristics produced by Table 3.1 cases, may be reproduced more consistently at large values of L_s/δ, if $z_{0,H}$ roughness regions consist of continuous changes in roughness length rather than uniform values. Here consideration is given to surfaces with no uniform roughness at all, by using a sine wave pattern for roughness length, along the entire spanwise dimension. A sinusoidal distribution of roughness seems well suited for producing the secondary flow effects of interest here. It offers more distinction between high and low roughness regions than a linear roughness distribution, but still creates continuous gradients in surface stress along the entire x_2 dimension. A summary of these cases is given in Table 4.4, where

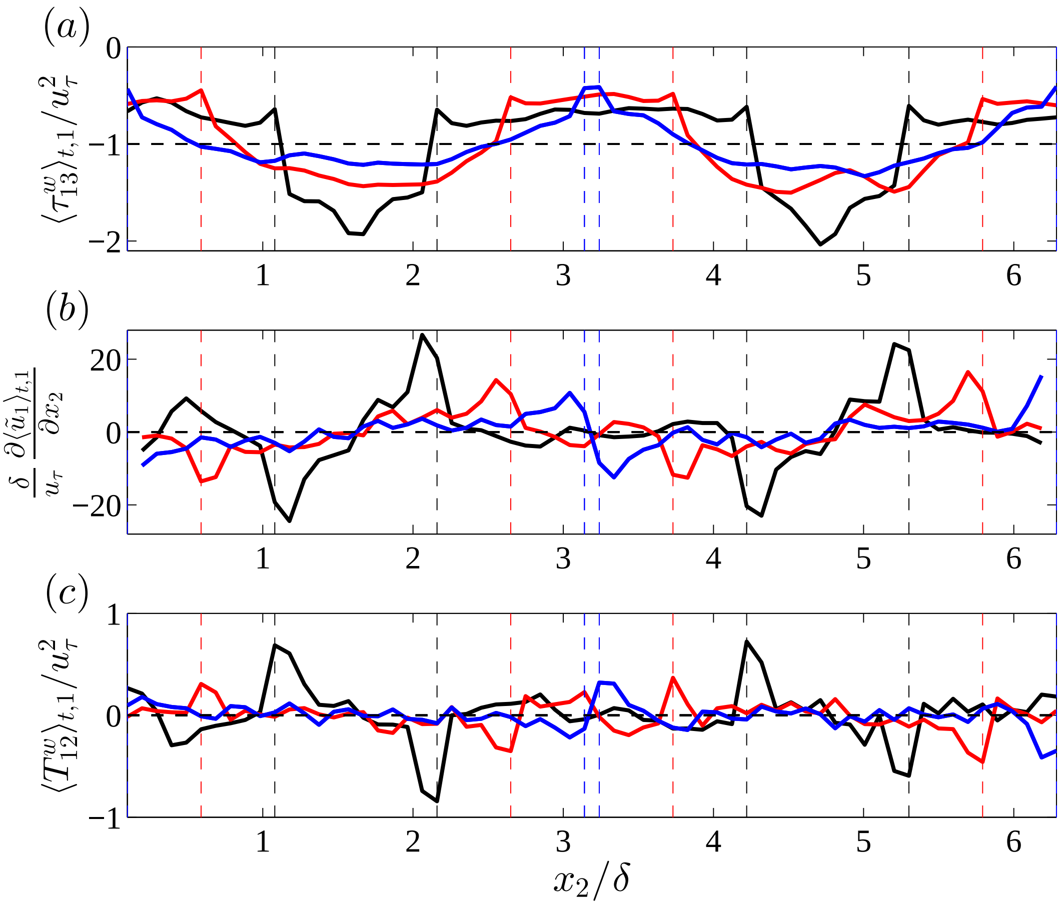

Figure 4.7: Streamwise averaged profiles of: surface stress (figure a), transverse velocity gradient (figure b) and transverse shear stress at $x_3 \approx 0.01\delta$ (figure c) for cases D_L1 (black), D_L2 (red) and D_L3 (blue).

as in Table 4.3, $\lambda = z_{0,\max}/z_{0,\min}$. Local roughness values are assigned according to:

$$z_0(x_2) = \left(\sin\left(\left(2\pi \frac{x_2}{Lx_2} \right) 2 - \pi/2 \right) \left(0.5 - \frac{z_{0,L}\delta}{2} \right) + 0.5 + \frac{z_{0,L}\delta}{2} \right) \right) z_{0,H}, \qquad (4.1)$$

so that z_0 values range from $z_{0,H}$ at $L_s = Lx_2/(4\delta)$ and $L_s = 3Lx_2/(4\delta)$ to $z_{0,L}$ at $L_s = 0$ and $L_s = Lx_2/(2\delta)$. Figure 4.8 shows velocity contours and secondary flow vectors for cases S1, S2 and S4 from Table 4.4. Dashed white lines, which correspond with values of $z_0\delta/10$ are are superimposed onto Figure 4.8 for reference. Figure 4.8 shows that Table 4.4 surfaces are also able to produce consistent mean and secondary flow structures with those of cases in Table 3.1.

Table 4.4: Summary Sinusoidal Roughness Cases

Case	λ
S1	2
S2	10
S3,	25
S4	100
S5	500
S6	900

These results are similar to what was seen in cases with linearly sloped roughness lengths. But it should be noted, that in Table 4.4 cases, secondary flow is in no way effected by total surface drag, because no $z_{0,L}$ regions are present. Therefore secondary flow is generated over sinusoidal roughness length, exclusively through transverse mixing spread throughout the entire domain.

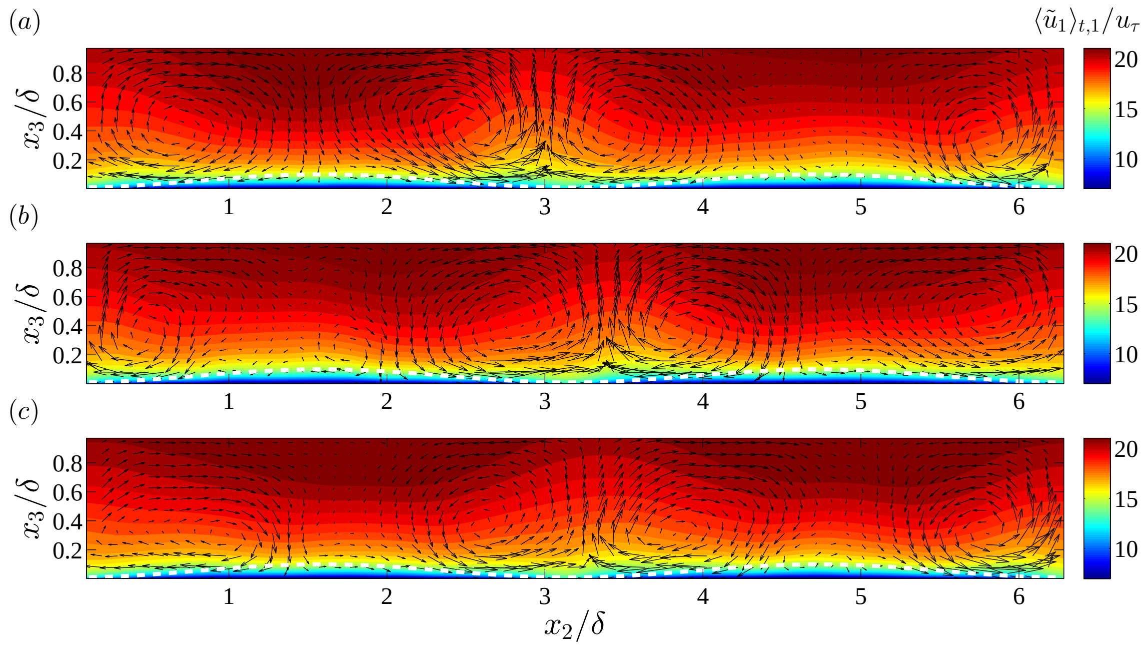

Figure 4.8: Black vectors of secondary flow components, $\{\langle \tilde{u}_2 \rangle_{t,1}/u_\tau, \langle \tilde{u}_3 \rangle_{t,1}/u_\tau\}$, superimposed over contours of streamwise velocity for cases S1, S2 and S4. White dotted lines indicate local values of surface roughness length $z_0\delta/10$.

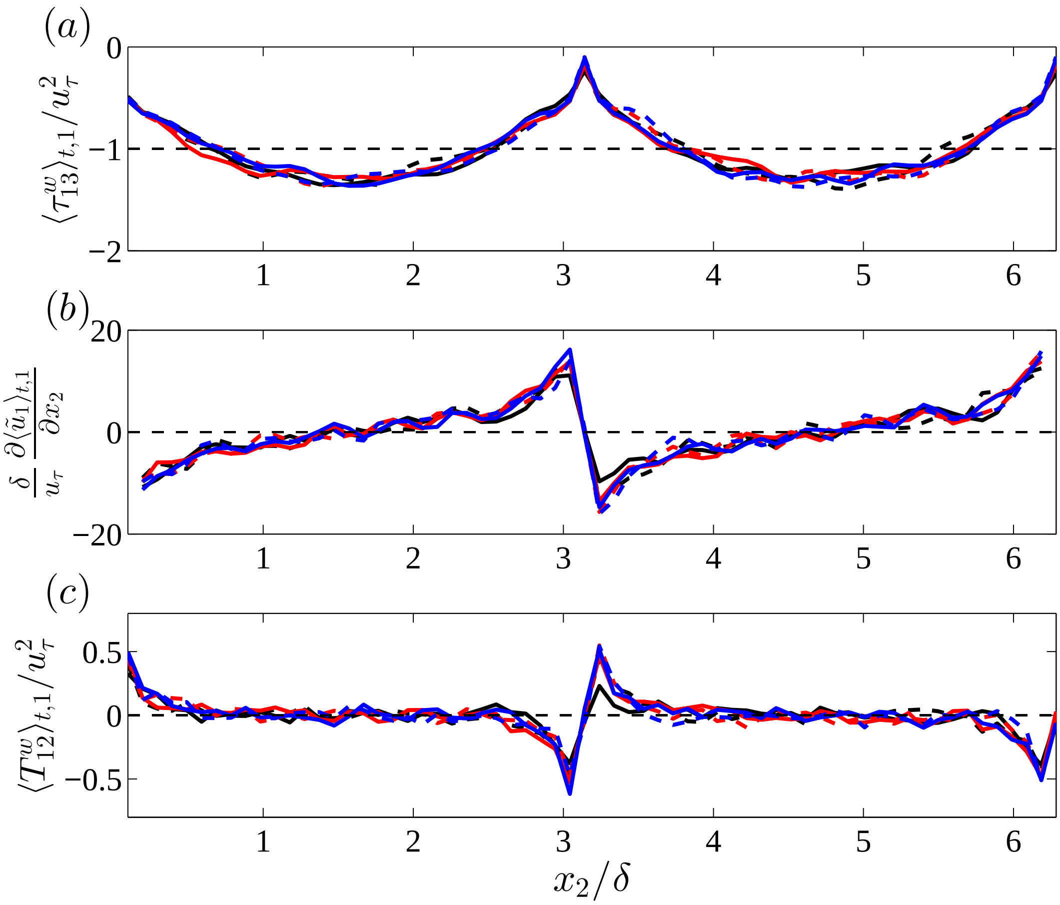

Figure 4.9: Streamwise averaged profiles of: surface stress (figure a), transverse velocity gradient (figure b) and transverse shear stress at $x_3 \approx 0.01\delta$ (figure c) for cases S2 (black line), S4 (red line) and S5 (blue line).

In Figure 4.9, profiles of surface stress, transverse velocity gradient and transverse shear stress, show that sinusoidal roughness cases show little dependence on λ. This is to be expected, because these sinusoidal roughness patterns cover the entire domain surface area and the impact of λ is dependent on the width of regions with uniform $z_{0,L}$. However, this is an important result, because it shows that subtle, but continuous gradients in roughness length, are able to produce well ordered flow features even at relatively low values of λ. This is confirmed in Figures 4.8 which shows good HMP-LMP symmetry and well ordered formation of counter-rotating vortices even for cases S1 and S2 in panels (a) and (b).

There is no single location in Figure 4.9 (a), which exhibits a dramatic increase in surface stress, as has been the case throughout results in previous sections. Instead, as with cases A_L-F_L3, transverse velocity gradient and shear stress are entirely due to subtle changes in roughness found across the entire domain surface. Absolute values of $\frac{\delta}{u_\tau}\partial\langle\tilde{u}_1\rangle_{t,1}/\partial x_2$ increase in an almost linear manner from ≈ 0 at local maxima in surface roughness, to maximum absolute values at local minima in surface roughness. This can be attributed to continuous, transverse shearing and mixing across the entire surface, which drives secondary flow at all spanwise locations and therefore causes acceleration of secondary flow, as it moves from high to low roughness. In general, the results from Table 4.4 cases suggest, that not only are large step-changes in roughness not required to produce the flow feature, discussed in Chapter 3, but it is possible that they may not even be the most effective method of doing so consistently.

4.4 Discontinuous High Roughness Strips

To ensure that mixing processes caused by transverse step-changes in roughness are fully developed, all strips of high roughness to this point have been continuous and infinite in the streamwise direction. This is of course, another idealized assumption that is not physically realistic for many practical applications. Therefore it is considered worthwhile to investigate the effects caused by high roughness strips with finite, rather than infinite lengths. The LES surfaces summarized in this section are all equivalent to those of Table 4.1, except that high roughness strips have been shortened to a streamwise length of $Lz_{0,H}$ where $0 < Lz_{0,H} < Lx_1$. A sketch of the described roughness configuration is provided in Figure 4.10 and Table 4.5 summarizes properties of the eight cases considered.

Figures 4.11 and 4.12 show streamwise velocity contours and vectors of secondary flow components, taken at $x_1 = Lz_{0,H}$, where transverse mixing effects have had greatest streamwise distance to develop. A qualitative analysis of Figures 4.11-4.12 shows that secondary flow structures become increasingly less organized as $Lz_{0,H}$ is reduced. It can be inferred from Figure 4.11-4.12 that for well-structured

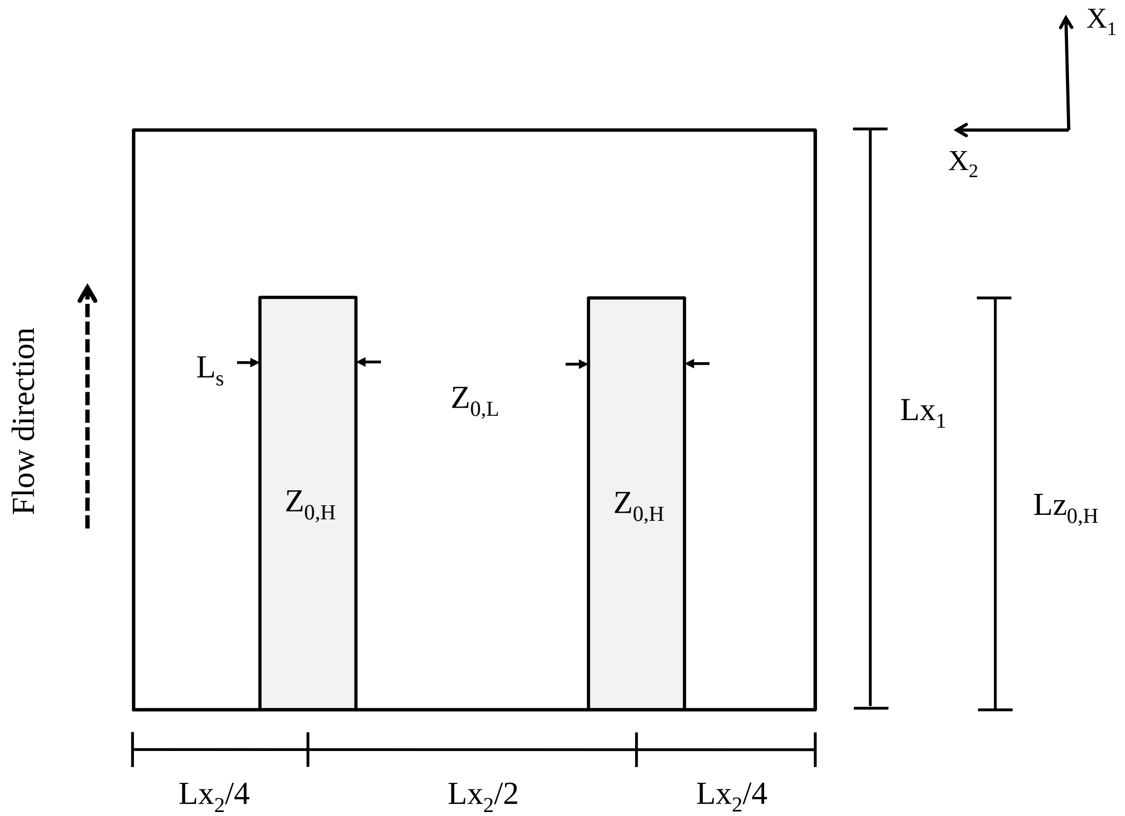

Figure 4.10: Illustration of basic surface roughness configuration used for cases in Table 4.4. Two strips of relatively high roughness length, $z_{0,H}$, are centered at $Lx_2/4$ and $3Lx_2/4$ with length $Lz_{0,H}$ and width L_s.

counter-rotating vortices and LMP-HMP patterns to form consistently, streamwise transition lengths of $Lz_{0,H} > \delta$ are typically required. Unfortunately, defining a precise $Lz_{0,H}$ value for which consistent vortex cores form, is not reasonable due to the inherent randomness of the turbulent flow considered here. Nevertheless, from Figures 4.11-4.12 alone, it can be reasonably stated that extremely long transition lengths are not necessary to produce the same flow features seen in Chapter 3.

Table 4.5: Summary of Discontinuous Strip Cases

Case	λ	L_s/δ	$Lz_{0,h}$
G1,	100	0.6	$0.875Lx_1$
G2,	100	0.6	$0.750Lx_1$
G3,	100	0.6	$0.625Lx_1$
G4,	100	0.6	$0.500Lx_1$
G5,	100	0.6	$0.375Lx_1$
G6,	100	0.6	$0.250Lx_1$
G7,	100	0.6	$0.125Lx_1$
G8,	100	0.6	$0.016Lx_1$

Figure 4.13 plots streamwise profiles of $\langle \tau_{13}^w \rangle_{t,1}/u_\tau^2$, $\frac{\delta}{u_\tau}\partial\langle \tilde{u}_1 \rangle_{t,1}/\partial x_2$ and $\langle T_{12}^w \rangle_{t,1}/u_\tau^2$, taken at $\{x_2 = Lx_2/4 - L_s/2, x_3 \approx 0.01\}$. Only cases G1, G4 and G7 are used in Figure 4.13 to enhance clarity of results, but it should be noted that the trends observed in Figure 4.13 are monotonic for all cases in Table 4.5. Vertical dotted lines are placed at $x_1 = Lz_{0,H}$ to show the endpoints of $z_{0,H}$ strips. Note that the beginning of the high roughness strips, takes place at $x_1/\delta = 0.0$ and accounts for the seemingly discontinuous changes in the profiles across the periodic boundary.

Figure 4.13 (c) shows sustained turbulent mixing continuing for over 3δ downstream of $x_1 = Lz_{0,H}$. As a result, residual downstream shear stress, in cases with small $Lz_{0,H}$ such as G7 (and even to some extent G4), does not dissipate fully by the end boundary. Therefore all profiles of case G7 experience the least dramatic drops, out of the three profiles considered, at $x_1 = 0.0$. Maximum absolute values of profiles in Figure 4.13 (a) are located at $x_1 = 0.0$. This is consistent with the observations found in literature regarding perpendicularly aligned roughness transitions [e.g. Bou-Zeid *et al.* 2004 [2]]. It can be clearly seen that the abrupt changes in $\langle \tau_{13}^w \rangle_{t,1}/u_\tau^2$ correspond exactly with changes in the slopes of $\frac{\delta}{u_\tau}\partial\langle \tilde{u}_1 \rangle_{t,1}/\partial x_2$ and $\langle T_{12}^w \rangle_{t,1}/u_\tau^2$ profiles. This simply confirms that the transverse mixing, which leads to

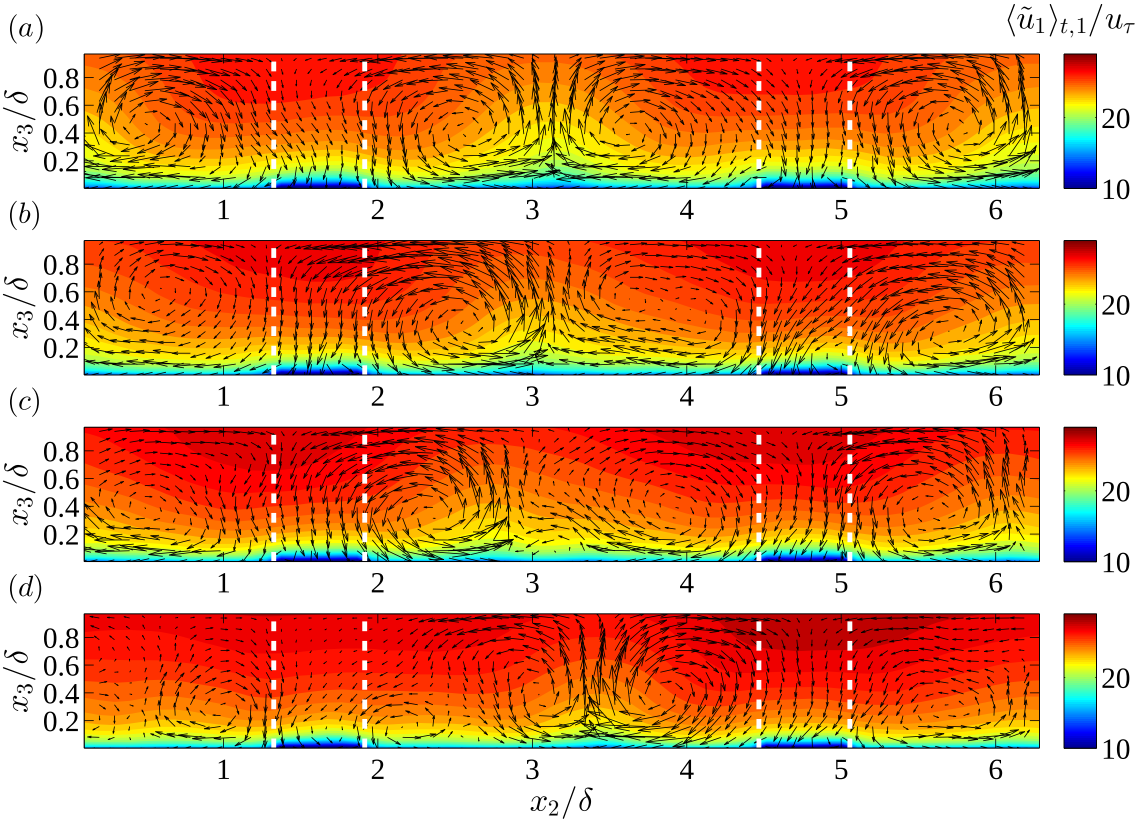

Figure 4.11: Black vectors of secondary flow components, $\{\langle\tilde{u}_2\rangle_{t,1}/u_\tau, \langle\tilde{u}_3\rangle_{t,1}/u_\tau\}$, superimposed over contours of streamwise velocity for cases G1 (figure a), G2 (figure b), G3 (figure c) and G4 (figure d). White dotted lines indicate x_2/δ locations of transverse variations in surface roughness.

momentum transport are initiated by variations in surface stress. But Figure 4.13 (b) and (c) indicate that, while shear stress develops more rapidly as transverse velocity gradient is increased, there is not a direct correlation between values of the two quantities. For example, at the streamwise location $x_1 = 0.125Lx_1$, case G3 has approximately the same value of $\frac{\delta}{u_\tau}\partial\langle\tilde{u}_1\rangle_{t,1}/\partial x_2$ as the other two cases shown in Figure 4.13 (b), yet it clearly has the least extreme value of $\langle T^w_{12}\rangle_{t,1}/u_\tau^2$ in Figure 4.13 (c). Because secondary flow structures become more consistent at $x_1 = Lz_{0,H}$ as the value of $Lz_{0,H}$ is increased (as shown by Figures 4.11-4.12), it is clear that $\langle T_{12}\rangle_{t,1}/u_\tau^2$ is more directly responsible for secondary flow generation than $\partial\langle\tilde{u}_1\rangle_{t,1}/\partial x_2$.

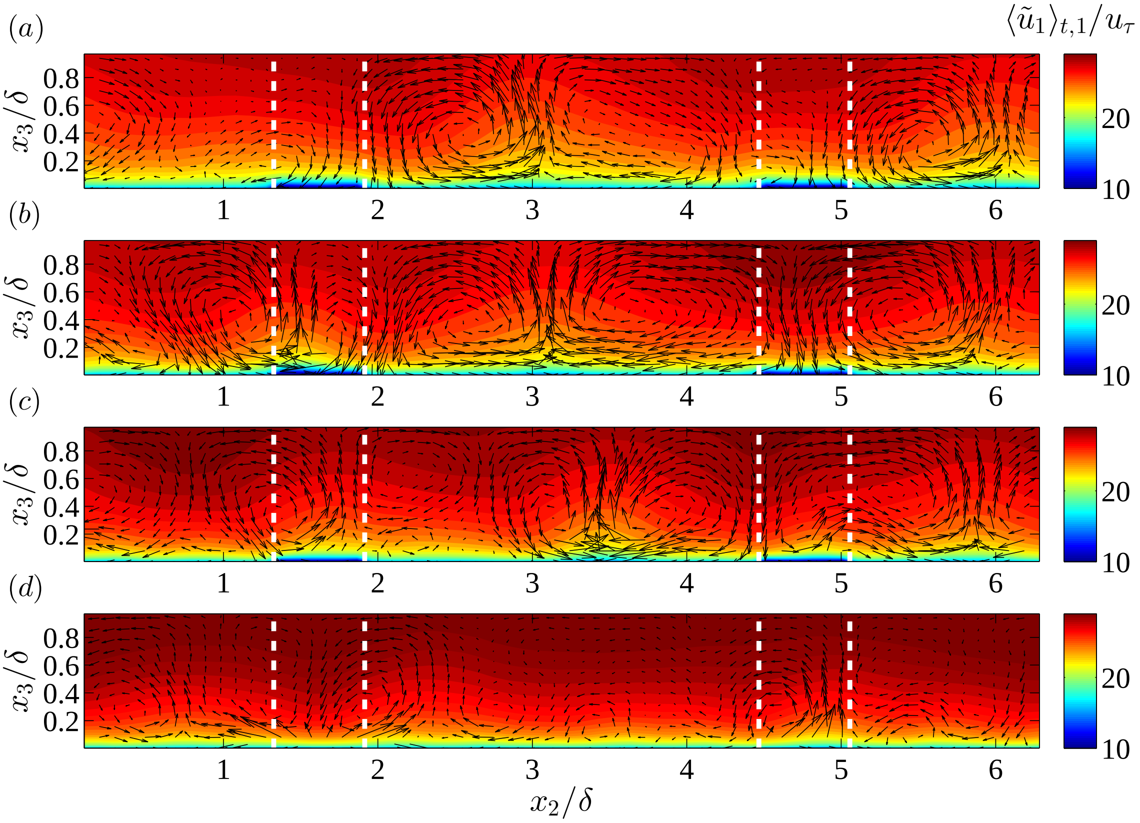

Figure 4.12: Black vectors of secondary flow components, $\{\langle\tilde{u}_2\rangle_{t,1}/u_\tau, \langle\tilde{u}_3\rangle_{t,1}/u_\tau\}$, superimposed over contours of streamwise velocity for cases G5 (figure a), G6 (figure b), G7 (figure 7) and G8 (figure8).

With the current, periodic boundary conditions, the use of smaller $Lz_{0,H}$ leads to larger streamwise gradients in all three quantities compared by Figure 4.13, at $x_1/\delta = 0.0$. This is because more shear stress is transported downstream to x_1/δ=0.0 when $Lz_{0,H}$ is increased and as Figure Figure 4.13 images show, this results in less dramatic changes of flow statistics. Nevertheless, total shear stress (and thus both primary and secondary flow consistency) is seen to be greater for larger values of $Lz_{0,H}$. In these cases, shear layer strength appears to plateau after approximately 3-4δ downstream of $x_1 = 0.0$, but it is not possible to determine how (if at all), this distance might change without the initial presence of residual, downstream shear stress caused by the periodic boundary conditions. Nonetheless, the fact that transverse

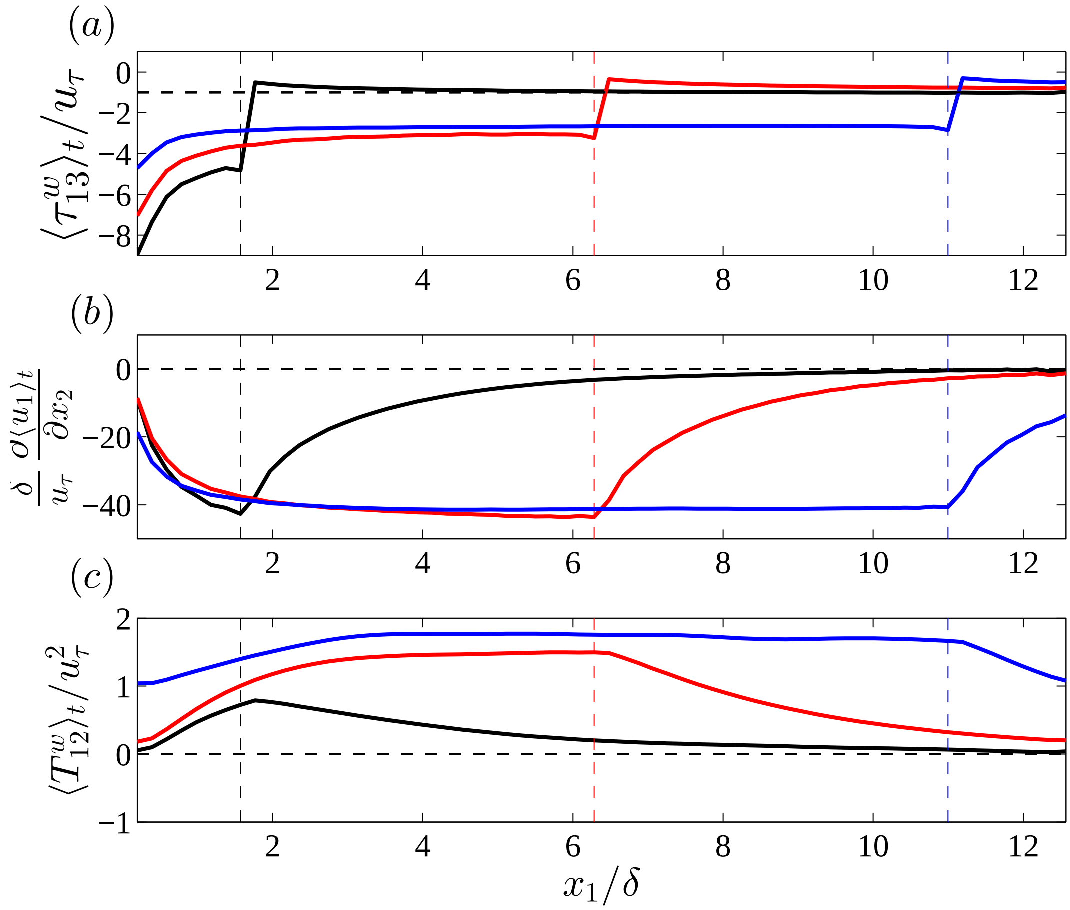

Figure 4.13: Profiles of surface stress (figure a), transverse velocity gradient (figure b) and transverse shear stress (figure c) taken at $\{(x_2 = Lx_2/4 - L_s/2)/\delta, x_3/\delta \approx 0.01\}$ from cases G1 (blue line), G4 (red line) and G7 (black line). Dashed lines indicate $Lz_{0,H}$.

variations in roughness length need not be continuous in the streamwise direction for shearing and secondary flow to be produced, is an important point to note. This could have significant importance to applications that deal with either a single patch of roughness, or intermittent patches of roughness in the streamwise direction.

4.5 Immersed Objects

As described in Chapter 3, it is currently believed that transverse velocity gradients, caused by step-changes in surface roughness, are responsible for creating shear stress, turbulent mixing and ultimately the LMP-HMP patterns shown throughout this thesis. Assuming that this is indeed the case, it stands to reason that any relatively low momentum event, located at or near a rough surface, should be able to produce similar effects. A number of previous studies have shown counter-rotating secondary flows caused by heterogeneities in surface elevation [39, 40, 45]. It would make sense that similar results to those caused by transverse variations in roughness, may also be obtained from flow over immersed objects, because they serve to obstruct flow and act as "low momentum events". In order to confirm this, a small suit of LES were run for flow past immersed objects. These objects are assigned lengths of only $\approx 0.01\delta$ in the x_1 direction, in order to isolate effects caused by the objects as much as possible from the periodic streamwise boundary conditions used. The objects are placed at equivalent x_2 locations to the $z_{0,H}$ strips of Table 3.1 cases. All domains are assigned uniform roughness lengths of $0.2/\delta$ across the entire lower boundary. Table 4.6 describes the five cases presented here, where L_s/δ denotes the non-dimensionalized object widths and "H" denotes the object heights. Figure 4.14 provides a general sketch of cases described by Table 4.6. Unlike all previous simulations in this thesis, these cases were run using an immersed boundary method, which is described in detail by Anderson 2013 [63].

Table 4.6: Summary of Immersed Object Cases

Case	H/δ	L_s/δ
$O1$	0.050	0.2
$O2$	0.010	0.6
$O3$	0.025	0.6
$O4$	0.050	0.6
$O5$	0.100	0.6
$O6$	0.050	1.0

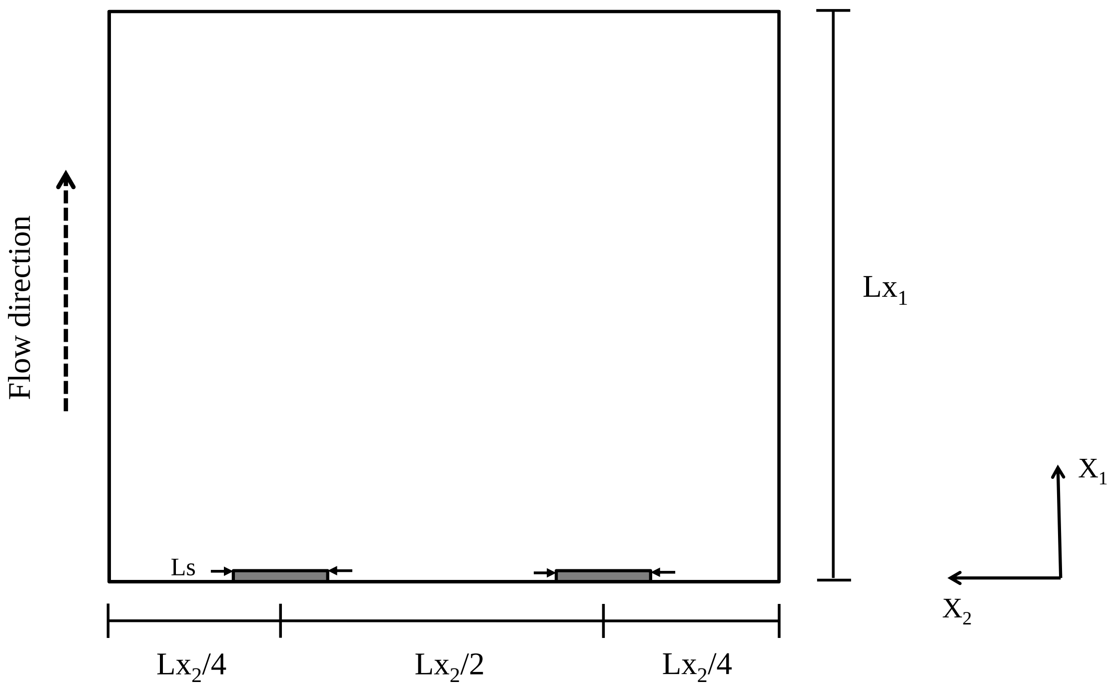

Figure 4.14: Illustration of basic surface configuration used for cases in Table 4.6. Two rectangular objects, are centered at $Lx_2/4$ and $3Lx_2/4$ with streamwise length $\approx 0.015\delta$ and width L_s.

Mean velocity values used in Figure 4.15 are taken, only from x_1 locations up to $\approx 1.0\delta$ downstream of the immersed objects. Though not as symmetric and well organized as most cases presented in previous sections, flow structures depicted in Figure 4.15 still clearly show the presence of low and high momentum pathways flanked by counter-rotating vortices. This is a noteworthy result, because it shows that only a single pair of immersed objects can generate flow features that are consistent with all others presented in this thesis. This also supports the theory, that any low momentum event, whether caused by heterogeneous surface roughness, heterogeneous surface elevation, or any other source of local reduction in streamwise momentum, will produce equivalent statistical results.

In order to verify that these immersed objects not only produce similar secondary flow structures, but are also initiated in equivalent manner to Chapter 3 cases, profiles of transverse velocity gradient and transverse shear stress are shown in Figure 4.16. Values in Figure 4.16 are taken over the same streamwise distance as those of Figure 4.15. These profiles show close qualitative agreement with trends previously noted for flow over heterogeneous roughness. Comparison of values in Figure 4.16 with those from Figures 3.11 and 3.15 shows that peaks in gradients and shear stress are less extreme for these immersed object cases. This is not at all surprising, because Table 4.6 cases only have low momentum events at a single streamwise location, as opposed to the infinite strips of high roughness in Table 3.1 cases. It is therefore not entirely unexpected to see that profiles in Figure 4.16 are not perfectly monotonic. Nonetheless, it does appear that increasing the object heights has a similar effect to increasing λ in previous cases. This is because taller objects produce larger wakes and it is these low momentum wakes, trailing downstream from the immersed objects, which impose transverse gradients on streamwise velocity.

Extreme values in Figure 4.17 show no consistent trends such as those seen in previous results. This is a notable distinction between the effects caused by immersed objects and those of elevated roughness regions. Because of the uniform roughness used in Table 4.6 cases, The total drag imposed on flow by the surface is approximately constant, regardless of the objects width. As a consequence, gradients in streamwise velocity and thus shear stress, are affected only by the object heights and not by the object widths.

Figure 4.18 (a) and (b) plots $\frac{\delta}{u_\tau}\partial\langle\tilde{u}_1\rangle_{t,1}/\partial x_2$ and $\langle T^w_{12}\rangle_{t,1}/u_\tau^2$ at: $\{x_2/\delta = \pi/2 - L_s/(2\delta),\ x_3/\delta \approx 0.01\delta\}$. As with Figure 4.16 perfectly monotonic results are not observed here due to weaker shear layers. Figure 4.18 (a) and (b), show that the

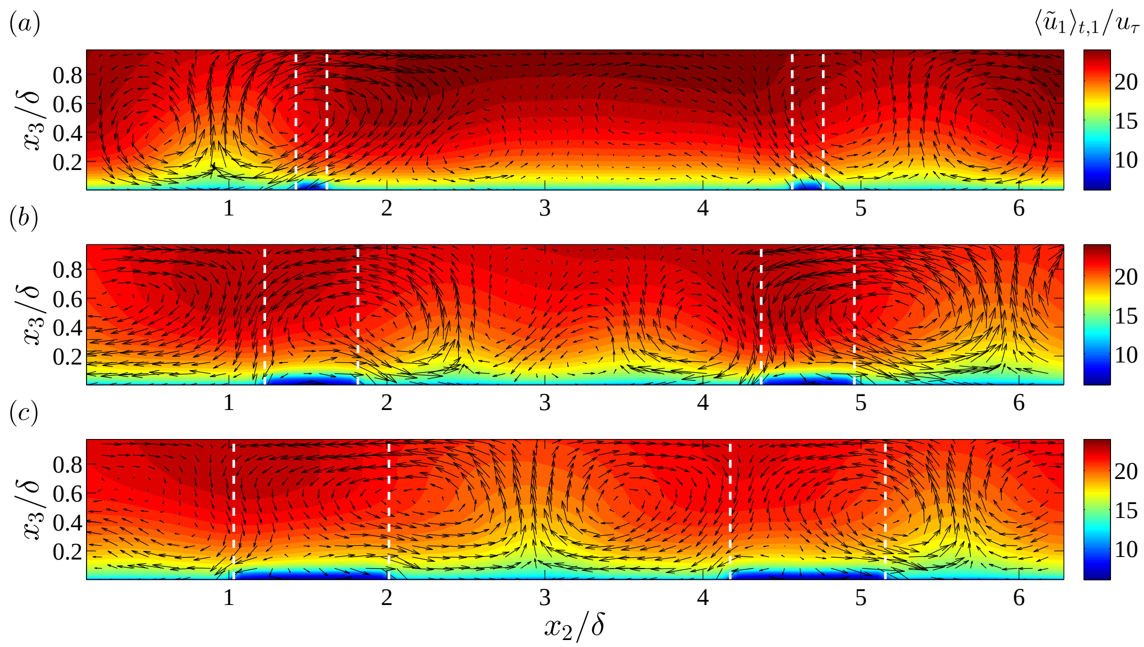

Figure 4.15: Black vectors of secondary flow components, $\{\langle \tilde{u}_2 \rangle_{t,1}/u_\tau, \langle \tilde{u}_3 \rangle_{t,1}/u_\tau\}$, superimposed over contours of streamwise velocity for cases $O1, O4$ and $O5$. White dotted lines indicate x_2/δ locations of transverse variations in surface roughness.

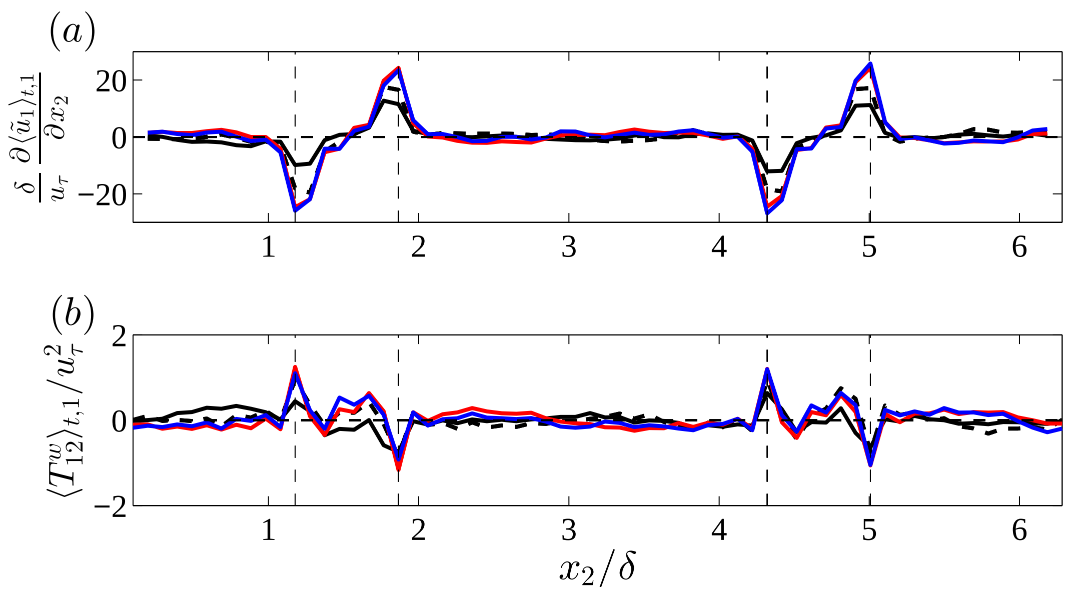

Figure 4.16: Streamwise averaged profiles of: transverse velocity gradient (figure a) and transverse shear stress at $x_3 \approx 0.01\delta$ (figure b) from cases $O2$ (black line), $O3$ (dashed black line), $O4$ (red line) and $O5$ (blue line). Dotted lines show spanwise locations of object endpoints.

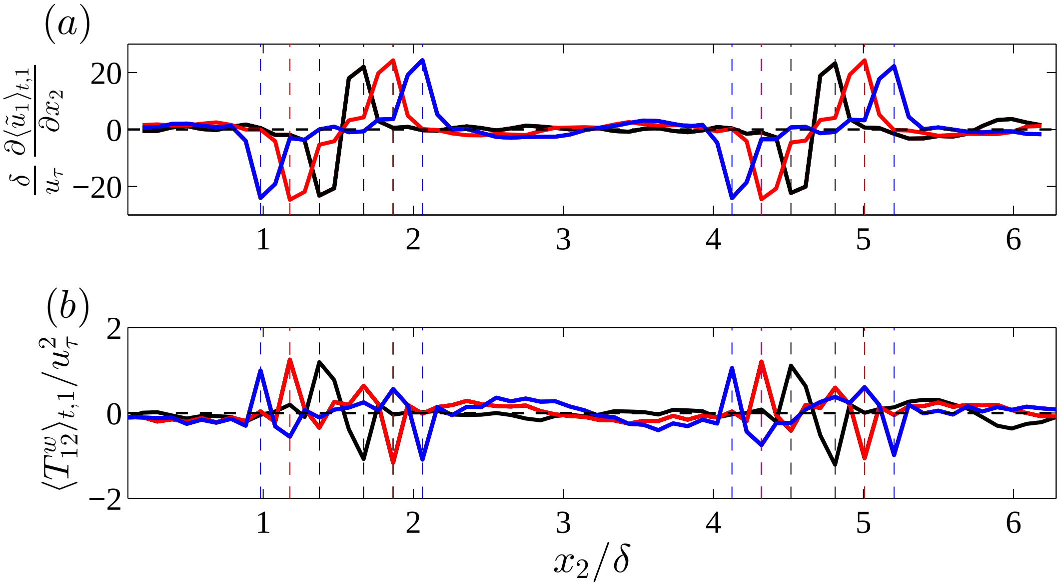

Figure 4.17: Streamwise averaged profiles of: transverse velocity gradient (figure a) and transverse shear stress at $x_3 \approx 0.01\delta$ (figure b) for cases $O1$ (black line), $O4$ (red line) and $O6$ (blue line).

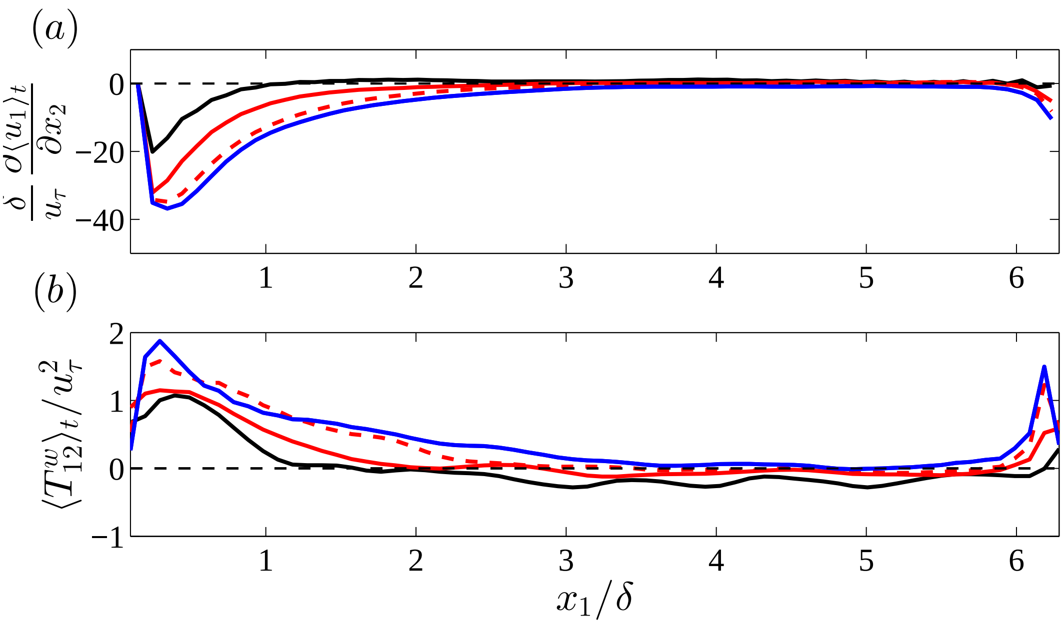

Figure 4.18: Profiles of transverse velocity gradient (figure a) and transverse shear stress (figure b) taken at $\{(x_2 = Lx_2/4 - L_s/2)/\delta,\ x_3/\delta \approx 0.01\}$ from cases $O2$ (black line), $O3$ (dashed black line), $O4$ (red line) and $O5$ (blue line).

gradients and shear layers caused by the object wakes, persist to some extent for over 3.0δ beyond the objects. This is roughly equal to the downstream reach of effects cause by roughness transitions in Figure 4.13. However, due to differences in initial magnitudes and amount of decoupling from upstream effects, a direct comparison is difficult to make between results in Table 4.6 and those in Table 4.5. Indeed, much more consideration of immersed objects is required to effectively compare the effects caused by such cases, with those caused by roughness transitions. However, it has at least been shown here, that the results presented throughout this thesis may be produced through other means than variations in surface roughness.

CHAPTER FIVE

Conclusions and Recommendations

5.1 Conclusions

Large eddy simulation has been used to predict three dimensional, fully turbulent, high Reynolds number flow, over surfaces exhibiting, transverse variations in aerodynamic surface roughness length. A single, primary set of LES was considered, which consisted of eighteen cases, all of which contained two equally spaced strips of relatively high roughness, oriented parallel to the streamwise direction and each other. A parametric study was performed with respect to two parameters: λ and Ls/δ, where λ represents the ratio of high to low surface roughness lengths and Ls/δ represents the spanwise width of the high roughness regions.

LES results showed that transverse variations in surface roughness induce the formation of high and low momentum pathways located above surface regions with high and low roughness, respectively. These pathways are approximately stationary with respect to time and spanwise position and are flanked by boundary layer scale, counter-rotating vortices, which rotate away from strips of high roughness and into the base of low momentum pathways, near the surface. This general pattern is observed for all values of λ and Ls/δ considered, but becomes less well structured and more asymmetric as values of λ increase and values of Ls/δ decrease.

These phenomenon are generated by transverse gradients in surface stress, caused by the heterogeneities in surface roughness length. Locally heightened surface roughness imposes greater drag on flow according to the logarithmic law of the wall. This creates large gradients in streamwise velocity near the surface, between low momentum flow over high roughness and high momentum flow over low roughness. As a consequence of high transverse velocity gradients at roughness transitions, profiles of transverse shear stress also show large peaks at the same spanwise locations. This indicates the formation of shearing layers forming between the high and low momentum flow regions. Shear layers drive transverse momentum flux, which occurs continuously across all roughness transitions and causes boundary layer scale, secondary flows to form, on either side of high surface roughness regions.

Boundary layer scale vortices cause vertical momentum flux, which effectively "pumps" low momentum and turbulence upwards from regions of low surface roughness and "pulls" high momentum and turbulence downwards towards regions of high surface roughness. As a result, local turbulent boundary layer heights become thickened and thinned over low and high surface roughness, respectively. This accounts for the observed locations of high and low momentum pathways, because flow in low momentum pathways have been essentially pulled farther inside the boundary layer, while flow in high momentum pathways is actually outside of the boundary layer entirely.

Values of Reynolds normal stress and turbulent kinetic energy revealed that significantly greater turbulence is produced over high roughness strips and at roughness transition locations. Turbulence is shown to be increased and decreased in low and high momentum pathways, respectively, due to vertical transport of turbulence by boundary layer scale, secondary flows. Quadrant analysis of transverse Reynolds stress was performed and it was show that shearing along roughness transitions acts in an analogous manner to streamwise surface stress, with respect to relative quadrant contributions.

Prandtls mixing length, associated with turbulent mixing at roughness transitions, l/δ, is calculated using the Boussinesq eddy viscosity model. In all cases it is found that smaller mixing length values correspond with more intense turbulent mixing. Profiles of l/δ increase and decrease with increasing and decreasing values of λ and L_s/δ, respectively, and grow in an approximately logarithmic manner with distance from the surface.

Five secondary suites of LES, run at coarser resolution were also presented and discussed. In order to justify the use of lower resolution, analogous cases to those in the primary set of LES are briefly presented and shown to exhibit reasonably good qualitative and quantitative agreement with results obtained at higher resolution. Cases are considered where surface area of high roughness length, $z_{0,H}$, is equal to or greater than that of low roughness length, $z_{0,L}$. It is found that for cases where surface area with $z_{0,H}$ is greater than surface area with $z_{0,L}$, shearing is significantly reduced and flow features become less well organized. This is the result of higher total drag imposed on the flow by the widened, high roughness regions. It is speculated that $Ls/\delta = \pi/2$ may provide optimal conditions for reduction of asymmetry in secondary flows.

A suite of cases was considered, where uniform values of high roughness length, $z_{0,H}$, are replaced with linearly decreasing values, from the center to the edges of "elevated roughness regions". These cases demonstrated that transverse changes in roughness length, need not be abrupt to create well-organized primary and secondary flow structures. These cases also showed more consistent flow structures than those with uniform $z_{0,H}$ and similar L_s/δ values. Extending this to surfaces with non-uniform roughness across the entire domain. A suite of LES was run using a sinusoidal distribution of roughness length along the extent of the transverse dimension.

These simulations produced well-structured primary and secondary flow, by creating transverse velocity gradients across the entire surface, rather than exclusively at roughness transitions.

Another suite of LES, with roughness strips extending only a fraction of the streamwise domain length, were also considered. These cases show that, while the idealized case of infinite roughness strip length is not necessary, shear layers do increase in strength as strip length (denoted by $Lz_{0,H}$) is increased. Further, it is observed that residual shearing effects continue to affect the flow over streamwise distances of more than 3δ beyond $x_1 = Lz_{0,H}$. The use of periodic streamwise boundary conditions, results in more dramatic effects on $\langle\tau_{13}\rangle_{t,1}/u_\tau^2$, $\frac{\delta}{u_\tau}\partial\langle\tilde{u}_1\rangle_{t,1}/\partial x_2$ and $\langle T_{12}\rangle_{t,1}/u_\tau^2$ for smaller values of $Lz_{0,H}$, but more total $\langle T_{12}\rangle_{t,1}/u_\tau^2$ and thus more well-organized primary and secondary flow structures, for larger values of $Lz_{0,H}$.

Finally, an immersed boundary method was used to compare the use of wakes, trailing behind immersed objects, rather than spanwise roughness changes to create streamwise velocity gradients. Results, although not perfectly monotonic, are similar results to those seen in all other LES considered in this thesis, with respect to secondary flow structures and also formation of high and low momentum pathways. This indicates that any low momentum producing event placed at the surface is capable of producing the effects detailed in this thesis.

5.2 Futures Recommendations

There is a great deal of work that can be done with this research moving forward. It is believed that through balancing turbulent kinetic energy and streamwise vorticity budgets, deeper insight may be gained about these flows from a mathematical perspective. Particularly with respect to the way in which turbulent anisotropies generate secondary flow throughout the entire flowfields.

Another topic of interest is the effect of roughness transitions at angles, neither parallel nor perpendicular to streamwise flow. Certainly, all actual applications dealing with rough surfaces exposed to atmospheric flow, may encounter flow approaching from any angle. It is theorized that such flow may be decomposed into normal and tangent velocity components and modeled such that the normal component behaves similar to flow over forward step-changes in roughness (discussed extensively in existing literature) and the tangent component experiences the effects described in this work. To date, all preliminary attempts to test this prediction have yielded inconclusive results.

Although the resolutions used in this study are believed to be sufficient to capture all relevant flow features, running both primary and secondary cases at higher resolutions could be worthwhile for validation purposes. It may be possible that higher resolution, particularly in the vicinity of the transverse transitions in surface roughness, could reveal some small scale flow features which are not resolved by the current LES.

It is also believed that cases with immersed objects merit much more consideration. A more comprehensive comparison between the effects caused by immersed objects and variations in roughness should be considered as well as the fundamental flow mechanics which drive them. Additionally, cases with smaller streamwise distance between objects could prove informative, due to enhancement of velocity gradients, caused by residual effects from upstream objects.

Coriolis forces are not considered in this work. However, this is an assumption which introduces some error into results when applied to flow over large-scale land surfaces. Therefore it is believed that future work should, if possible take the effects of Coriolis forces into account.

Finally, it is recommended that consideration be given to the effects of heat transfer caused by the counter-rotating secondary flows and local variations in turbulence described above. No effects of temperature or heat flux are considered by the current LES code. However, the enhancement of heat transfer that is expected to result from the counter-rotating, time-invariant vortices and local variations in turbulence, are likely some of the most useful and practically applicable features of this research.

BIBLIOGRAPHY

[1] E.F. Bradley. A micrometerological study of velocity profiles and surface drag in the region modified by a change in surface roughness. *Q.J.R Meteorol. Soc.*, 94:361–379, 1968.

[2] E Bou-Zeid and MB Parlange C Meneveau. Large-eddy simulation of neutral atmospheric boundary-layer flowover heterogeneous surfaces: blending height and effective roughness. *Water Resour Res*, 40:W02505, 2004.

[3] MB Parlange E Bou-Zeid and C Meneveau. On the parameterization of surface roughness at regional scales. *J. Atmos Sci*, 64:216–227, 2007.

[4] D.H. Wood. The growth of the internal layer following a step change in surface roughness. *Report T.N. – FM 57, Dept. of Mech. Eng., Univ. of Newcastle, Australia*, 1981.

[5] J.R. Garratt. The internal boundary layer – a review. *Boundary-Layer Meteorol.*, 40:171–203, 1990.

[6] R.A. Antonia and R.E. Luxton. The response of a step change in surface roughness. part 1: Smooth to rough. *J. Fluid Mech.*, 48:721–761, 1971.

[7] R.A. Antonia and R.E. Luxton. The response of a step change in surface roughness. part 2: Rough to smooth. *J. Fluid Mech.*, 53:737–757, 1972.

[8] D.H. Wood. Internal boundary layer growth following a step change in surface roughness. *Boundary-Layer Meteorol.*, 22:241–244, 1982.

[9] W.H. Schofield. Measurements in adverse-pressure-gradient turbulent boundary layers with a step change in surface roughness. *J. Fluid Mech.*, 70:573–593, 1975.

[10] M. B. Parlange J. D. Albertson. Natural integration of scalar fluxes from complex terrain. *Adv in Water Res.*, 23:239–252, 1999a.

[11] W. Brutsaert. A theory for local evaporation (or heat transfer) from rough and smooth surfaces at ground level. *Water Resour. Res.*, 11:543–550, 1975.

[12] J. Jiménez. Turbulent flows over roughwalls. *Annu. Rev. Fluid Mech*, 36:173196, 2004.

[13] S. Baidya Roy and S. W. Pacala. Can large wind farms affect local meteorology? *J. Geographical Res.*, 109:D19101, 2004.

[14] P.A. Davidson. Scientists Turbulence, An Introduction for Scientists and Engineers. page 424. Oxford University Press, Great Clarendon Street, Oxford, 2004.

[15] J. Smagorinsky. General circulation experiments with the primitive equations, part 1: the basic experiment. *Mon Weather Rev*, 91:99–164, 1963.

[16] E. Bou-Zeid, M.B. Parlange, and C. Meneveau. On the parameterization of surface roughness at regional scales. *J. Atmos. Sci.*, 64:216–227, 2005.

[17] Fernando Porté-Agel W. Anderson, P. Passalacqua and Charles Meneveau. Large-eddy simulation of atmospheric boundary-layer flow over fluvial-like landscapes using a dynamic roughness model. *Boundary-Layer Meteorol*, 144:263286, 2012.

[18] C. Meneveau F. Porté-Agel and M.B. Parlange. Ascale-dependent dynamicmodel for large-eddy simulation: application to a neutral atmospheric boundary-layerl. *J. Fluid Mech.*, 415:261–284, 2000.

[19] J. D. Albertson and M. B. Parlange. Surface length scales and shear stress: Implications for land-atmosphere interaction over complex terrain. *Water Resources Research*, 37:2121–2132, 1999b.

[20] S.A. Orzag and Yih-Ho Pau. Numerical computation of turbulent shear flows. *Adv. Geophys.*, 18:224–236, 1974.

[21] D. K. Lilly. Surface length scales and shear stress: Implications for land-atmosphere interaction over complex terrain. *The representation of small-scale turbulence in numerical simulation experiments*, page 195210, 1967.

[22] P. Moin M. Germano, U. Piomelli and W.H. Cabot. A dynamic subgrid-scale eddy viscosity model. *Phys Fluids*, 3:1760–1765, 1991.

[23] M.B. Parlange E Bou-Zeid, C Meneveau. A scale-dependent lagrangian dynamic model for large eddy simulation of complex turbulent flows. *Phy Fluids*, 17:025105, 2005.

[24] S.A. Orzag. Numerical simulation of incompressible flows within simple boundaries, 1, galerkin (spectral) representations. *Stud. Appl. Math., L*, pages 293–327, 1971a.

[25] S.A. Orzag. Numerical simulation of incompressible flows within simple boundaries: Accuracy. *J. Fluid Mech.*, 49:75–112, 1971b.

[26] W. C. Reynolds Moin, P. and J.H. Ferzinger. Spanwise structure and scale growth in turbulent boundary layers. 490:37–74, 2003.

[27] J. Wieringa. Representative roughness parameters for homogeneous terrain. *Boundary-Layer Meteorol*, 63:323–363, 1993.

[28] A.M. Obukhov A. S. Monin. Basic laws of turbulent mixing in the surface layer of the atmosphere. *Tr. Akad. Nauk SSSR Geophiz*, 24:163–187, 1954.

[29] R. Mejia-Alvarez, J.M. Barros, and K.T. Christensen. *Coherent flow structures at the earth's surface.* Wiley-Blackwell, 2013.

[30] N. Hutchins and I. Marusic. Evidence of very long meandering features in the logarithmic region of turbulent boundary layers. *J. Fluid Mech.*, 579:195210, 2007.

[31] N. Hutchins and I. Marusic. Large-scale influences in near-wall turbulence. *Phil. Trans. R. Soc.*, 365:647664, 2007.

[32] C . R. Smith and S. P. Metzler. The characteristics of low-speed streaks in the near-wall region of a turbulent boundary layer. *J. Fluid Mech.*, 129:27–54, 1983.

[33] C. R. Smith and S. P. Schwartz. Observation of streamwise rotation in the nearwall region of a turbulent boundary layer. *Phys. Fluids.*, 26:641–652, 1983.

[34] J.P. Monty B. Nugroho, N. Hutchins. Large-scale spanwise periodicity in a turbulent boundary layer induced by highly ordered and directional surface roughness. *Int. J. Heat and Fluid Flow*, 41:90–102, 2013.

[35] Y. Wu and K. T. Christensen. Spatial structure of a turbulent boundary layer with irregular surface roughness. *J. Fluid Mech.*, 655:380–418, 2010.

[36] J. M. Barros and K. T. Christensen. Cross-plane stereo piv measurements of a turbulent boundary layer overlying irregular roughness. *10th International Symposium on Particle Image Velocimetry - PIV13*, 2010.

[37] R. Mittal D. You, M. Wang and P. Moin. Large-eddy simulations of longitudinal vortices embedded in a turbulent boundary layer. *AIAA JOURNAL*, 44:3032–3039, 2006.

[38] R. K. Madabhushi and S. P. Vanka. Large-eddy simulation of turbulence-driven secondary flow in a square duct. *Phys. Fluids.*, 3:2734–2745, 1991.

[39] M. Omidyeganeh and U. Piomelli. Large-eddy simulation of three-dimensional dunes in a steady, unidirectional flow. part 1. turbulence statistics. *J. Fluid Mech.*, 721:454–483, 2013.

[40] M. Omidyeganeh and U. Piomelli. Large-eddy simulation of three-dimensional dunes in a steady, unidirectional flow. part 2. turbulence statistics. *J. Fluid Mech.*, 734:509–534, 2013.

[41] C. D. Tompkins and R. J. Adrian. Spanwise structure and scale growth in turbulent boundary layers. *J. Fluid Mech.*, 490:37–74, 2003.

[42] R. J. Adrian. Hairpin vortex organization in wall turbulence. *Phys. Fluids.*, 19:041301, 2007.

[43] E. K. Longmire B. Ganapathisubramani and I. Marusic. Characteristics of vortex packets in turbulent boundary layers. *J. Fluid Mech.*, 478:35–46, 2003.

[44] W. T. Hambleton B. Ganapathisubramani, N. Hutchins and I. Marusic. Investigation of large-scale coherence in a turbulent boundary layer using two-point correlations. *J. Fluid Mech.*, 524:57–80, 2005.

[45] H. Meng R. Elavarasan. Flow visualization study of role of coherent structures in a tab wake. *Fluid Dyn. Res.*, 27:183–197, 1999.

[46] R.J. Adrian, K.T. Christensen, and Z.C. Liu. Analysis and interpretation of instantaneous turbulent velocity fields. *Exp. Fluids*, 29:275–290, 2000.

[47] J. Wieringa. An objective exposure correction method for average wind speeds measured at a shelter location,. *Q.J.R. Meteorol. Soc.*, 102:241–253, 1976.

[48] J.C. Kaimal. Turbulence structure in the convective boundary layer. *Journal of the Atmospheric Sciences*, 33:2152–2169, 1976.

[49] J.C. Wyngaard, O.R. Coté, and Y. Izumi. Local free convection, similarity, and the budgets of shear stress and heat flux. *Journal of the Atmospheric Sciences*, 28:1171–1182, 1971.

[50] J.A. Businger. Flux-profile relationships in the atmospheric surface layer. *Journal of the Atmospheric Sciences*, 28:181–189, 1971.

[51] D. Oster and I. Wygnanski. The forced mixing layer between parallel streams. *J. Fluid Mech.*, 123:91–130, 1982.

[52] E. Kit M. Gaster and I Wygnanski. Large-sclae structures in a forced turbulent mixing layer. *J. Fluid Mech.*, 150:23–39, 1985.

[53] W. S. J. Uijttewaal D. A. Vermaas and A. J. F. Hoitink. Lateral transfer of streamwise momentum caused by a roughness transition across a shallow channel. *Water Resour Res*, 47:W02530, 2011.

[54] L. C. Hoagland. *Fully Developed Turbulent Flow in Straight Rectrangular Ducts - Secondary flow, Its Cause and Effect On The Primary Flow.* PhD thesis, Massachusetts Institute of Technology, September 1960.

[55] J. O. Hinze. Secondary currents in wall turbulence. *Phys. Fluids.*, 10:S122–125, 1967.

[56] R. Mejia-Alvarez and K. T. Christensen. Low-order representations of irregular surface roughness and their impact on a turbulent boundary layer. *Phys. Fluids.*, 22:015106, 2010.

[57] W.W. Willmarth and S.S. Lu. Structure of the reynolds stress near the wall. *J. Fluid Mech.*, 55:65–92, 1972.

[58] S. K. Robinson. Coherent motions in the turbulent boundary layer. *Annu. Rev. Fluid Mech.*, 23:601–639, 1991.

[59] R. Mejia-Alvarez and K. T. Christensen. Low-order representations of irregular surface roughness and their impact on a turbulent boundary layer. *Phys. Fluids.*, 22:015106, 2010.

[60] H. Nakagawa and I. Nezu. Prediction of the contributions to the reynolds stress from bursting events in open-channel flows. *J. Fluid Mech*, 80:99–128, 1977.

[61] K. Bai, C. Meneveau, and J. Katz. Near-wake turbulent flow structure and mixing length downstream of a fractal-tree. *Boundary Layer Meteorol.*, 143:285–308, 2012.

[62] T. Cebeci . Analysis of Turbulent Flows, Second Revised and Expanded Edition. page 92. Elsevier, The Boulevard, Langford Lane, Kidlington Oxford, 2004.

[63] W. Anderson. An immersed boundary method wall model for high-reynolds-number channel flow over complesx topography. *Int. J. Numer. Meth. Fluids*, 71:1588–1608, 2013.